Project Title	Virtual Presence in Moving Objects through 5G
Project Acronym	PriMO-5G
Grant Agreement No	815191
Instrument	Research and Innovation Action
Topic	The PriMO-5G project addresses the area of “a) Focus on mmWave and super broadband services” in the call “EUK-02-2018: 5G” of the Horizon 2020 Work Program 2018-2020.
Start Date of Project	01.07.2018
Duration of Project	36 Months
Project Website	https://primo-5g.eu/

D3.3 - FINAL REPORT ON PRIMO-5G RADIO TECHNOLOGIES

Work Package	WP3, Advanced radio technologies
Lead Author (Org)	Sang-Hyun Park (YU)
Contributing Author(s) (Org)	Sang-Hyun Park (YU), Gee-Yong Suk (YU), Soo-Min Kim (YU), Chan-Byoung Chae (YU), Sanghwa Lee (YU), Dong Ku Kim (YU), Kwang Soon Kim (YU), Eui Whan Jin (YU), Kwanghoon Lee (YU), Hyungsik Han (KAIST), Seonyong Kim (KAIST), Namshik Kim (KAIST), Seongbae Jun (KAIST), Hyuncheol Park (KAIST), Giuseppe Destino (KCL), Toktam Mahmoodi (KCL), Pardo Grino, Enric (KCL), Abdo Nasser Ali Gaber (NI), Martin Anderseck (NI), Woonghee Lee(EAB), Ki Won Sung (KTH), Dr Cicek Cavdar (KTH), Meles Mehari (Aalto), Muhammad Usman Sheikh (Aalto), Edward Mutafungwa (Aalto), Riku Jäntti (Aalto)
Due Date	30.04.2021, M34
Date	03.05.2021
Version	1.0

Dissemination Level

X	PU: Public
	PP: Restricted to other programme participants (including the Commission)
	RE: Restricted to a group specified by the consortium (including the Commission)
	CO: Confidential, only for members of the consortium (including the Commission)

The work described in this document has been conducted within the project PriMO-5G. This project has received funding from the European Union’s Horizon 2020 research and innovation programme under grant agreement No 815191. The project is also supported by the Institute for Information & communications Technology Promotion (IITP) grant funded by the Korea government (MSIT) (No.2018-0-00170, Virtual Presence in Moving Objects through 5G). The dissemination of results herein reflects only the author’s view, and the European Commission, IITP and MSIT are not responsible for any use that may be made of the information it contains.

Disclaimer

PriMO-5G has received funding from the European Union's Horizon 2020 research and innovation programme under grant agreement No 815191. The project is also supported by the Institute for Information & communications Technology Promotion (IITP) grant funded by the Korea government (MSIT) (No.2018-0-00170, Virtual Presence in Moving Objects through 5G). The dissemination of results herein reflects only the author's view, and the European Commission, IITP and MSIT are not responsible for any use that may be made of the information it contains.

Table of Contents

List of Tables

List of Figures

Executive Summary

This document incorporates radio access technologies to satisfy the scenarios required by the PriMO 5G project. Because the main goal of the PriMO-5G project is to implement a 5G end-to-end system that provides immersive video services for high-speed mobile devices such as unmanned aerial vehicles (UAV), Radio access technologies suitable for this high-capacity, high-speed mobility transmission scenario should be based on seamless connectivity, where multiple UAVs can move each radio cell without delay and interruption. Besides, new transceiver and waveform designs should be proposed, and beam tracking and beamforming technologies should be incorporated to support UAVs, a high-speed mobile network.

The D3.3 achievements are as follows. First, we proposed algorithms for trajectory planning of UAVs connected to terrestrial mmWave BSs, considering path length and quality of the ground-to-aerial connection. We considered “Drone localization based on terrestrial transmitters in both indoor-controlled and outdoor environments for enhanced localization of UAVs using multiple terrestrial BSs. We showed that mmWave blockage effects on UAV networks could be sorted out using beamforming gain and multiple antennas (MIMO) and increasing the bandwidth in our simulations. We researched analysis of propagation characteristics of UAV base stations with ray tracing. We improved the performance of sparse channel estimation by expressing each multi-path element as a geometric sequence and applying the novel method of GSD-ST. We proposed the mmWave Full Duplex-Interference Alignment(FD-IA) scheme to remove new interference with the FD network. We proposed grant-free multiple access (GFMA) that can reduce uplink connection time via grant-free uplink transmission. In Section 3, a USRP-based mmWave prototyping architecture has been presented. mmWave Beam Management has been developed based on NI’s Test UE / Test gNB. We proposed the interference cancellation algorithm with the MMSE receive filter for the QAM-FBMC system. We proposed USFDMA as a new waveform robust to dynamics of neighboring environments establishing a coexistence of different waveforms within one carrier. In Section 4, we designed a beam tracking algorithm based on monopulse ratio exploiting the CP in the OFDM system for angle synchronization. Also, we proposed a low latency AoA estimation method in the mmWave lens antenna system.

List of Acronyms

Acronym	Definition
AAC	Antenna-Array-Agnostic Control
AoA	Angle of Arrival
BFR	Beam Failure Recovery
BM	Beamforming
BS	Base Station
CDD-SDMA	Code Division Duplex-Spatial Division Multiple Access
CFR	Channel Frequency Response
CHP	Channel Power
CIR	Channel Impulse Response
CP	Cyclic Prefix
CS	Compressive Sensing
CSI	Channel State Information
CSIRS	Channel State Information Reference Signals
DAC	Digital-to-Analog Converter
DFE	Decision Feedback Equalizer
DFT	Discrete Fourier Transform
DoF	Degree of Freedom
EM	Electromagnetic
EPA	Extended Pedestrian A model
EVA	Extended Vehicular A model
FD	Full-Duplex
FFT	Fast Fourier Transform
FR2	Frequency Range 2
GFDM	Generalized Frequency Division Multiplexing
GFMA	Grant-Free Multiple Access
GSD-ST	Geometric Sequence Decomposition with k-Simplexes Transform
H-ARQ	Hybrid Automatic Repeat Request
IFFT	Inverse Fast Fourier Transform
ISD	The distance between base stations
IT	Image Theory
IVR	Immersive Virtual Reality
LoS	Line-of-Sight
MIMO	Multiple-Input and Multiple-Output
MMSE	Minimum Mean Squared Error
MS	Mobile Stations
OFDM	Orthogonal Frequency Division Multiplexing
OMP	Orthogonal Matching Pursuit
OOBE	Out-of-band Emission
OQAM-FBMC	Offset-Quadrature Amplitude Modulation-Filter-Bank Multicarrier
PBCH	Physical Broadcast Channel
PIC	Parallel Interference Cancellation
PROBE	Power Profile based Estimation

Acronym	Definition
PSS	Primary Synchronization
QAM-FBMC	Quadrature Amplitude Modulation-Filter-Bank Multi-Carrier
QOD	Qaulity Outage Duration
QOR	Qaulity Outage Ratio
RSRP	Reference Signal Received Power
S-D	Source-Destination
SCS	Subcarrier Spacings
SDMA	Space Division Multiple Access
SE	Spectral Efficiency
SER	Symbol Error Rate
SIC	Successive Interference Cancellation
SINR	Signal to Interference plus Noise Ratio
SPI	Serial Peripheral Interface
SRRC	Square Root Raised Cosine
SRS	Sounding Reference Signals
SS	Synchronization Signal
SSB	Synchronization Signal Blocks
SSS	Secondary Synchronization Signal
SWaP	Size, Weight and Power
TDD	Time Division Duplex
TTI	Transmission Time Interval
UART	Universal Asynchronous Receiver Transmitter
UAV	Unmanned Aerial Vehicles
UE	User Equipment
ULA	Uniform Linear Array
UPA	Uniform Planar Array
URLLC	Ultra Reliable Low Latency Communication
USFDMA	Universal Spatio-Frequency Division Multiple Access
ZC	Zadoff-Chu
ZF	Zero-Forcing

1 Introduction

1.1 Scope of the document

The title of the D3.3 is “Final report on PriMO-5G radio technologies”. WP3 has been researching the fundamental core technologies of the PriMO-5G project. Beyond D3.1 [PRIMO-D31] and D3.2 [PRIMO-D32] as an intermediate deliverable, D3.3 provides the last radio access technologies to realize the scenarios. To support fast-moving objects and send immersive videos, WP3 should achieve low latency and high data rate via variable radio access technologies, mmWave 5G transceiver and waveform design and beamforming technologies. This document spans all technologies to achieve PriMO-5G scenarios. Especially in D3.3, radio access technologies cover research from characteristics of drone communication and mmWave channel estimation to full-duplex and multiple access.

1.2 Structure of the document

D3.3 consists of three sections, such as radio access technologies, radio transceiver & waveform design, and beamforming technologies.

Section 2 is about radio access technologies. Especially, this section consists of two categories, which are research about drone communication and RAT research supporting those. Since drone has characteristic about altitude and free mobility unlike vehicles, D3.3 introduces research topic such as drone propagation, trajectory planning, and drone localization. The remaining parts contain Full duplex interference alignment for two times capacity and Grants-free multiple access for URLLC.

Section 3 is about the mmWave transceiver design and waveform. First, the description of the mmWave transceiver system is provided. A receiver that incorporates MMSE-Interference canceling, vital for quadrature amplitude modulation-filter-bank multi-carrier (QAM-FBMC) technology, is presented. To enable low latency with high reliability, time-varying multiple access with spatial-frequency filter for mmWave is described.

Section 4 is about beamforming technologies. First, a novel codebook-based two-stage solution that combines a novel beam tracking protocol with a low sounding overhead, a unique receiver structure employing a beam scheduler and a beam tester, and a fine accuracy residual AoA/AoD error estimation algorithm based on the monopulse ratio concept is proposed. Then, a novel AoA and beam tracking algorithm for the lens-incorporated mmWave hybrid architecture is presented.

Finally, conclusion and the SwaP issue are presented in Section 5.

1.3 Relationship to other project outcomes

Deliverable 3.3 will provide input on the planned demonstration activities in D5.1~D5.3 of WP5 Testbed and demonstration, which will include some of the experimental implementations of the enhanced radio access technologies and concepts introduced in this document. In the D5.3, based on WP3 D3.1~D3.3, demo from European partners, Korean partners and intracontinental system will be presented.

2 Radio access technologies for the PriMO-5G

2.1 Introduction

The PriMO-5G firefighting scenarios and use cases were previously described in deliverable D1.1 *PriMO-5G Use Case Scenarios* [PRIMO-D11]. These include two scenarios, namely, forest firefighting in rural areas and firefighting in urban areas, with each of these scenarios having two associated use cases (see Figure 2-1). Each of these use cases introduces stringent requirements for ubiquitous, reliable and high-capacity wireless connectivity inspired by the critical needs of firefighting operations. In practice this also considers on-the-scene wireless connectivity between and among mobile or nomadic firefighting entities on the ground (human firefighters, robots, fire engines, etc.) at the firefighting scene, as well as, in the aerial spaces (e.g. UAVs or drones)[1] above the scene. This setting with heterogeneous connectivity modes (ground-to-ground, ground-to-aerial, aerial-to-aerial etc.), service classes (e.g. mission-critical eMBB), user types (e.g. terrestrial versus aerial), and so on, creates a need for enhancement in radio access networks to support firefighting requirements of the different use cases as outlined in D1.1 [PRIMO-D11].

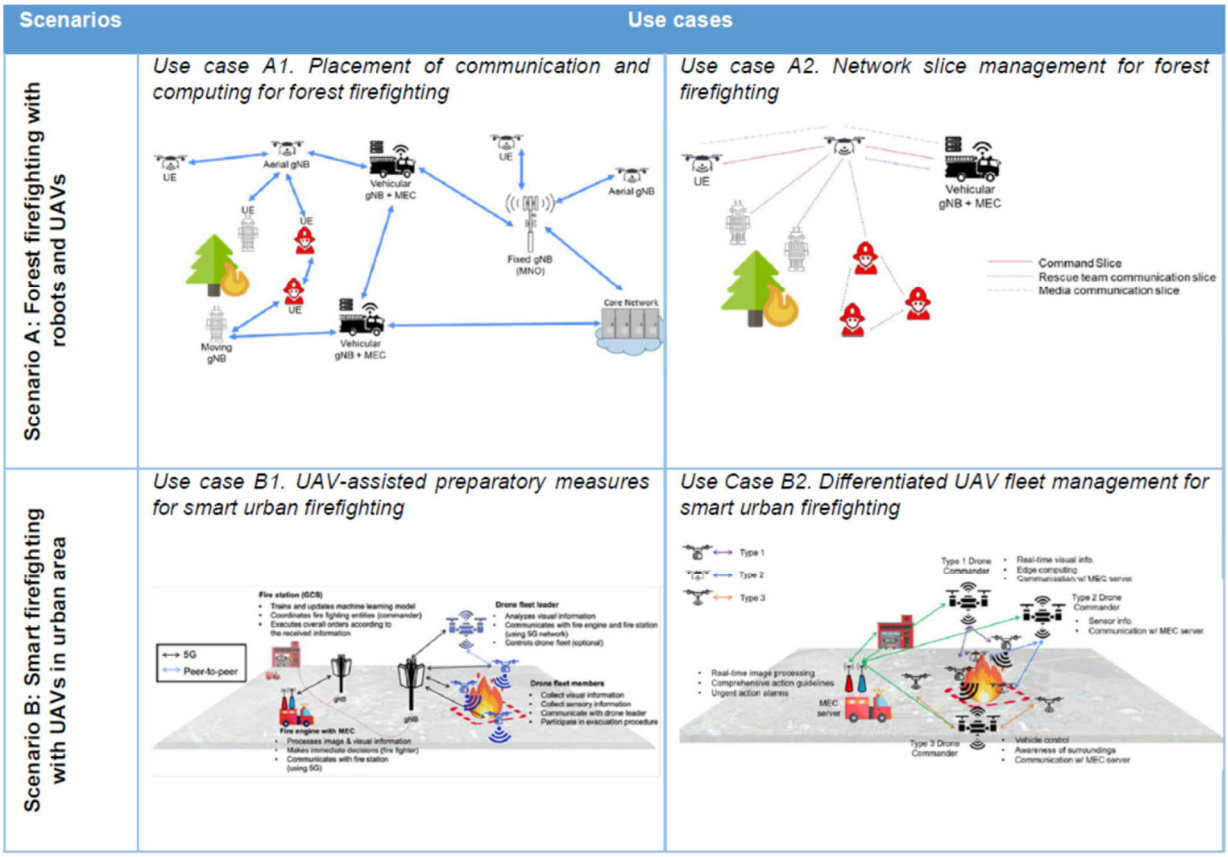

Figure 2-1 PriMO-5G use cases and scenarios

This Section outlines some of the limitations in conventional radio access technologies and different approaches considered for their enhancements to enable support of the aforementioned PriMO-5G use cases. The study items includes the following:

[1] In this deliverable, the terms UAV and drone will be used interchangeably

- Improved support for firefighting UAVs connected by terrestrial base stations (BSs) through careful (performance-aware) planning of the trajectory of UAVs (see Section 2.2), seamless mobility of UAVs connected to multiple terrestrial BSs, as well as, insights on measurements for enhanced localisation of UAVs (e.g. for improved handover) using multiple terrestrial BSs (see Section 2.3).
- Investigation of the coverage limitations of mmWave (or higher) bands and how these could be alleviated when these bands for used by UAVs connected to terrestrial BSs (see Section 2.5) or UAVs themselves are used as BSs providing extended coverage for terrestrial BSs (see Section 2.5). Moreover, Section 2.6 proposes channel estimation technique that leverages sparse behaviour of mmWave bands with potential use in both aerial and terrestrial channels.
- Finally, additional enhancements in the radio access are proposed with potential to improve PriMO-5G service KPIs through increased capacity by use of full-duplexing with enhanced interference mitigation (see Section 2.7) and reduced latency through grant-free multiple access schemes (see Section 2.8).

2.2 Quality-aware trajectory planning of cellular connected UAVs

Cellular networks are traditionally built for serving terrestrial users. However, cellular networks are effective in providing support services to UAVs for long-range and critical applications. There exists coverage holes in practical cellular networks, whereas, the usage of UAVs in varied application scenarios may require a non-interrupted connectivity and a good quality of service from cellular networks. The main objective of this research work was to propose a modified form of well-known graph search methods i.e., Dijkstra and A-star also known as A* algorithm, for quality-aware trajectory planning of the UAV. The Signal to Interference plus Noise Ratio (SINR) is considered as the quality metric of the network as is used an input for UAV trajectory planning algorithm. For comparing the performance of different trajectory planning approaches, the UAV trajectory is quantified in terms of three performance metrics i.e., path length, Quality Outage Ratio (QOR), and maximum Quality Outage Duration (QOD). The target of proposed path planning algorithm is to achieve a trade-off between the path length and other quality metrics of the UAV trajectory.

2.2.1 System model

We have only considered the horizontal mobility of the UAV i.e., UAV flies horizontally from the source point to the destination point at same height, and the whole space is discritized into a grid of equal spaces. At any grid position, the UAV is allowed to move in one of the possible eight directions i.e., forward, backward, right, left, right-forward, left-forward, right-backward, and leftbackward, the later four movements are the diagonal movements. It is assumed that UAV flies at a constant speed from source point to the destination point. Aerial quality map is used as an input for the trajectory planning algorithm, and aerial quality map is also discretized into equal grid as UAV mobility space. The aerial quality map is the matrix with binary numbers, and it shows that each grid unit in the UAV mobility space the cellular network is able or not able to provide services with above or equal to certain quality threshold (δ).

2.2.2 Performance metrics

The UAV trajectory is quantified in terms of three performance metrics i.e., path length, Quality Outage Ratio (QOR), and maximum Quality Outage Duration (QOD).

- The path length is defined as the length of the UAV trajectory from the source to the destination point in meters.
- The QOR is given in percentage and is defined as the ratio of the grid units with cellular quality lower than the quality threshold to the total number of grid units the UAV covers along the trajectory.
- The QOD is defined as the length of the consecutive quality holes in the UAV trajectory.

2.2.3 Simulation Cases

We have considered three cases for comparison, and their details are given as:

- **Shortest path ($\alpha = 1$):** The first trajectory planning method we have considered is the basic and the most widely used "Shortest path" algorithm. It follows the shortest route between the source and the destination point and does not consider any quality constraint. In case of shortest path, the biasing factor $\alpha = 1$.
- **Outage avoidance path ($\alpha = \infty$):** In the second case, the target is to completely avoid the outage by not going into quality/coverage holes. In case of outage avoidance path, the biasing factor $\alpha = \infty$.
- **Proposed quality-aware biased path:** In our proposes approach, a compromise is made between the shortest path and the outage avoidance path. In the proposed quality-aware biased path algorithm, the weight of the nodes with quality level below the threshold is altered with the biasing factor. The biasing factor varies the path length, and that in turn changes QOR of the path. The biasing factor can be adjusted with respect to the requirement of the trajectory planner. In this case the biasing factor $1 < \alpha < \infty$.

2.2.4 Simulation approach/methodology

MATLAB is used as a simulation tool, both for generating the aerial coverage/quality map data and for finding the optimal path of the UAV. The simulations are performed using an agreed 3GPP macro cell LoS scenario for UAVs. We have considered a cloverleaf tessellation with nineteen macro sites having an intersite distance of 500 m, and each macro site has three sectors with fixed angular separation in an horizontal plane as shown in Figure 2-2. The Base Station (BS) antenna height is set to 25 m, and the frequency of operation is 28 GHz, utilizing 20 MHz system bandwidth. It is assumed that UAV flies at the height of 200 m, and there exists a line-of-sight (LoS) between the BSs and UAV. The aerial map is computed only for the focus area which is highlighted with a blue rectangle in Figure 2-2.

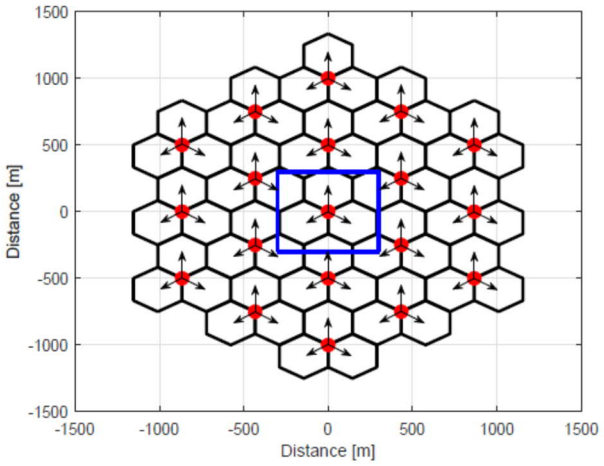

Figure 2-2 Grid of 19 sites for simulations

2.2.5 Simulation results

We evaluated the performance of different trajectory planning algorithms for two different Source-Destination (S-D) pairs, and considered modified Dijkstra and modified A* algorithm. Figure 2-3 shows the aerial quality map of the focus area, and the gray and black color of the map shows the grid units with above or equal and below the quality level threshold, respectively. The aerial map was obtained by using the quality threshold of −3 dB SINR.

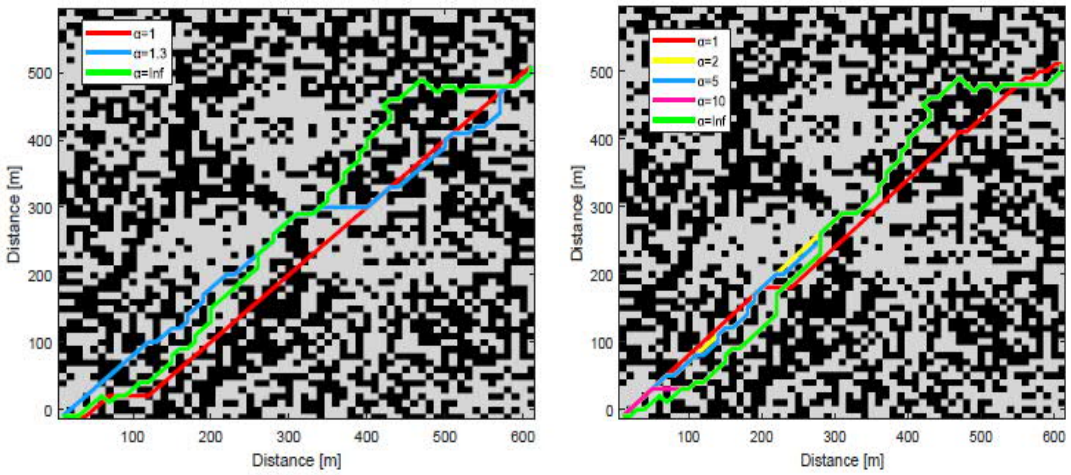

(a) (b)

Figure 2-3 UAV trajectories for source-destination pair 1 with different biasing factor, (a) Modified Dijkstra algorithm, (b) Modified A* algorithm

Figure 2-3(a) shows three UAV trajectories, whereas those trajectories were obtained by using a modified Dijkstra algorithm with three different values ofbiasing factor α. The path with α = 1 corresponds to the shortest path, $\alpha = Inf$ corresponds to detour or outage avoidance path, and α = 1.3 is a biased quality-aware path. It can be seen in Figure 2-3(a) that the shortest path did not consider any quality constraint and follows a trajectory that provides minimal flying distance. On the other hand, the outage avoidance path strictly takes into account the quality metric and took the longest path to reach destination. The biased path finds the compromise between the two different paths, and follows a path longer than the shortest path but smaller than detour path and made a compromise at the quality of the link. Similarly, Figure 2-3(b) shows five different trajectories of UAV obtained with a modified A* algorithm.

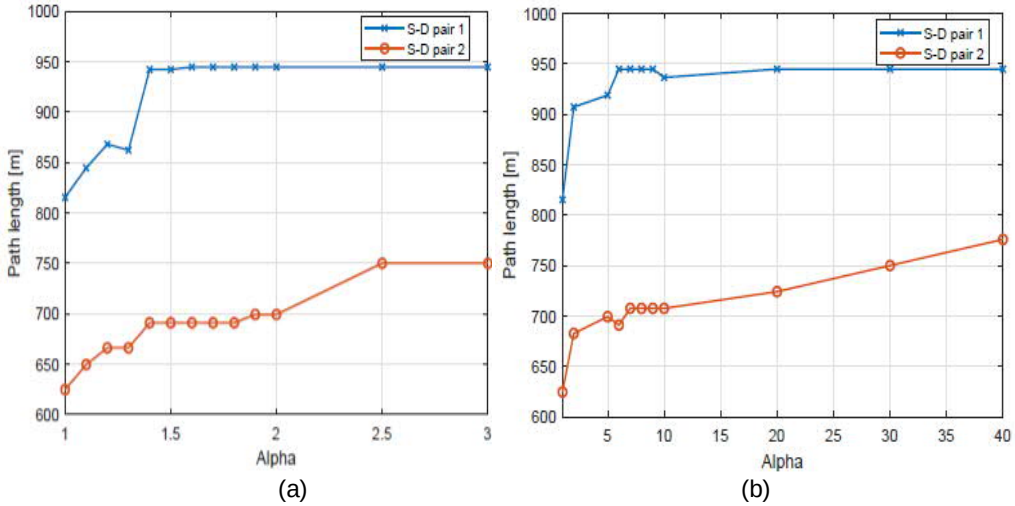

(a) (b)

Figure 2-4 Path lengths of UAV with different biasing factor, (a) Modified Dijkstra algorithm, (b) Modified A* algorithm

Figure 2-4(a) and Figure 2-4(b) show the length of the paths in meters, as a function of biasing factor α for modified Dijkstra and A* algorithm, respectively. It is observed that that the modified Dijkstra approach is sensitive to even small values of the biasing factor, whereas the modified A* algorithm is not that sensitive compared with modified Dijkstra. It can be seen that path length generally increases with the increase in the biasing factor.

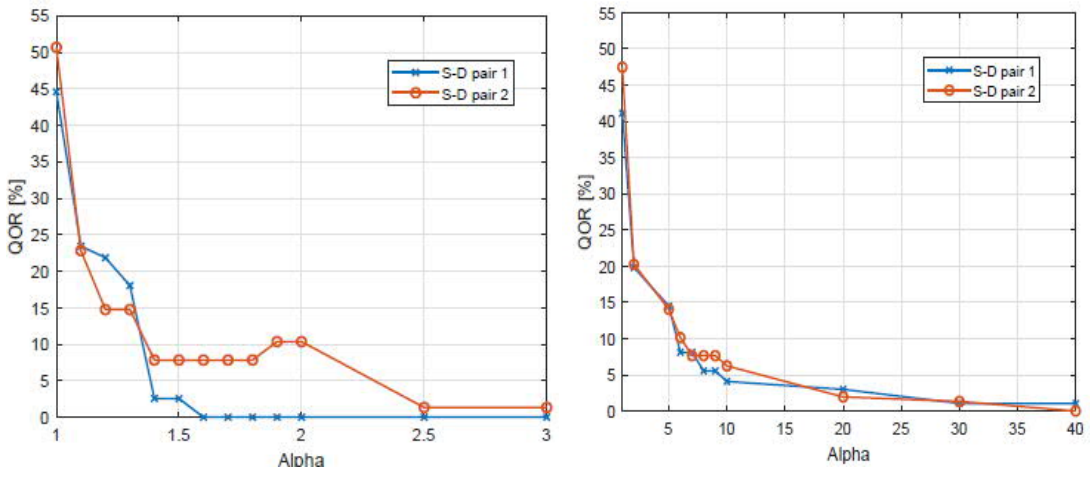

(a) (b)

Figure 2-5 Quality outage ratio of UAV with different biasing factor, (a) Modified Dijkstra algorithm, (b) Modified A* algorithm

Figure 2-5 shows the QOR against the biasing factor α. In Figure 2-5, it is observed that the QOR becomes improved in both cases of modified Dijkstra and modified A* algorithm by increasing the value of the biasing factor. It can also be seen that the trajectory with minimum path length has maximum QOR, and vice versa. The QOR of the outage avoidance path is zero, as it does not enter the coverage hole at all. It is interesting to analyze Figure 2-5(a) and Figure 2-5(a) together, for S-D pair 1 by using the biasing factor of 1.1 in modified Dijkstra model, the path length is increased by 3.6% and QOR is improved by 90.2% with respect to the shortest path. Similarly, the results of other S-D pair with both algorithms show the effectiveness of adding a cellular aerial quality based biasing factor in achieving a good compromise between the path length and QOR.

2.3 Drone localization based on terrestrial transmitters

Localization has been an active field of study for the last few decades. Earlier, localzation methods were planned for fleet management, emergency medical services and monitoring vehicles. In this project, we consider a drone equipped with an antenna having two non-isotropic antenna shown below in Figure 2-6, with antenna gain $G_{rx}(\theta, \psi)$ where θ denotes the azimuth angle and ψ denotes the horizontal angle of the arriving signal. Assume that the azimuth angle is equal to 0 radians correspond to magnetic North. Let φ denote the angle that the drone is facing away from the magnetic north. A known emitter is located in the direction θ from the magnetic pole. In the line-of-sight (LoS) conditions, the Frii's equation states that

$$P_{rx}(\phi) = G_{rx}(\theta - \varphi, \psi)\left(\frac{\lambda}{4\pi d}\right)^2 G_{tx}(\theta, \psi)P_{tx} \tag{2.1}$$

where λ is the wavelength, d is the distance between the drone and the signal source, G_{tx} is the transmitter antenna gain and P_{tx} is the transmitted power. Due to the noise, the power is varying randomly with the mean given by $P_{rx}(\phi)$. The drone measures the power $P_{rx}(\varphi_k)$ in several known angles, $\{(\varphi_k), k \in K\}$ and then seeks to find the angle θ that maximizes the convolution between the power and given antenna pattern:

$$\theta = \text{argmax}_{-\frac{\pi}{2} \le \theta \le \frac{\pi}{2}} \sum_k G_{rx}(\theta - \varphi_k, \psi)P_{rx}(\varphi_k) \tag{2.2}$$

Figure 2-6 Drone setup

Assume that the drone is localized in the coordinates (x,y,z). We target to estimate the 2D location (x,y) based on AoA and the height z based on altimeter or downwards placed laser range finder. The drone is able to estimate angle of arrival θ_k, ∈ K from ∈ K = 1,2,...,K known transmitters located in 2D plane in coordinates (x_k, x_k). In the absence of AoA estimation errors and drone location uncertainty, we would have

$$\mathrm{Tan}\,\theta_k = \frac{y-y_k}{x-x_k}, \forall k \in \mathcal{K} \tag{2.3}$$

We assume that the estimated angle is Gaussian distributed around the true value $\hat{\theta}_k \sim \mathcal{N}(\hat{\theta}_k, \sigma^2_{\theta_k})$. If we can obtain multiple measurements for the single AoA angle $\hat{\theta}_k(t)$, we have

$$\mathbb{Pr}\{\tan\hat{\theta}_k \leq t\} = \Phi\left(\frac{\arctan(t)-\theta}{\sigma_{\theta_k}}\right) \tag{2.4}$$

Given AoA measurements from K different base stations, we can then localize the drone by solving

$$\min_{(x,y)\in\mathbb{R}^2} \sum_{k\in\mathcal{K}} e_k^2 \tag{2.5}$$

where

$$e_k = (x-x_k)\tau_k - (y-y_k) \tag{2.6}$$

Let x_d and y_d denote the position of the drone and this can be represented as $p_0 = (x_d,y_d)^T$. We are interested in identifying drone 2D location from the measured angles between directions towards known base stations locations. Assume we know base station BS_i location $bs_i = (x_i,y_i)^T$. A vector towards a BS is $\vec{v}_i = p_0 - bs_i$. The angle between directions towards different BS can be expressed as

$$\alpha_{ij}(\boldsymbol{p}_0) = \angle\{\vec{\boldsymbol{v}}_i, \vec{\boldsymbol{v}}_j\} = \arccos\left(\frac{\vec{v}_i\cdot\vec{v}_j}{|\vec{v}_i|\cdot|\vec{v}_j|}\right) \tag{2.7}$$

At the drone, we can measure direction towards multiple BSs and angles between those directions $\tilde{\alpha}_{ij}$. We can construct function describing difference between the computed angle and the measured angle $\alpha_{ij}(p_0) - \tilde{\alpha}_{ij}$. The estimated location of the drone is location $\boldsymbol{p}_0$ that minimize the difference between the computed angles and the measured angles. The optimization function is

$$\min_{p_0\in\mathbb{R}^2} \sum_{ij} \left|\alpha_{ij}(p_0) - \tilde{\alpha}_{ij}\right| \tag{2.8}$$

where index pairs i,j consider all the angle differences measured at the drone. The general setup of multiple base station with drone is given in Figure 2-7. However, in our measurement we use only two base stations to localize the drone.

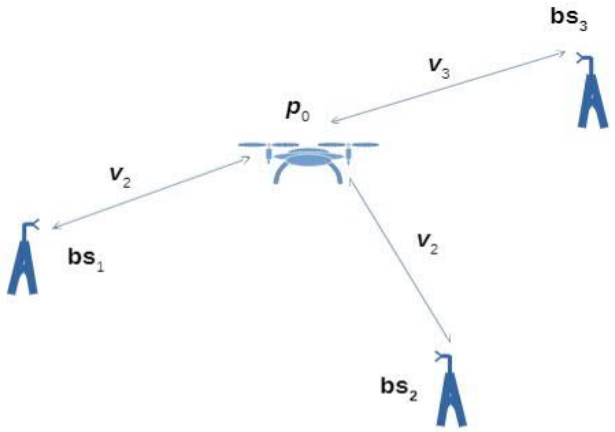

Figure 2-7 Setup with multiple base stations

2.3.1 Anechoic chamber measurement

We measured the signals coming from two Base Stations (BSs) i.e., BS1 (3.0GHz) and BS2 (3.03 GHz). We keep one of the base station at 90 degree and the second at 120 degree. The receiver rotates with 10-degree steps and we also considered multiple (100) measurements.

Table 2-1 Main Parameters of the measurements

Parameters	**Values**
Number of Antennas	2
Frequency	3.0/3.03 GHz
Inter Element Spacing	0.5 λ
Number of Base Stations	2
Signal Generator Output	-20 dBm
True AoA (Degree)	90/120

Figure 2-8 Anechoic chamber setup

We performed extensive measurements to examine the received signal from the two base stations at different locations with respect to the receiver. Due to the uncertainty of the rotation of the receiver, the

received power from the second base station is somehow shifted with some angles and this causes the estimation of the direction of the base station more erroneous. The acquired results multiple measurements clearly indicate that the received power coming from the two base stations is consistent and stable. This shows there is a good estimation of the direction of the base station.

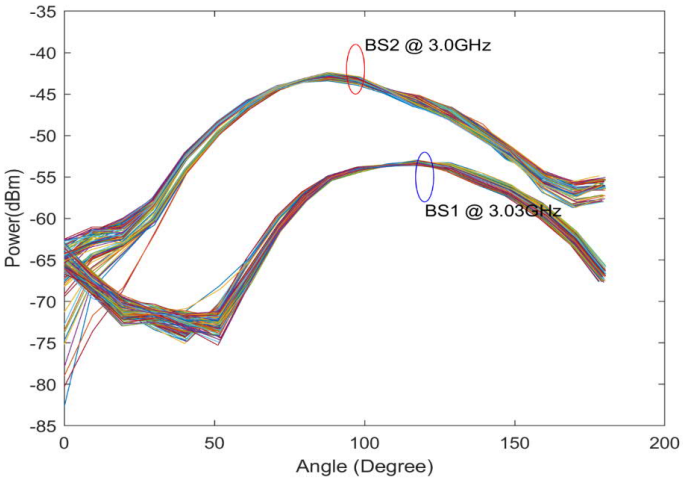

Figure 2-9 Anechoic chamber measurement received power of the two incoming signals

From the incoming signal shown in Figure 2-9, we can estimate the angle of arrival (AoA) for each measurement. It is clearly seen that the maximum received power from BS1 and BS2 are coming from the angles 120 and 90 degree respectively. It is also stated in (2-8) that the estimated location of the drone has minimized the difference between the computed angles and the measured angles. The computed angle is the angle between the two base stations, which is 30 degrees as shown in Figure 2-10. Therefore, from the received signal shown in Figure 2-9, it's possible to estimated the anlgles and the estimated AoA for each measurements and BSs is given below, Figure 2-10.

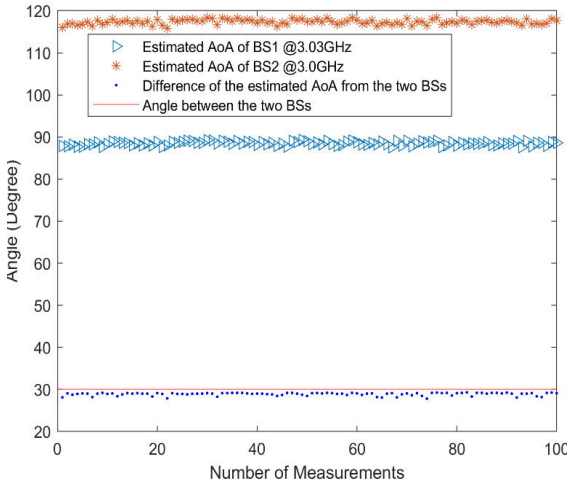

Figure 2-10 Anechoic chamber estimated angle

2.3.2 Outdoor measurement

We conducted an experiment by fixing the drone at one location in our university campus to validate our approach. For obtaining the orientation of the drone we made a comparison between two components; one the drone GPS and the other from an external compass which can give an absolute orientation with respect to the Magnetic north. The first experiment was a ground test to check the sensitivity of the two components. The drone was kept on a large compass which was hand drawn and

the idea of this test was to rotate the drone every 10° starting from 0° to 180° and collect the data from the GPS and External compass. We used Raspberry Pi 3 B+ as a companion computer to obtain and record the data. The outdoor measurement setup is shown in below Figure 2-11.

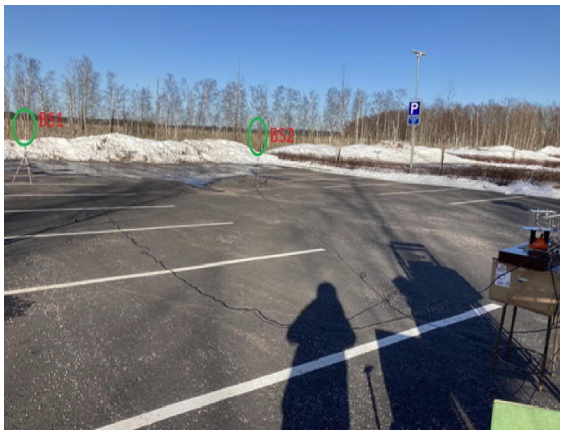

Figure 2-11 Outdoor measurement setup

From this experiment, the received signal for the multiple mueasuremnt is as shown below in Figure 2-12 and it can be clearly seen clearly that the received power is not stable and this happens due to the effect of the environmental reflections and multipath effects. This brings huge impact on the angle estimations which affects the localization of the drone. To solve this problem, we are working on the extended kalman filter for minimizing the uncertainitiy of nonlinear localizations

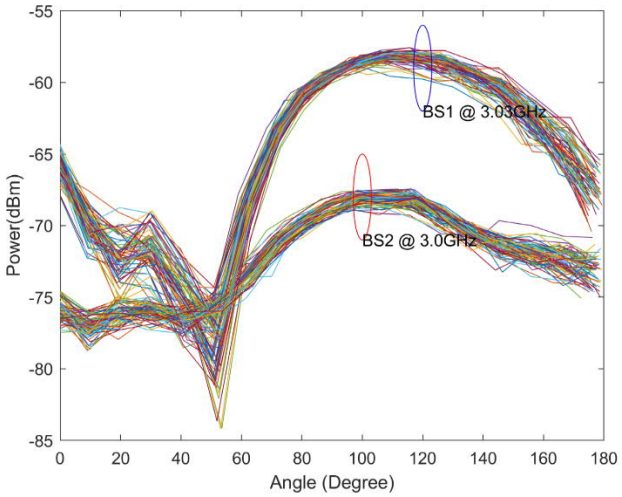

Figure 2-12 Received power of two incoming signals in an outdoor Measurement

2.4 Analysing the limitations of mmWave for UAV communications

Higher frequencies will be exploited in future mobile communications generations. On the way of use expand the range of frequencies by using THz communications, there is an actual transition from microWave communications to mmWave communications. This trend is extended to all types of UEs

and applications. Therefore, it is essential to evaluate how the UAVs perform in mmWave communications, considering the narrowness of the beam in higher frequencies.

Despite the benefits of these range of frequencies (the narrow beams increase the receiving power to the UE), it also have some drawbacks. Firstly, the narrowness of the beam increases the chances of the connection being blocked. Then, as the pathloss is dependant to the distance, higher distances as UAV-terrestrial BSs is highly affects the final performance of the connection. To this end, in this study we aim to evaluate how all these variables (the beamforming gain, the bandwidth, the central frequency and the height of the UAV) affects to the maximum Euclidean distance the UAV can be from the terrestrial BS, the received SINR, and the Capacity coverage (i.e. how many users within a certain area have an achievable capacity above a given threshold). We consider all those scenarios in terms of the ISD (the distance between base stations). In other words, how these 3 KPIs are affected by the densification of the scenario.

2.4.1 System model

We have simulated our scenario using MATLAB software. We have deployed a set of terrestrial Base stations (BS) following an even hexagonal fixed distribution, separated from each other certain distance. The distance between BS is denoted by ISD, which stands for Inter Site Distance. We use the ISD as a variable to evaluate how the densification of the scenario affects to the SINR received by the UE.

For this study, we consider a static scenario in which the UE is centred in a [5000x5000] meters grid, and we will evaluate the performance of different KPIs in different situations. First, we evaluate the received SINR by UE located in the centre of the grid. We consider interference from other BS. Then, we evaluate the coverage in terms of Euclidean distance and achievable capacity. In order to evaluate the Capacity coverage, we have deployed different possible user locations (25x25) along the square grid. In each position, we compute the SINR, and the Capacity and we evaluate in how many locations the Capacity is above certain threshold. In Figure 2-13, an example of the UE evaluate locations and the BS deployment is shown. In this case, the grid is 10 km^2 and the ISD is 2.5 km. Finally, in order to represent the mmWave connectivity, we consider beamforming gain, with 64 antennas on the transmitter and 8 antennas on the receiver.

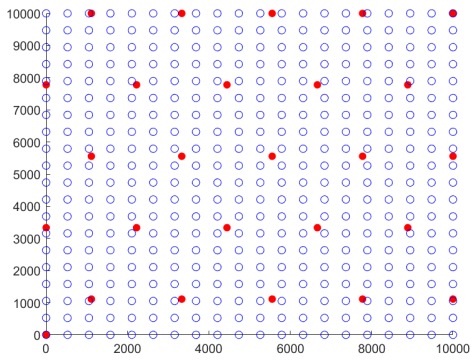

Figure 2-13 Scenario simulation: Red dots are the BS, with ISD of 2500m. Blue dots are the UE locations for the coverage analysis

2.4.2 SINR Analysis

First, we compute the SINR of a user centred in the grid. We evaluate the SINR for three different heights:

- Low height (h<40m): The UAV is at the same height or below the top of the buildings.
- Medium height (h=50-90m): The UAV lies above the buildings but still subjected of blockage.

- Higher alttitudes (h>100m): The UAV is assumed to be LoS and no blockage is considered.

In Figure 2-14, we simulate those group of heights in a grid of 5 km^2. We compute the SNR for different ISD, from 200m to 2000m set apart. For low and medium heights, we observe the same trend on the SNR (overall, in lower heights SNR it is a lower due to the higher blockage). As we increase the number of BS (i.e. the ISD is lower), the SNR increases up until an optimal number of BSs. By densifying the scenario beyond this point, the SNR decreases again due to the higher number of interfering BSs. For LoS heights (h=120m in the figure), the effect of the interference is not visible as there are more BS as LoS, and the received signal will always be from the closest BS.

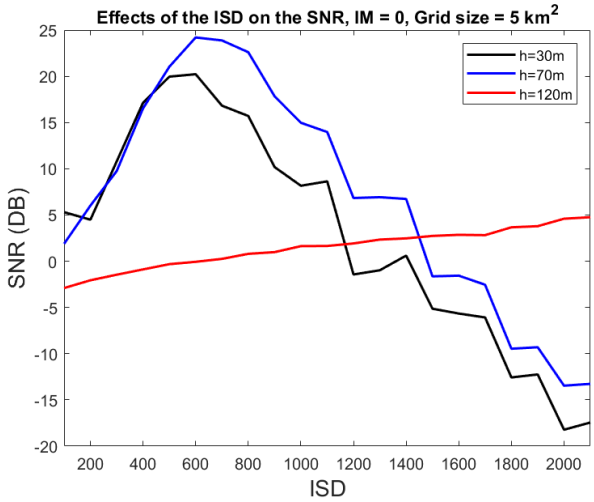

Figure 2-14 SNR of the centred-user device

2.4.3 Euclidean distance limitations

From the LoS distribution, we can ensure that it depends on three main factors, the distance Euclidean distance (2D) the height of the UAV, and the frequency in which the signal is emitted, *f*. We note that loss due to the attenuation increases abruptly and at a very short distance. A natural question that follows this, based on this distribution is: Given a certain height, working at a certain frequency, and given a maximum LoS (which can be derived from a minimum receiving power), which is the maximum Euclidean distance that the UAV can be from the terrestrial BS?

This maximum Euclidean distance is usually limited by the maximum Loss allowed by the UAV. Loss is, at the same time, depending on the maximum receiving power from the BS. Therefore, if for instance the minimum receiving power in order for the connection to be successful is -90 dBm, L = 115 dB. In Figure 2-15 we can observe the maximum euclidean distance for different heights. An observation based on these results, is that in order to be able to increase the Euclidean distance in which the UAV and the terrestrial BS the minimum received power need to be as low as possible. We show, based on those minimum received power, how the beamforming gain can increase this maximum Euclidean distance. We have simulated 2 different scenarios (beamforming mmWave gain, uniform gain, and 20 and 0 dB of SNR threshold), which gives us four possible deplyments. In a), we only show the effects of the SNR threshold, whilst in b) we show how the distance is affected by the interference.

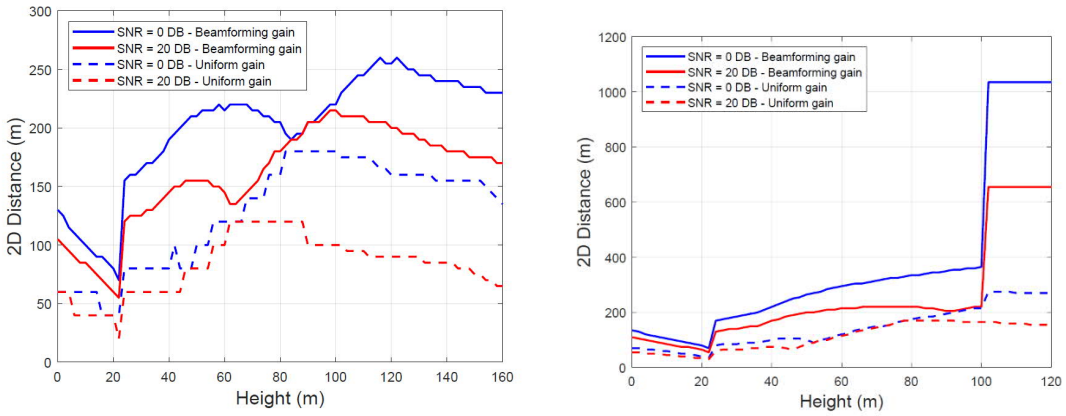

(a) (b)

Figure 2-15 Maximum Euclidean distance coverage, (a) Single base station scenario, (b) Multi base station scenario, interference

2.4.4 Capacity coverage simulation

In our final simulation, we evaluate the Capacity threshold to investigate the amount of users can be covered for a certain BS deployment. In our case, we consider the Capacity threshold fas an acceptavle achievable capacity by the UAV as C=1Mbps**.** To do so, we first locate the UE in all possible grids, and calculate the SNR and the Capacity respectively. In order to make the scenario realistic, at each of the possible pair of location-ISD evaluations we randomise the plos depending on the height and Euclidean distance between the BS and the UE. Based on this plots, we randomise the state of the UAV (either LoS and NLoS, for heights < 100m. --- We consider always LoS above 100m). We finally apply the LoS or NLoS pathloss depending on the state of the UE at this point. Thus, some uncertainty is depicted in the figure with some spikes in the Capacity coverage.

In Figure 2-16, we show the percentatge of UEs that are above the threshold. In a) we consider an interference-limited system. For lower heights, the trend follows the same approach as the SNR behaviour. There is an increase of the percentatge of UEs above the threshold ip until a certain BS distribution ISD. By densifying the scenario after the optimal ISD, the interference affects to the total coverage we observe a decrease in a highly densified scenario (ISD<200 m). On the other hand, for LoS heights, the trend is different. Since we receive interference for more BS, the coverage on a high densified scenario is much lower (as the average Capacity is lower). This leads to a trade-off, in which the densification and the decision on the ISD depends on the height of the UAVs.

Finally, we show how the bandwidth affects to the Capacity coverage. One of the advantatges of the mmWave communications, besides the beamforming gain, is the increase of bandwidth available for connectivity. The IEEE standards have approved four possible bandwidth in mmWave communications: 100,200,300 and 400 MHz. In Figure 2-17, we show the Capacity coverage for those possible bandwidth. We consider the UAV at medium height, and a system with interference mitigation (i.e. noise-limited system). While in 100-200 MHz bands the coverage is slightly reduced, there is no such a difference when we increase the bandwidth up to a 300-400 MHz bands.

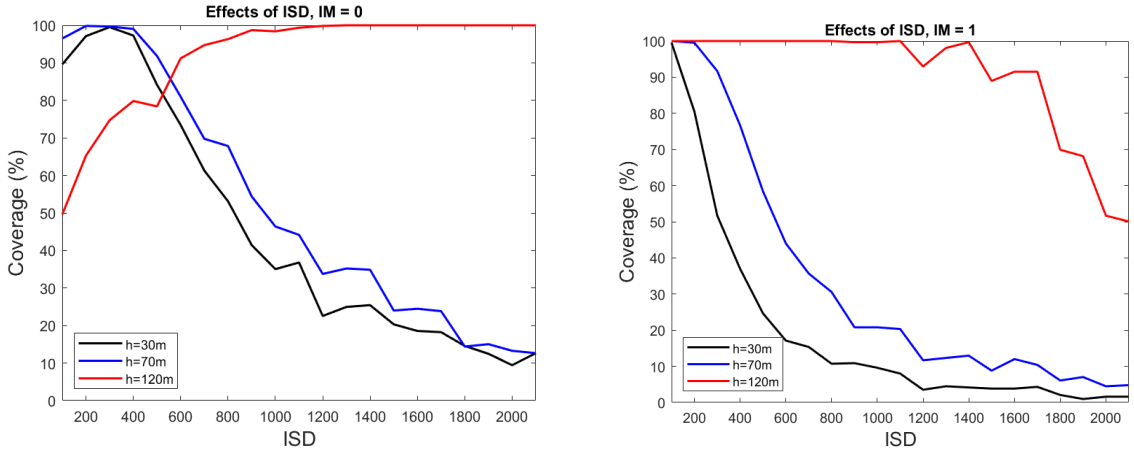

(a) (b)

Figure 2-16 Capacity coverage analysis with a threshold of 1Mbps and BW=200 Mhz. factor, (a) Interference-limited (b) Interference mitigation (noise-limited system)

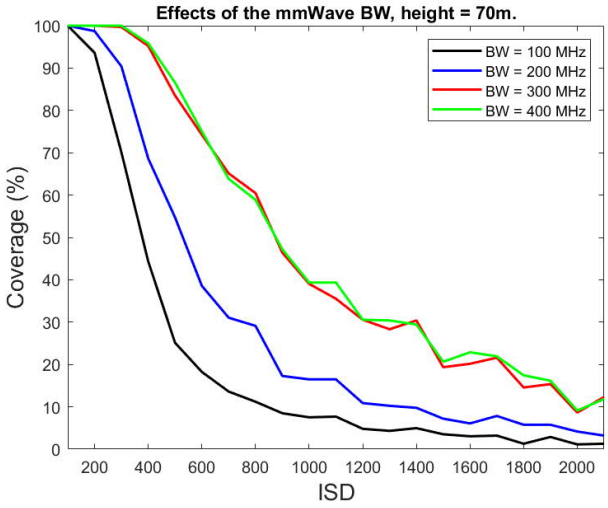

Figure 2-17 Effects of the mm Wave bandwidth to the capacity coverage (Threshold = 1Mbps)

2.5 Analysis of propagation characteristics of UAV base stations using ray tracing

Unmanned aerial communication platforms have been recently considered as effective solutions to provide homogeneous and extended network coverage to terrestrial users, and they are effective for critical missions. The UAV base station experiences different propagation environments compared with the terrestrial BSs. The objective of this study was to investigate the characteristics of signal propagation of drone-based communication system in a real world city environment. This study was carried out by performing comprehensive 3D ray tracing simulations and by utilizing an analytical model for the UAV propagation. For this work, we have considered a 3D building data of downtown area of a European urban city i.e., Helsinki, as shown in Figure 2-18. Unlike, hypothetical regular manhattan type building grid, the target area has buildings of irregular shapes and different heights, where the maximum height of the buildings is limited to 28 m. The signal coverage with drone heights i.e., from 50m up to 250m at different frequencies of operation i.e., from 3.5 GHz to 180 GHz is analyed in this work. Figure

2-19 shows the two dimensional plan of the coverage area, and the position of the drone and the Rx points are highlighted with the blue and red mark, respectively. It is assumed that both the Tx and Rx ends are equipped with isotropic antenna. Moreover, another target of this research work was to study the validity of a previously proposed geometrical Line-of-sight (LoS) probability model between the ground user and the drone base station, and proposes a new set of parameter values for analytical LoS probability and a large scale path loss model based on 3D ray tracing simulation results.

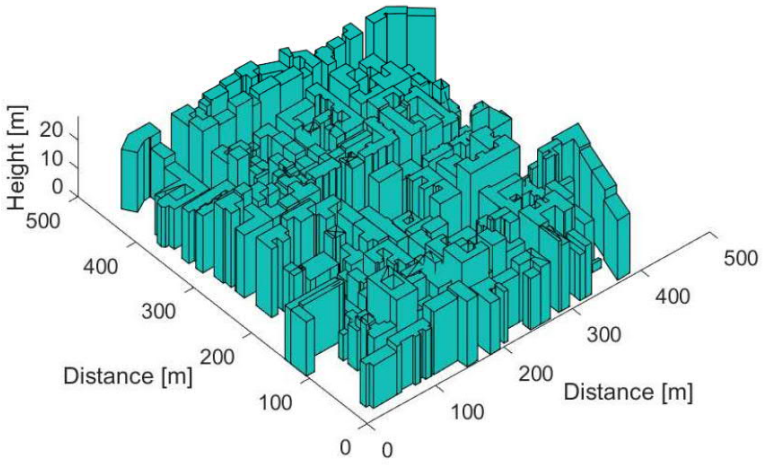

Figure 2-18 Three dimensional view of buildings of the considered target area

Figure 2-19 Distribution of receiver points in the target area

2.5.1 Simulation approach/methodology

In the first part of this work, a comprehensive campaign of 3D ray tracing simulations was carried out by using a MATLAB based ray tracing tool developed at Aalto University. The indigenously developed RT tool is based on Image Theory (IT), and is basically used for finding the propagation paths with mutliple reflections and diffractions along with the LoS path. The RT tool computes the received power levels and also provides the information about the LoS status between the Tx and the Rx. Moreover,

the received power levels are also computed by using analytical model for UAV, and a comparison between the results obtained through ray tracing and analytical model is presented. We have mainly considered the propagation analysis in the downlink direction. The maximum transmission power at the drone BS was set to 30 dBm i.e., 1 watt, and no power control is assumed at the BS.

2.5.2 Simulation results

The acquired 3D ray tracing simulation data is post processed to obtain the information about the percentage of outdoor terrestrial ground users in LoS with the drone, while drone flying at different heights. Figure 2-20 shows the percentage of outdoor ground UEs in LoS condition as a function of drone heights. It can be clearly seen in Figure 2-20 that in drone based communication the height of the drone has a direct impact on the LoS condition, and the obtained ray tracing simulation results show that the LoS percentage increases with the increase in the height of the flying drone. In a considered case study environment, at 50 m drone height there were only 14% ground users in LoS with the drone, however, at 200m drone height the LoS percentage is increased to 54%, and the growth of LoS connections continues with the increasing height of the UAV.

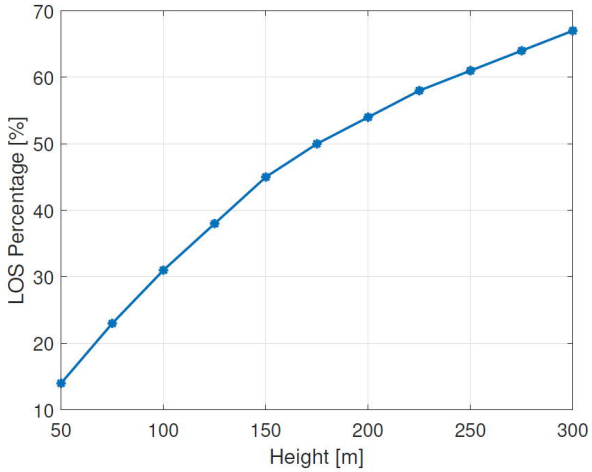

Figure 2-20 Percentage of outdoor ground UEs in LoS with drone flying at different heights

The second metric considered for the analysis is the mean received power-level, and Figure 2-21 shows a surface plot of mean received power-level for different considered frequencies and drone heights. It was found that for low flying drone, i.e., at 50m, the distance between the terrestrial user and the UAV is low, and it is expected to have a high received power for low flying drone. However, at the same time the LoS probability between the flying drone and the ground UE is also small for drone flying at lower heights. Interestingly, it was found that with the increase in the drone height from 50m to 75m, although the distance between the terrestrial user and the drone is increased, however, at the same time LoS probability also increases with the drone height, and that results in a better mean received signal power-level at 75m compared with the 50m drone height. Above 75 m, the mean received power-level again starts to decrease with the increase in drone height. In simple words, for a considered environment and user grid, the drone altitude of 75m is found as an optimal height in terms of received power. There is a sharp change in the received power-level while migrating from 3.5 GHz to 28 GHz and 60 GHz as the mean received power-level drops by almost 20.5 dB and 33.5 dB, respectively. It was found that due to significantly high atmospheric absorption at 60 GHz compared to 80 GHz, despite of higher frequency of operation the mean power-level is found slightly better at 80 GHz compared to 60 GHz. After 80 GHz a gradual drop in mean received power-level is observed up to 180 GHz.

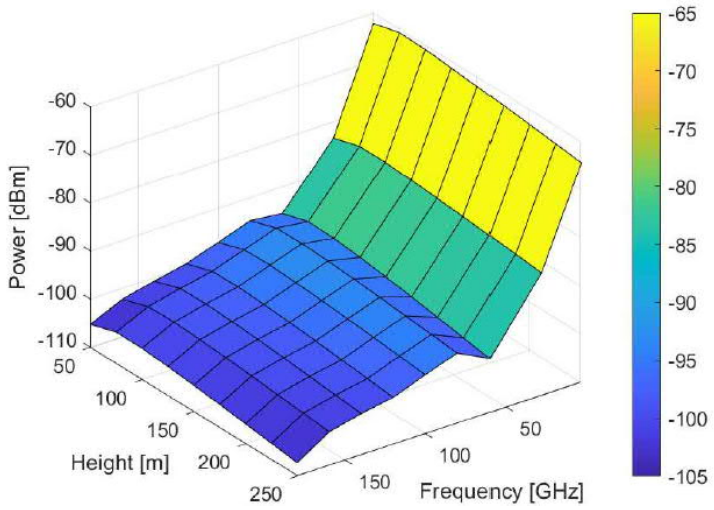

Figure 2-21 Mean received power level at different frequencies and drone heights

Figure 2-22(a-d) show the LoS probability against the elevation angle in degrees for the ray tracing simulation data at different heights of the flying drone. It is important to highlight here that the simulation data shown in Figure 2-22 is obtained through ray tracing simulations based on the simulation environment and user distribution shown in Figure 2-19. In Figure 2-22, the analytical LoS probability model presented at [AKL14] is considered as a reference model, and a tuned model is acquired by using a curve fitting on the ray tracing simulation data. As we have considered only a single drone for covering the area under consideration, therefore, elevation angle has a wide spread at low flying drone altitudes, and it was found that the spread of the elevation angle decreases with the increase in the height of the drone. In addition, at large elevation angles, i.e. above 75 degrees, the drone is almost on the top of the user and accordingly the LoS probability is high. Interestingly, significant difference was found between the reference and our proposed tuned LoS probability model. The reference model is found clearly over optimistic as the LoS probability given by the reference model is considerably high in comparison with the obtained ray tracing simulation data.

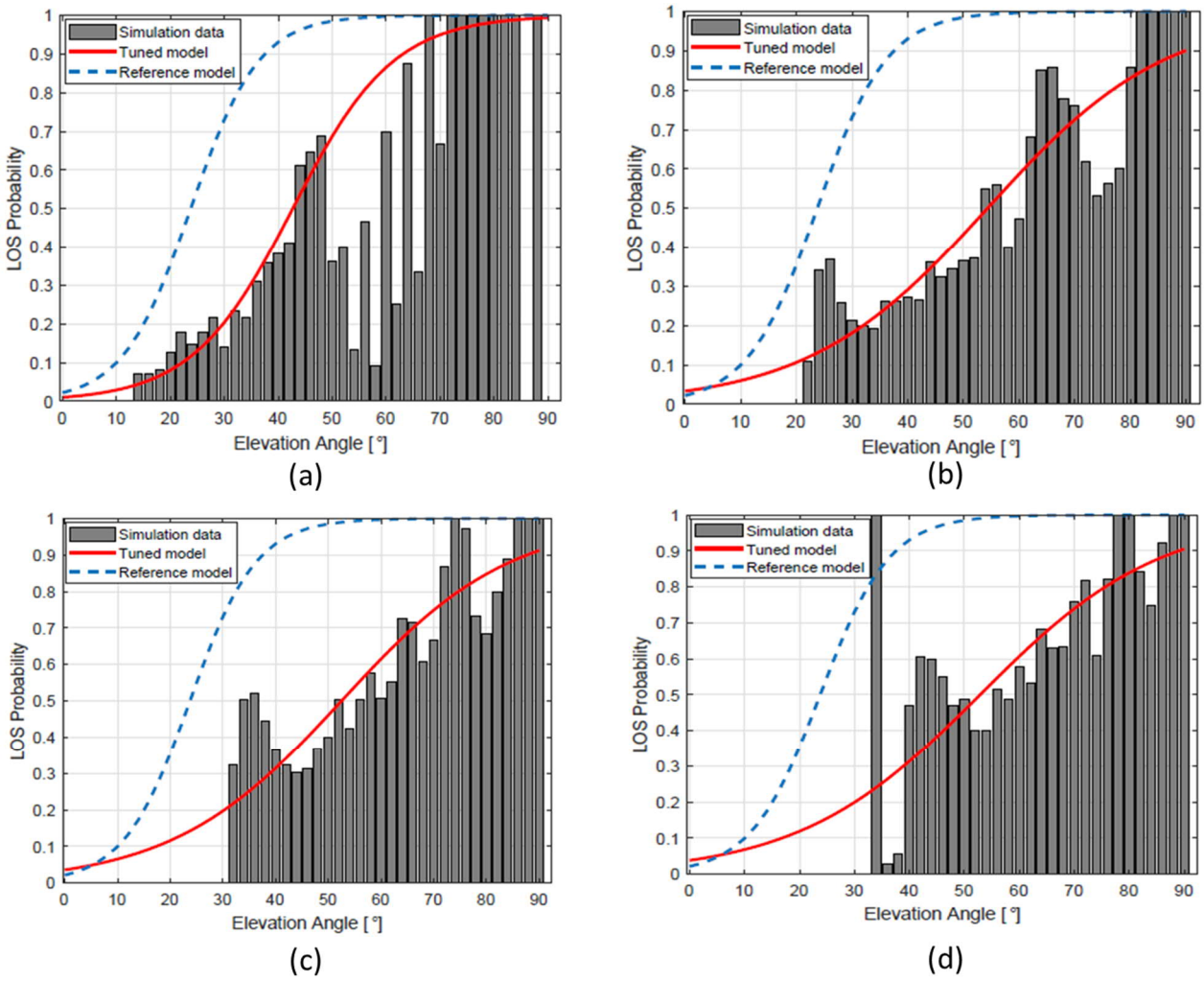

Figure 2-22 LoS probability acquired through ray tracing simulation data and through analytical LoS probability models at, (a) 50m, (b) 100m, (c) 150m, and (d) 200m

2.6 mmWave channel estimation with delay-domain sparsity

Precise channel estimation is a prerequisite for the communication and localization that constitute PriMO-5G use cases. Recent studies on mmWave band show that the channel exhibits a sparse behaviour which is characterized by only a few dominant paths in propagation [GZP+19]. In this section, we introduce a novel method of wideband channel estimation that utilizes delay-domain sparsity. The proposed method is inspired by a recently developed signal processing technique, namely geometric sequence decomposition with *k*-simplexes transform (GSD-ST) [LLS21].

2.6.1 Background and motivation

Wideband mmWave channel can be characterized by a few dominant tap coefficients. Thus, the principle of compressed sensing (CS) has attracted the studies of channel estimation to reduce the pilot overhead. However, the application of CS to the channel estimation has two well-known technical issues. First, the excess delay appears in continuous time. Hence, it is not guaranteed that the channel

impulse response (CIR) occurs exactly at the sampling grid. Consequently, forming a complete sparse vector is difficult, and we typically deal with an approximately sparse vector with energy dispersion. This makes a channel reconstruction error inevitable. Second, orthogonal matching pursuit (OMP), which is a popular implementations of CS, sequentially selects the basis with the highest correlation. Hence, it is vulnerable to inter-path interference coming from the non-orthogonality among multipaths. So, the required number of bases must be numerous, which in turn requires high computational complexity.

To address these issues, we propose an entirely different approach. Assume that a channel consists of L mutipaths. Different from the conventional OMP, our method directly obtains the parameters of L multipaths from pilot estimation. To achieve this, we use the fact that each peak in time domain can be viewed as a geometric sequence in frequency domain. It means that we can think of a CIR as a non-orthogonally superposed L geometric sequences in frequency domain. Therefore, the sparse channel estimation problem is converted into the acquisition of the parameters of the geometric sequences while we can observe only the superposition of the sequences. The transformed problem can be solved efficiently owing to the recently developed method of GSD-ST [LLS21]. Here, sampled radio waves in time domain are described as geometric sequences to distinguish multiple random access requests. The proposed method has a notable property that it enables the error-free estimation of the whole bandwidth with only a few pilot symbols, on the condition that the pilot estimation is perfect and the excess delay is bounded to a certain value.

2.6.2 System model

Assume an OFDM system with N subcarriers where the subcarrier spacing is Δf . Let $\mathbf{x} \in \mathbb{C}^N$ be a sequence of an OFDM symbol in frequency domain. $\mathbf{x}[n]$ is the n-th element of $\mathbf{x}$ and denotes the symbol transmitted through the n-th subcarrier. The transmitted signal in the continuous time domain $x(t)$ is given by

$$x(t) = \sum_{n=0}^{N-1} x_n(t) = \sum_{n=0}^{N-1} \mathbf{x}[n] e^{\frac{j2\pi n\Delta f t}{N}}, \tag{2.9}$$

where $x_n(t)$ represents the continuous signal passed through digital-to-analog converter (DAC) after N -point inverse fast Fourier transform (IFFT) of $\mathbf{x}[n]$. For brevity, we neglect the cyclic-prefix, i.e., the symbol duration is $1/\Delta f$.

Let L be the number of multipaths ($L \leq N$). The CIR, $h(t,\tau)$, can be modeled by the sum of Dirac-delta functions as follows:

$$h(t,\tau) = \sum_{l=0}^{L-1} \alpha_l \delta(t - \tau_l), \tag{2.10}$$

where α_l and τ_l are the complex channel gain and the excess delay of l -th path, respectively.

Let $\mathbf{s} \in \mathbb{C}^N$ denote the discrete signal obtained by N -point fast Fourier transform (FFT) after the sampling of the signal experiencing the wireless channel at the receiver. Thus, $\mathbf{s}$ is given by

$$\mathbf{s} = \mathrm{F}(x * h) = \mathbf{x} \odot \mathbf{h} = \{\mathbf{x}[n] \sum_{l=0}^{L-1} \alpha_l e^{-j2\pi n\Delta f \tau_l}\}_{n=0}^{N-1}, \tag{2.11}$$

where $*$ and $\odot$ denote the operators of the convolution and the Hadamard product, respectively. Here,

$\mathbf{h} \in \mathbb{C}^N$ is the channel frequency response (CFR), which is the N-point FFT of $h(t,\tau)$.

We consider that $\mathbf{x}$ consists of the equispaced pilot symbols and the data symbols. Let $\mathbf{x}_T \in \mathbb{C}^P$ denote the sequence of pilot symbols for channel estimation, which can be represented as follows:

$$\mathbf{x}_T = \{\mathbf{x}[pK]\}_{p=0}^{P-1}, \tag{2.12}$$

where K is the index spacing of the pilot symbols.

If we assume β is the predetermined transmitted pilot symbol, i.e., $\mathbf{x}_T[p] = \beta$ for all p, then $\mathbf{s}_T$ denoting the known part of $\mathbf{s}$ is given by

$$\mathbf{s}_T = \{\sum_{l=0}^{L-1} \beta\alpha_l e^{-j2\pi pK\Delta f \tau_l}\}_{p=0}^{P-1}. \tag{2.13}$$

2.6.3 Proposed channel estimation method

Our objective is to obtain accurate channel estimation with the minimum number of required pilots. This can be expressed by maximizing the spectral efficiency (SE) as follows:

$$\text{SE (bps/Hz)} = \frac{(K-1)}{K}(1-q)\log_2 M, \tag{2.14}$$

where q and M denote the symbol error rate (SER) and the modulation order, respectively.

Different from conventional CS methods such as OMP, we approach the sparse channel estimation problem by directly extracting the parameters of the L multipaths. The sequence of the l-th path within $\mathbf{s}_T$ is as follows:

$$\beta\alpha_l\{1, e^{-j2\pi K\Delta f\tau_l}, e^{-j2\pi 2K\Delta f\tau_l}, e^{-j2\pi 3K\Delta f\tau_l}, \cdots\}. \tag{2.15}$$

This is indeed a geometric sequence with the initial term of $\beta\alpha_l$ and the common ratio of $e^{-j2\pi K\Delta f\tau_l}$. Therefore, $\mathbf{s}_T$ is in fact a non-orthogonal superposition of L geometric sequences. Since a geometric sequence is characterized by two parameters (initial term and common ratio), the entire CFR, $\mathbf{h}$, can be reconstructed by obtaining $2L+1$ unknowns: $\mathbf{a}$, $\mathbf{r}$, and L. Here, $\mathbf{a}$ and $\mathbf{r}$ are the vectors of initial terms and common ratios of the geometric sequences that consist of $\mathbf{s}_T$.

To obtain the unknowns, we employ GSD-ST, which is a mathematical technique of handling geometric sequences [LLS21]. The proposed channel estimation scheme is divided into three phases.

2.6.3.1 Phase 1: obtaining L

Let $\hat{L}$ be an estimate of L. Firstly, let us make $\hat{L}$-dimensional vertices out of $\mathbf{s}_T$. The k-th vertex, which is denoted by $\mathbf{v}_k \in \mathbb{C}^{\hat{L}}$, is defined as

$$\mathbf{v}_k = [\mathbf{s}_T(k), \cdots, \mathbf{s}_T(k+\hat{L}-1)]^T. \tag{2.16}$$

Secondly, let $\chi_{\hat{L}}(\mathbf{v}_k, \cdots, \mathbf{v}_{k+\hat{L}-1})$ be the $\hat{L}$-simplex by connecting the origin point and given $\hat{L}$

consecutive vertices. In addition, let $\Lambda(\chi_{\hat{L}}(\mathbf{v}_k,\cdots,\mathbf{v}_{k+\hat{L}-1}))$ denote the volume of the simplex, i.e.,

$$\Lambda(\chi_{\hat{L}}(\mathbf{v}_k,\cdots,\mathbf{v}_{k+\hat{L}-1}))=\frac{\det([\mathbf{v}_k,\cdots,\mathbf{v}_{k+\hat{L}-1}])}{\hat{L}!}. \quad (2.17)$$

Thirdly, we define $\Omega_{\hat{L}}$ as the series of the volumes of $\hat{L}$-simplexes, i.e.,

$$\Omega_{\hat{L}}=\{\Lambda(\chi_{\hat{L}}(\mathbf{v}_k,\cdots,\mathbf{v}_{k+\hat{L}-1}))\}_{k=0}^{P-\hat{L}}. \quad (2.18)$$

According to Theorem 1 in [LLS21], $\Omega_{\hat{L}}$ becomes a non-zero geometric sequence if and only if $\hat{L}=L$.

2.6.3.2 Phase 2: obtaining $\mathbf{a}$ and $\mathbf{r}$

In the second phase, we obtain $\mathbf{a}$ and $\mathbf{r}$ with the information of known L. We create a series of L-simplexes from a lexicographical combination of $2L$ samples of $\mathbf{s}_T$. For this, firstly compose $L+1$ consecutive vertices, $\mathbf{v}_0,\cdots,\mathbf{v}_L$. Next, let $\aleph$ denote the series that we utilize. Its length is $L+1$, and it is formed by the lexicographical combination of the vertices as follows:

$$\aleph=\{\chi_L(\mathbf{v}_0,\mathbf{v}_1,\cdots,\mathbf{v}_{L-1}),\chi_L(\mathbf{v}_0,\mathbf{v}_1,\cdots,\mathbf{v}_L),\ \cdots,\chi_L(\mathbf{v}_0,\mathbf{v}_2,\cdots,\mathbf{v}_L),\chi_L(\mathbf{v}_1,\mathbf{v}_2,\cdots,\mathbf{v}_L)\}. \quad (2.19)$$

According to Theorem 2 in [LLS21], we can construct an L-th order polynomial equation whose roots are equal to $\mathbf{r}$. After $\mathbf{r}$ is obtained, $\mathbf{a}$ can be obtained by a simple matrix pseudo-inversion.

2.6.3.3 Phase 3: extracting channel parameters

The extraction of the channel parameters $\alpha_0,\cdots,\alpha_{L-1}$ and $\tau_0,\cdots,\tau_{L-1}$ is straightforward. That is,

$$\hat{\alpha}_l\leftarrow\mathbf{a}[l]/\beta \text{ and } \hat{\tau}_l\leftarrow\frac{-\angle\mathbf{r}[l]}{2\pi K\Delta f}, \quad (2.20)$$

where $\angle(\cdot)$ is the phase of a complex-valued input. We emphasize that the only source of the error in the proposed scheme is phase ambiguity. It occurs when the excess delay happens to be large such that $\angle\mathbf{r}[l]$ stretches out of the range of $[-2\pi,0)$.

2.6.4 Numerical results

The performance of the proposed scheme is evaluated via Monte Carlo simulation experiments with 1024-QAM. We compare the proposed scheme with OMP [SM15] with the 5000 bases of partial discrete Fourier transform (DFT) matrix. Furthermore, the cubic interpolation [CEP+02] and the theoretical bound of the perfect CFR are provided as references of the low and high performances, respectively. We assume that the excess delay values follow the truncated exponential distribution with τ_{max}.

Figure 2-23 shows the SE to demonstrate that the proposed method can acheive the error-free estimation depending on τ_{max}. The proposed method gradually loses its ability of error-free channel estimation as τ_{max} increases. This is because the excess delays leading to the phase ambiguity occur stochastically. However, the performance of the proposed method is still superior to other methods.

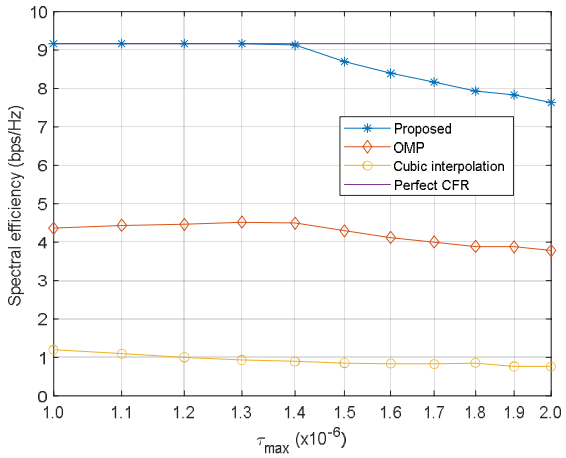

Figure 2-23: SE according to τ_{max} ($L = 4$, $1/\lambda = 5\times10^{-7}$, and $K = 12$)

The effect of the pilot symbol density is depicted in Figure 2-24. Here, we define the pilot density as $\rho(=1/K)$. In this experiment, τ_{max} is considered to be infinity. It is observed that the performance of the proposed scheme gradually approaches the theoretical limit even with the infinite τ_{max}. On the other hand, OMP has the limited capability to estimate the multipaths that are extremely close to each other. When ρ becomes 15%, even cubic interpolation shows better performance than OMP. This implies that increasing the pilot density does not help OMP unless higher sampling rate is supported. Conversely, the performance of cubic interpolation increases with ρ due to the nature of element-wise correlation.

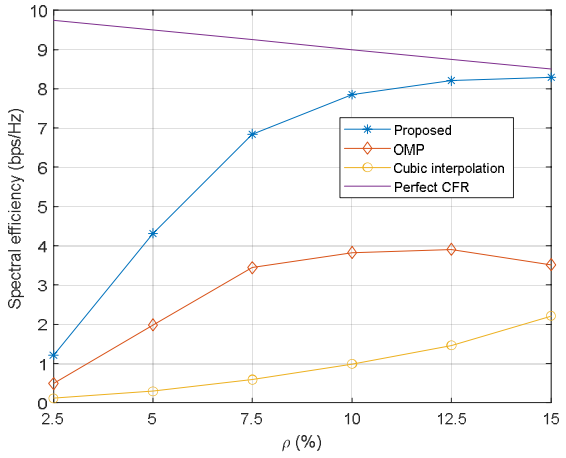

Figure 2-24: SE according to ρ ($L = 4$ and $1/\lambda = 5\times10^{-7}$)

In summary, by utilizing the fact that the channel of each multi-path element is a geometric sequence, we can achieve an error-free estimation of the whole bandwidth with only a few pilot symbols. The recently developed method of GSD-ST lays the foundations for the proposed channel estimation scheme.

2.7 Full-Duplex Interference Alignment in practical case

This section addresses practical performance and analysis of Full-Duplex(FD) Interference Alignment(IA) scheme we proposed on D3.1. First, we analyze the effect of practical errors. Frequency offset, and sync error are considered practical errors.

2.7.1 Review of Full-Duplex Interference Alignment

In section 5.3 of D3.1, we proposed an interference alignment scheme for FD, which is called Code Division Duplex-Spatial Division Multiple Access(CDD-SDMA). The system model consists of N RF-chains and M antenna elements, and L cells. To eliminate the interference, it is assumed that $M \geq 2LN$. Full channel state information (CSI) assumed to be known at FD BS, and the channel is assumed to remain unchanged for $2L$ symbol durations to divide other users' signals.

Let $\mathbf{A}_l$ be $2LN \times 2LN$ analog precoder and $\mathbf{U}_l$ be the digital precoder of users in cell l. Let us define the matrix $\mathbf{F}_l$, which the ith row consists of each user's channel coefficients of the ith user in cell l, and $\mathbf{C}$ be the $2L \times 2L$ codebook for 2L symbol times for each downlink and uplink. The method of constructing the precoders $\mathbf{A}_l$ and $\mathbf{U}_l$ is to zero force other users' signals and other BS signals by $\mathbf{F}_l \times \mathbf{A}_l \times \mathbf{cU}_l$ be diagonal matrix where $\mathbf{cU}_l$ is the coded precoder.

2.7.2 Practical case analysis

Our proposed scheme can guarantee twice spectral efficiency compared to Half-Duplex(HD) with perfect estimation. However, the practical case may have non-ideal measures such as non-perfect channel estimation, frequency offset, etc. We will analyze the effect of frequency offset sync error on our proposed scheme. We consider the OFDM mmWave FD system. The OFDM baseband signal expression of frequency offset and sync error can be expressed as below:

$$\boldsymbol{e}_{error}(k,p) = e^{\frac{j\pi\Delta kp}{P}} e^{\frac{j\pi k\Delta p}{P}} e^{\frac{j\pi\Delta k\Delta p}{P}}, \tag{2.21}$$

where k is subcarrier index, and p is the symbol time. Thus the 2L symbol-time signal sum with error of the ith downlink user in the lth cell can be expressed below.

$$\boldsymbol{y}_i^{(l)} = \boldsymbol{f}_{\boldsymbol{i}}^{(l)} \boldsymbol{x}_{code}^{(l)}(p) \circ \boldsymbol{e}_{error}(k,p) + \sum_{l' \neq l}^{2LN} \boldsymbol{f}_i^{(l)(l')} \boldsymbol{x}_{\boldsymbol{ifft\,error}}^{(l')} + \sum_{l'=1}^{L} \sum_{j=1}^{2LN} g_{ij}^{(l)(l')} v_j^{(l)(l')} \beta_j^{(l)(l')} e^{\frac{j\pi\Delta kp}{P}} e^{\frac{j\pi k\Delta p}{P}} e^{\frac{j\pi\Delta k\Delta p}{P}} + \boldsymbol{z}_i^{(l)} \tag{2.22}$$

This can be simplified as

$$\boldsymbol{y}_i^{(l)} = desired\ signal\ part + other\ BS\ signal + uplink\ user\ to\ downlink\ interference + noise.$$

The desired signal part consists of channel $\boldsymbol{f}_{\boldsymbol{i}}^{(l)}$, coded signal $\boldsymbol{x}_{code}^{(l)}(p)$, and error $\boldsymbol{e}_{error}(k,p) = e^{\frac{j\pi\Delta kp}{P}} e^{\frac{j\pi k\Delta p}{P}} e^{\frac{j\pi\Delta k\Delta p}{P}}$. Other BS signal consists of channel from other BS to downlink $\boldsymbol{f}_i^{(l)(l')}$ and errored coded signal from cell l', $\boldsymbol{x}_{\boldsymbol{ifft\,error}}^{(l')}$. The uplink user to downlink interference part consists of user j of cell l' to user i of cell l $g_{ij}^{(l)(l')}$, uplink digital precoder $v_j^{(l)(l')}$, uplink user signal $\beta_j^{(l)(l')}$, and error. For the last, $\boldsymbol{z}_i^{(l)}$ represents the noise.

The point to analyze the effect of practical errors, we need to focus on the non desired interference left after multiply DFT matrix and code to $\boldsymbol{y}_i^{(l)}$. The signal expression of DFT coded signal is like below.

$$\mathbf{y}_{dft}^{(l)} = \mathbf{W}^{DFT} \mathbf{y}_i^{(l)} \circ \mathbf{c}_{2l-1} = \mathbf{W}^{DFT} \circ \mathbf{c}_{2l-1} \left(\mathbf{f}_{i_t}^{(l)} \mathbf{x}_{\boldsymbol{code\ error}}^{(l)} + \sum_{l' \neq l}^{2LN} \mathbf{f}_i^{(l)(l')} \mathbf{x}_{\boldsymbol{code\ error}}^{(l')} + \sum_{l'=1}^{L} \sum_{j=1}^{2LN} g_{ij}^{(l)(l')} v_j^{(l)(l')} \beta_j^{(l)(l')} e^{\frac{j\pi\Delta kp}{P}} e^{\frac{j\pi k\Delta p}{P}} e^{\frac{j\pi\Delta k\Delta p}{P}} + \mathbf{z}_i^{(l)} \right) \tag{2.22}$$

Where $\mathbf{W}^{DFT}$ is DFT matrix and $\mathbf{c}_{2l-1}$ is code for cell l downlink. The interference term can be written as below.

$$\mathbf{W}^{DFT} \circ \mathbf{c}_{2l-1}\left(\sum_{l' \neq l}^{2LN} \mathbf{f}_i^{(l)(l')} \mathbf{x}_{\boldsymbol{code\ error}}^{(l')} + \sum_{l'=1}^{L}\sum_{j=1}^{2LN} g_{ij}^{(l)(l')} v_j^{(l)(l')} \beta_j^{(l)(l')} e^{\frac{j\pi\Delta kp}{P}} e^{\frac{j\pi k\Delta p}{P}} e^{\frac{j\pi\Delta k\Delta p}{P}}\right) \quad (2.23)$$

To analyze this interference, we changed the effect of the interference term's expression into polar coordinate with approximation as below[WTW+03].

$$\mathbf{y}_{dft}^{(l)}(k,p) = \frac{\left|\mathbf{y}_{dft}^{(l)}(k,p)\right|}{2\pi\sigma^2} e^{-\frac{\left|\mathbf{y}_{dft}^{(l)}(k,p)\right|^2 + \left|\mathbf{x}_{error}^{(l)}\right|^2 - 2\left|\mathbf{y}_{dft}^{(l)}(k,p)\right|\left|\mathbf{x}_{error}^{(l)}\right| cos\left(tan^{-1}\left(\frac{Re\left\{\mathbf{y}_{dft}^{(l)}\right\}}{Im\left\{\mathbf{y}_{dft}^{(l)}\right\}}\right) - tan^{-1}\left(\frac{Re\left\{\mathbf{x}_{error}^{(l)}\right\}}{Im\left\{\mathbf{x}_{error}^{(l)}\right\}}\right)\right)}{2\pi\sigma^2}} \quad (2.24)$$

Where $\mathbf{x}_{error}^{(l)}$ is desired signal part with error.

The noise term is $\mathbf{W}^{IDFT}\mathbf{z}_i^{(l)} \circ \mathbf{c}_{2l-1}$. With respect to DFT matrix and code magnitude to be 1, the noise term will have the same distribution.

From the analysis above, practical errors could affect the scheme. However, it could work with additional gaussian expressed interference.

2.7.3 Practical case result

The analysis result above shows the effect of practical errors can be approximated to gaussian distribution. To support our analysis, we simulated the effect of practical errors. The result of the simulation is as below

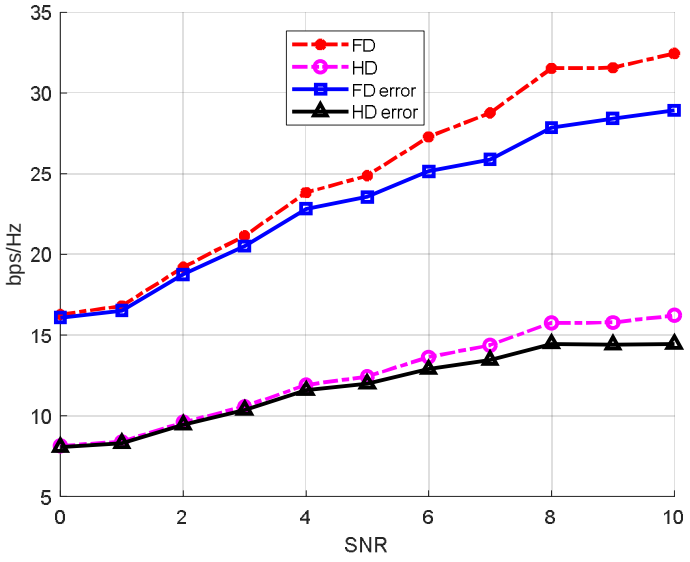

Figure 2-25. Single-cell performance of proposed scheme

The simulation environment consists of 4 antennas per BS and 4 users in a cell using 2 subcarriers. Sync error and frequency offset follow the gaussian distribution with variance $\frac{1}{10}$ of symbol duration and subcarrier bandwidth. The spectral efficiency is calculated by the capacity of SINR of signal. In Figure 2-25, red line represents FD without sync and frequency offset error, and blue line represents the FD with sync and frequency error. The pink and black line represent HD without error and with error each. From Figure 2-25, we can figure out little effect of sync error and frequency offset at low SNR and its

effect grows with SNR. From the above result, we can figure out that our proposed scheme could perform about 60% higher spectral efficiency to HD even with practical errors.

2.8 Grant-free multiple access for URLLC

In the previous 4G communication, the uplink random access is grant-based so that a 4-way handshaking must be completed before a data transmission from user equipments (UEs) to a base station (BS). This procedures cause severe delays at least 4 times of the transmission time interval (TTI) and decrease the spectral efficiency, especially as the latency requirement becomes tight. Furthemore, the hybrid automatic repeat request (H-ARQ) employed for achieving reliability cannot work appropriately due to the low latency requirement. Recently, a grant-free multiple access (GFMA) has been proposed to overcome these limitations and meet the high reliability requirements of a URLLC. URLLC services are considered as the most challenging applications in 5G or future cellular systems, and their typical use cases include immersive virtual reality (IVR) which can be supported by GFMA.

We consider an uplink large-scale antenna system as illustrated in Figure 2-26, where each of BS is equipped with M antennas and each of U UEs is equipped with a single antenna. Also, we configure the time-frequency sub-channels with a sub-frame with a duration of T_s and the sub-band bandwidth W_s. Within each sub-channel, the channel state is assumed to be static so that the $M \times 1$ SIMO spatial small scale block fading, denoted by h_j, does not change, while the large scale fading β_j only depends on the location of UE and does not change also within the scheduling period. We assume a perfect non line-of-sight (NLoS) propagation so that the small scale fading is modeled by a Rayleigh distribution. The UEs are divided into scheduling groups and then the BS allocates the sub-channels to the scheduling groups. The UEs allocated in the same sub-channel access to the BS by using space division multiple access (SDMA) and every UE with a new packet arrival gets activated and transmits by using the allocated sub-channel with a size of $N = W_s T_s$ symbols. For analytical tractability, it is assumed that the packet arrival follows a Poisson distribution with the average arrival rate of P_A. The BS and UE are assumed to operate in a perfect synchronization.

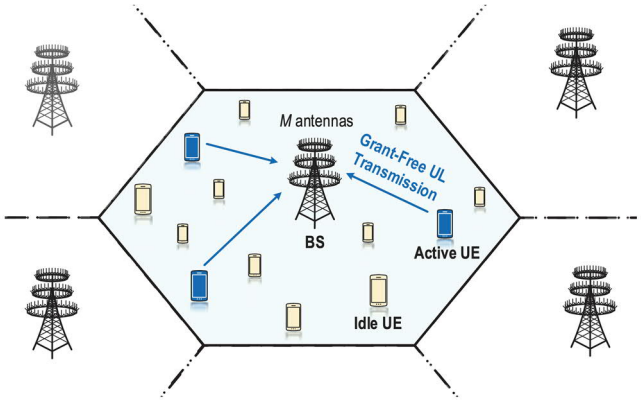

Figure 2-26 A grant-free multiple access system model

2.8.1 Channel and Signal Model

Let $\mathcal{O}$ be the set of users scheduled at the sub-channel of the sub-frame t and the sub-band f. Denote x_j the transmission block of user j in $\mathcal{O}$, then the $M \times N$ received signal matrix Y at the BS of interest can be expressed as

$$\mathbf{Y} = \sum_{j \in \mathcal{O}} \sqrt{\beta_j} \mathbf{h}_j \mathrm{x}_j^{\mathrm{H}} \mathbb{I}_j + \mathbf{V}, \qquad (2.25)$$

where $\mathbb{I}_j$ is the indicator function for the activation of user j and $\mathbf{V}$ is the $M \times N$ matrix for the thermal noise and other-cell interference signals. The transmission block x_j has L symbols for its pilot sequence and $N - L$ symbols for data so that we can write x_j as $\mathrm{x}_j = \left[\sqrt{p_j^{\mathrm{tr}}}\psi_j^{\mathrm{H}}, \sqrt{p_j^{\mathrm{dt}}}\mathbf{d}_j^{\mathrm{H}}\right]^{\mathrm{H}}$, where ψ_j denotes the pilot sequence of length L and $\mathbf{d}_j$ denotes the $N - L$ data symbol vector. Also, p_j^{tr} and p_j^{dt} denote the powers of the pilot sequence and the data symbols respectively. Here we assume that p_j^{tr} is determined by the full channel inversion power control for a given common target received power $\bar{p}^{\mathrm{tr}}$, i.e., $p_j^{\mathrm{tr}} = \bar{p}^{\mathrm{tr}}\beta_j^{-1}$. Let $\mathbf{Y} = [\mathbf{Y^{tr}}, \mathbf{Y^{dt}}]$ and $\mathbf{V} = [\mathbf{V^{tr}}, \mathbf{V^{dt}}]$, then Y^{tr} can be written

$$\mathbf{Y^{tr}} = \sum_{j\in\mathcal{O}} \sqrt{\bar{p}^{\mathrm{tr}}}\mathbf{h}_j\psi_j^{\mathrm{H}}\mathbb{I}_j + \mathbf{V^{tr}}. \qquad (2.26)$$

For the pilot sequence, we use Zadoff-Chu (ZC) sequences currently used in LTE-A. With a length of a prime number L, there are sequences with $L - 1$ different roots and L circularly shifted versions for each root so that there re $L^2 - L$ sequences available. Note that the cross correlation value is zero between the ZC sequences of circularly shifted versions in the same root and is constant of $\frac{1}{L}$ between sequences from different roots. As the cross correlation causes interferences and degrades the user detection performance, the sequence assignment must maximize the number of sequences of the samre root. Therefore, when $K = |\mathcal{O}|$ and the sequence length is L, the number of used roots is minimized to $\left\lceil\frac{K}{L}\right\rceil$.

2.8.2 The Neyman-Pearson Decision Criterion

The number of activated users in $\mathcal{O}$ at a time follows a binomial distribution $\mathcal{B}(K, P_A)$ because we asuume a Poisson random packet arriaval. At the BS side, for every sub-frame duration, it tries to detect which users transmitted signals by using the sequences and a correlation detector. Let define $Z_j = \left\|\mathbf{Y^{tr}}\psi_j\right\|^2$, then Z_j is the sufficient statistic for detecting user j from the received signal $\mathbf{Y}$ by using sequence ψ_j. Also, define $\tilde{v}_j^{\mathrm{tr}} = \mathbf{V^{tr}}\psi_j$. Then the sufficient statistic Z_j can be written as

$$Z_j = L\bar{p}^{\mathrm{tr}}\left\|\mathbf{h}_j\mathbb{I}_j\right\|^2 + \sum_{k\in\mathcal{O}\setminus\mathcal{O}_{r_j}} \bar{p}^{\mathrm{tr}}\|\mathbf{h}_k\mathbb{I}_k\|^2 + \left\|\tilde{v}_j^{\mathrm{tr}}\right\|^2, \qquad (2.27)$$

where $\psi_j^{\mathrm{H}}\psi_j = L, \left\|\psi_j^{\mathrm{H}}\psi_j\right\| = 1$ if $r_j \neq r_k$, and $\left\|\psi_j^{\mathrm{H}}\psi_j\right\| = 0$ if $r_j = r_k, j \neq k$. Le define $J = \sum_{k\in\mathcal{O}\setminus\mathcal{O}_{r_j}} \mathbb{I}_k$, then $J \sim \mathcal{B}\left(K - K_{r_j}, P_A\right)$. Because $\mathbf{h}_j, \mathbf{h}_k \sim \mathcal{CN}(0, L^2\mathrm{I}_M)$, Z_j follows a chi-square distribution with the degree of freedom (DoF) of $2M$ if J is determined. More specifically, $Z_j \sim \sigma_{J,active}^2\mathcal{X}_{2M}^2$ if $\mathbb{I}_k = 1$ and $Z_j \sim \sigma_{J,idle}^2\mathcal{X}_{2M}^2$ if $\mathbb{I}_k = 0$, where $\sigma_{J,active}^2 = \frac{L\bar{p}^{\mathrm{tr}} + J\bar{p}^{\mathrm{tr}} + L^2}{2}$ and $\sigma_{J,idle}^2 = \frac{J\bar{p}^{\mathrm{tr}} + L^2}{2}$. In fact, due to the large value of M, Z_j can be treated as a Gaussian random variable by using the central limit theorem.

By the NP decision criterion under a target detection nprobability P_D, the detection threshold Ω is the minimum value satisfying the detection probability condition as

$$\begin{aligned} 1 - P_D &\geq \underset{K-K_{r_j}}{P}\left(Z_j \leq \Omega \middle| \mathbb{I}_j = 1\right) \\ &= \sum_{q=0}^{K-K_{r_j}} \left(Z_j \leq \Omega \middle| \mathbb{I}_j = 1, J = q\right) P(J = q) \qquad (2.28) \\ &= \sum_{q=0}^{K-K_{r_j}} Q\left(\frac{\Omega/\sigma_{q,active}^2 - 2M}{\sqrt{4M}}\right) P(J = q), \end{aligned}$$

where $Q(\cdot)$ denotes the tail probability of the standard normal distribution. Note that the decision criterion with a threshold of Ω can cause false alarm and the false alarm probability P_{FA} can be calculated as

$$P_{FA} = P\left(Z_j > \Omega \middle| \mathbb{I}_j = 1\right)$$

$$= \sum_{q=0}^{K-K_{r_j}} \left(Z_j > \Omega | \mathbb{I}_j = 0, J = q\right) P(J = q) \qquad (2.29)$$

$$= \sum_{q=0}^{K-K_{r_j}} Q\left(\frac{\Omega/\sigma_{q,idle}^2 - 2M}{\sqrt{4M}}\right) P(J = q).$$

Note that there always exists a threshold that satisfies the detection probability condition. However, it is generally impossible to satisfy both the detection probability condition and the false alarm probability condition simultaneously. The resulted false alarm probability by the threshold from the detection probability condition shows the distance between $P\left(Z_j = z | \mathbb{I}_j = 1\right)$ and $P\left(Z_j = z | \mathbb{I}_j = 0\right)$ and thus it can evaluate a trade-off between the detection probability and the false alarm probability.

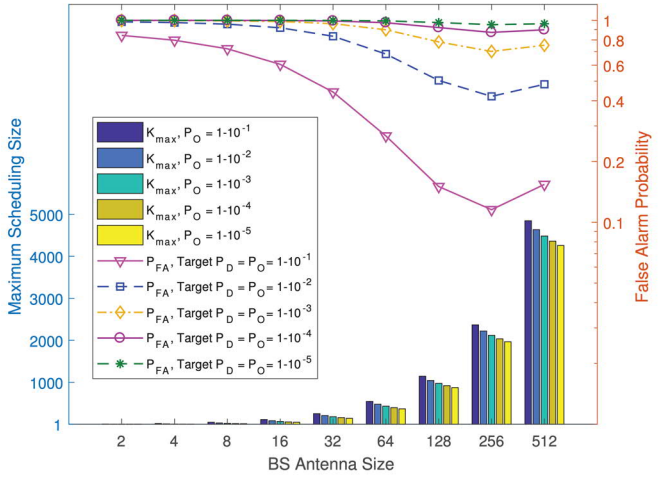

Figure 2-27 The false alarm probability and the maximum scheduling size versus the BS antenna size when $L = 97$ and $P_A = 0.1$

The false alarm probabilities of various detection schemes under various target detection probabilities are evaluated numerically in this section. For one sub-channel, the sub-frame duration is 1 ms and the sub-band bandwidth is 125 KHz. Using orthogonal frequency division multiplexing (OFDM) waveform with 25% cyclic prefix (CP) overhead, $N = 100$ symbols are used in a transmission block. The target received power $\bar{p}^{\text{tr}}$ is set to be 15 dB over the thermal noise and other- cell interference. Here, we consider the maximum scheduling size constrained by the packet arrival rate P_A, the BS antenna size M, and the outage probability P_O. Because, when ZF receiver is used at the receiver, the maximum supportable number of users is at most $M - 1$ to have non-zero rates. Thus, the maximum scheduling size is $K_{max} = \max K$, subject to $P(J \leq M - 1) \leq P_O$, where $J \sim \mathcal{B}(K, P_A)$. In addition, we used sufficiently large pilot length so that $L^2 - L \geq K_{max}$ for the simulations.

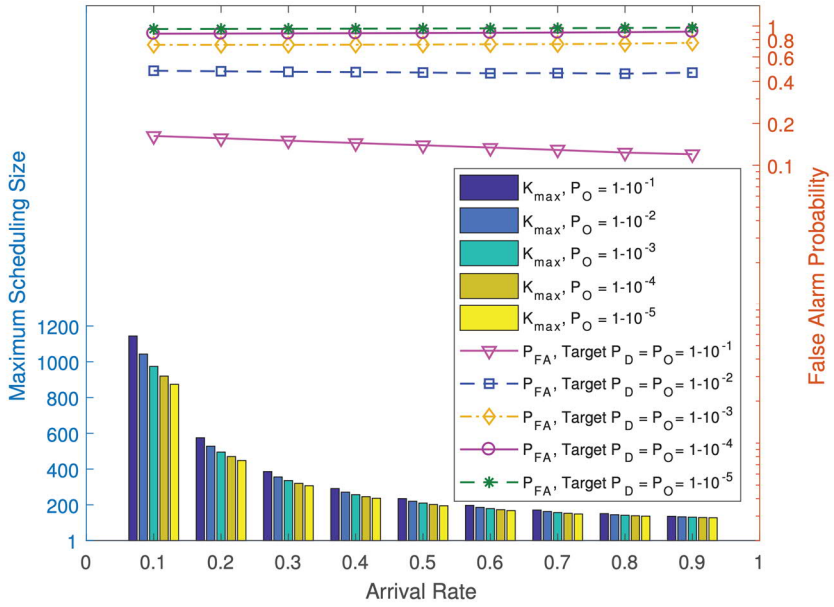

Figure 2-28 The false alarm probability and the maximum scheduling size versus the arrival rate when $M = 128$ and $L = 47$

In Figure 2-27, the false alarm probability and the maximum scheduling size are plotted. Here, we set the pilot length L = 97 because K_{max} increases up to 4846 as M increases to 512. In this figure, the false alarm probability dose not always decrease with the number of BS antennas. The reason is that as the number of antennas increases, the number of interferers also increases very rapidly. From this, the number of BS antennas at a given target detection probability can be seen to have some optimal value for a given false alarm probability. In Figure 2-28, the false alarm probability and the maximum scheduling size are shown when the arrival rate P_A changes from 0.1 to 0.9. Here, since the maximum scheduling size decreases significantly while the arrival rate increases, the number of active users at a time does not change a lot, and thus the false alarm probability decreases very slightly.

3 Radio transceiver and waveform design for PriMO-5G

3.1 Introduction

Within PriMO-5G, the vision of an end-to-end communication system for immersive video services was followed. To get closer to this vision, a number of enabling technologies have to be used. One of them is the mmWave communication which is already part of the 5G NR standard. The technology which is necessary for this has been investigated and described in section 3.2.

The forest fire fighting scenarios A and use case A1 from Deliverable D1.1 of PriMO-5G are the target applications for the technology presented in the following sections. Video capturing drones fly over the forest fire and send their video data to the incident commander truck via a stationary drone where all the video streams are aggregated. Therefore the link from this stationary drone to the incident commander truck needs to be capable of transferring this aggregated video data while at the same time the link in the opposite direction must provide low latency to enable a real time control of the video drones.

Due to new waveform designs which help enabling these requirements, transceivers need to be adapted to this, too. Section 3.3 focuses on a receiver that incorporates MMSE-Interference canceling which is important for quadrature amplitude modulation-filter-bank multi-carrier (QAM-FBMC) technology, a potential successor for CP-OFDM because of its high spectrum confinement characteristics and high spectrum efficiency which help the required data rates.

To enable low latency with high reliability at the same time, time-varying multiple access with spatial-frequency filter for mmWave is described in section 3.4. This technology helps to overcome the difficulties of wireless fading channels by proposing a new multiple access technology.

3.2 mmWave Radio Transceiver Design

This section deals with the description of the mmWave transceiver system provided by NI.

3.2.1 5G NR – 3GPP Specification

3.2.1.1 Numerology and Reference Signals

3GPP has defined a number of numerologies in Section 4.2 of TS 38.211. For frequency range 2 (FR2) which covers frequencies above 24.25 GHz, subcarrier spacings (SCS) of 60 kHz and 120 kHz are defined in TS 38.211 [3GPP20-38211]. In addition, a SCS of 240 kHz is defined for synchronization signal blocks (SSB), which include the Primary synchronization signal (PSS), the Secondary synchronization signal (SSS) and the Physical broadcast channel (PBCH). Next to channel state information reference signals (CSIRS) and the sounding reference signals (SRS), the SSBs are one means beamforming (BM) can be based on. 3GPP describes SSBs in Section 7.4.3 of TS 38.213 [3GPP20-38213], possible SSB patterns in Section 4.1 of TS38.213 [3GPP20-38213], CSIRS in Section 7.4.1.5 and SRS in Section 6.4.1.4 of TS 38.211 [3GPP20-38211].

For the PriMO-5G project transceiver, the particular band n257 (26.5 GHz to 29.5 GHz) is going to be used. With increasing frequency, the pathloss scales quadratically, yielding very high losses at the mmWave frequencies. For example, the path loss at 28 GHz is larger than that at 850 MHz by 30 dB; the pathloss ratio is increased by a factor of 1000. In addition, the aperture size is smaller. The aperture size ratio of 850 MHz to 28 GHz is 1:1085. As a result, beamforming is required to overcome the high Path Loss by utilizing multi-antennas at TX to direct the energy and at RX to increase the aperture size effectively [K18].

3.2.1.2 3GPP 5G NR Beam Management

3GPP does not specify how to perform analog or digital beamforming. However, it describes measurements on time and frequency resources. According to the 5G NR specification, the beam management consists of three main procedures [DPS18]:

1. Initial beam establishment
2. Beam adjustment
3. Beam recovery.

In Section 2.3 of deliverable D3.1 [PRIMO-D31], an overview on beam management is described. The 3GPP specifications describe how to configure these measurements, the measurement resources and the reporting of these measurements, how to perform the measurements and how to actually report the UE-based measurements back to the gNB. The UE needs to be capable of doing downlink and uplink beam management including RX and TX beam sweeping. This leads to an increased overhead and latencies which can be reduced if the uplink beam pair selection can rely on the downlink measurements without doing uplink beam sweeping. This ability is called beam correspondence and it is present if the tolerance requirement is met [3GPP20-38521]

$$\Delta EIRP = (EIRP_2 - EIRP_1) < 3dB$$

where $EIRP_2$ is the highest measured power in dBm by running uplink beam sweeping, and $EIRP_1$ is the measured power in dBm based on the uplink beam that the UE chooses to transmit in the direction of the incoming downlink signal based on beam correspondence.

The test procedure of beam correspondence is described by 3GPP in TS 38.512 [3GPP20-38521] and the RF performance criteria for beam correspondence in TS 38.101-2 [3GPP20-38101-2]. NI has performed beam *reciprocity* tests as a simplified version of beam correspondence to ensure this can be used in the beam management demonstrator as it is presented in Section 3.2.4.

3.2.1.3 RF Control Requirements

For all operation stages of a BM system – initial beam establishment, beam refinement and beam recovery – it is required to be able to switch from one beam to another. The timing requirements however depend on how BM is performed: BM can be based on SSBs and based on CSIRS/SRS. For BM based on SSBs, the RF sub-system should be able to switch analog beams for every SSB. When doing CSIRS/SRS-based BM, it is required to switch analog beams every CP-OFDM symbol which carries CSIRS/SRS. Since effects from switching transients should be minimized, the switching should happen within the cyclic prefix (CP).

The SCS of 120 kHz is going to be used for synchronization signals and data transmission. With a subcarrier spacing of 120 kHz, the SSB duration, where each SSB has four symbols, is 35.6 µs. For a symbol carrying CSIRS or SRS, the duration is 8.3 µs. The cyclic prefix in both cases is 0.6 µs long. From this it can be concluded that in an SSB-based BM system, the RF sub-system must be able to switch analog beams every 35.6 µs with the switching transient not being longer than 0.6 µs. If analog beams should be switched every CP-OFDM symbol, the RF sub-system must be able to do this every 8.9 µs with the switching transient being no longer than 0.6 µs. In the PriMO-5G project, the SSB-based BM is used.

3.2.2 Novel mmWave Transceiver Design

The components of NI mmWave transceiver system used in PriMO-5G is described extensively in Section 2 of deliverable D3.2 [D3.2]. Figure 3-1 shows the mmWave system architecture. It extends the Sub-6 GHz SDR platform towards mmWave platform, which enables the mmWave experimentation. It has three main components [GNN+21]:

- Real-Time Antenna-Array-Agnostic Control (AAC): It is capable of interfacing several mmWave antenna arrays to NI USRP. The control path is between an external application and the NI USRP FPGA. External applications can be for example a real-time 5G NR protocol stack consisting of PHY and MAC and further higher-layer functionality as well as a non-real-time streaming application that is running on a host PC. Section 3.2.3 describes the antenna array control in more details.

- NI USRP SDR: The digital baseband signal processing is implemented in the FPGA. The real-time RF control is designed to control the TX power, RX gain, and the active antenna array. In addition, it is designed to align a given beam index from the beam scheduler to the executed NR OFDM symbol on PHY layer. The NI USRP acts also as the IF module. The key performance data of NI USRP 2954-R is presented in deliverable D3.2 [D3.2].
- mmWave front-end extension: The IF transmitter/receiver represented by NI USRP is connected to up-/downconverters to shift the IF signal into the RF frequency range. In our design, the RF 5G Mixer is a 24 GHz to 28 GHz up / down converter with an integrated phase locked loop synthesizer. The IF carrier frequency can be up to 4 GHz. The mmWave antenna arrays are used to radiate the RF signals. In our mmWave transceiver design, the gNB is occupied with 8x8 mmWave antenna array while the UE is occupied with 2x8 mmWave antenna array. The key performance data of active antenna arrays for gNB and UE is presented in Section 2 of deliverable D3.2 [D3.2]. The control of the active antenna arrays is done in real-time via the dB15 connector of NI USRP using Serial Peripheral Interface (SPI) and Universal Asynchronous Receiver Transmitter (UART) protocols. The 8x8 active antenna array has a beam coverage between -60° and 60° for both azimuth and elevation angles while the 2x8 active antenna array has a beam coverage between -60° and 60° for azimuth angle and -10° and 10° for elevation angle. Both arrays have a default beam width of 15° and the supported RF interface is TDD only.

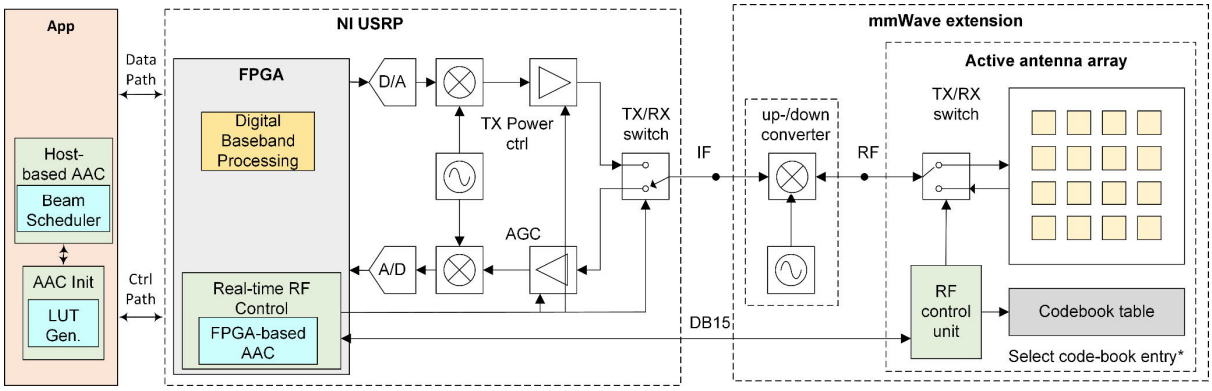

Figure 3-1 mmWave System Architecture [GNN+21]

3.2.3 Real-Time Antenna-Array-Agnostic Control

For beam steering in 5G NR, a real-time AAC with hard switching rate is required as described in Section 3.2.1.3. In addition, the AAC should be extendable to work with other mmWave antenna arrays. In the designed AAC, we define a set of messages for all expected events. Each event is mapped to the related command of the selected antenna array. The integration of another antenna array to the designed AAC is straightforward. The command mapper on the host and the beam update command generator on the FPGA need to be updated to support another antenna array. The FPGA timing parameters of SPI and UART protocols are configurable. The designed AAC has the following blocks shown in Figure 3-1:

- AAC Initialization: It sets the static and debug configurations. Those are related to the active antenna array hardware operation such as the communication source (USB or dB15), interface rate, trigger mode, … etc. The look-up-table (LUT) represented by beam indices of the selected active antenna array is generated and stored in a DRAM on the USRP FPGA. The beam indices are given to the Beam Scheduler on both the gNB and UE.
- Host-Based AAC: It is used for beam update, or antenna array re-configuration in non-real time applications. It is used also for PHY control emulation in real-time applications if the AAC is used alone.

- FPGA-based AAC: The main functionalities are triggering the beam update, reading the beam index from LUT Memory (DRAM) based on the given beam identity, generate the beam update command based on selected antenna array, and set the RF mode. It has the SPI and UART cores that are responsible for beam update command conversion to related interface.

The designed AAC supports the following operation modes as it is shown in Figure 3-2:

- Host-based Mode: Useful for antenna array commands test and antenna array characterization. It is used for non-real time applications.
- FPGA-based Mode: It has three submodes:
  - Continuous Beam Sweeping: Useful for beam update rate and antenna array stability test.
  - Manual Beam Selection: Useful for non-real time streaming applications or real-time applications during the development phase.
  - External App Beam Selection: Useful for real-time applications such as 5G NR protocol stack (gNB and UE), for example to be part of beam management.

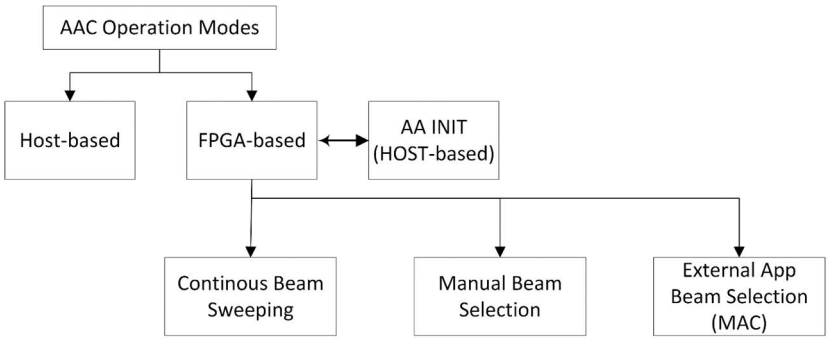

Figure 3-2 AAC Operation Modes

It is worth mentioning that the AAC needs only a few cycles at 200 MHz clock rate on FPGA to create the beam update command based on a given beam identity. The AAC latency in FPGA between getting the beam identity until sending the first bit to the active antenna array interface is 20 ns. The 8x8 active antenna array supports both SPI and UART protocols. The UART protocol is used for initial antenna array configuration at a baudrate of 115.2K while the SPI is used for beam update at 10 MHz rate. The SPI beam command has 24 bits and can be transferred to active antenna array via a dB15 cable. The transfer latency is 2.5 us (24 cycles times 100 ns + 100 ns for SPI clock rising edge and SPI chip select rising edge). The 2x8 active antenna array supports only UART at a baudrate of 921.6 K. The beam update command has 7 bytes. The latency of beam command transfer is 75.95 us (each UART byte has extra two bits for start and stop). The active antenna arrays have extra latency for beam command processing. Their transient time is less than 100 ns for 8x8 and 500 ns for 2x8 active antenna array. As a result, the active antenna arrays that support SPI will allow switching per a single OFDM symbol while the active antenna arrays that supports only UART will allow switching per two Slots.

3.2.4 System-Level Beam Reciprocity Test

Together with the real-time RF control, the USRP-based mmWave prototyping architecture is used to investigate if beam reciprocity on a system-level is applicable. The downlink beam sweeping finds a specific pair of downlink TX beam on the gNB and downlink RX beam on the UE. If beam reciprocity is given, the azimuth and elevation angle from the downlink TX beam can be applied to the uplink RX beam and vice versa while maintaining a comparable performance in terms of EIRP and EVM. With this the uplink beam management can be simplified a lot as it can use the results from the downlink beam management.

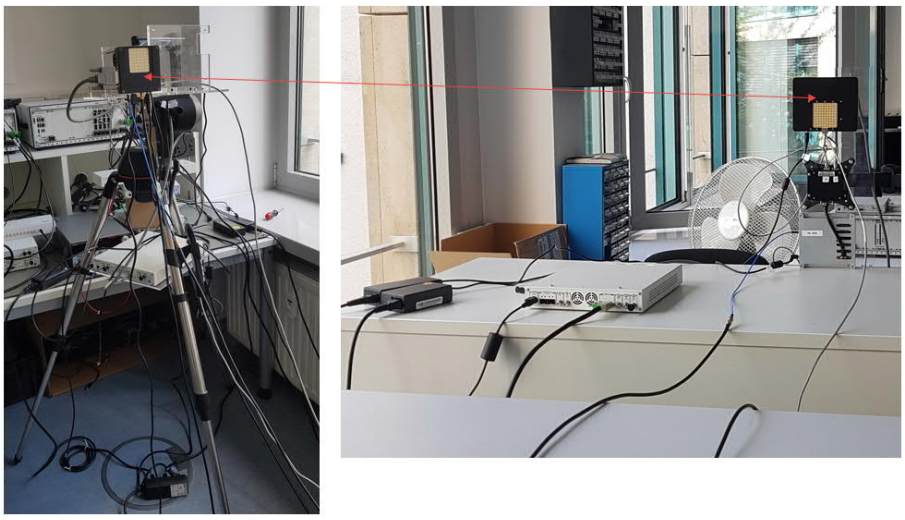

Figure 3-3 Beam Reciprocity test setup with 4.37 m distance at 26.45 GHz; left: UE, right: gNB

For the PriMO-5G mmWave demonstrator, the beam reciprocity investigations have been performed in an indoor office environment with the setup as shown in Figure 3-3:

- gNB active antenna array with a fixed orientation,
- UE active antenna array on top of a telescope movement unit.

Both antenna arrays were positioned at the same vertical level. The measurements were performed at an RF frequency of 26.45 GHz using 5G NR standard compliant uplink and downlink waveforms that were generated using the NI RFmx NR Waveform Creator [NI_RFmx_Waveform_creator] with the following settings: TDD, 64-QAM, 120 kHz SCS, 100 MHz bandwidth, and PTRS enabled. For analyzing the received signal, the NI RFmx NR [NI_RFmx_NR_Lib] library was used.

With these prerequisites the actual test procedure was performed. The telescope movement unit rotates the UE antenna array in the azimuth plane while keeping the elevation angle constant. The azimuth rotation range is between -60° and +60° with a resolution of 12°. For each azimuth angle, the following steps were performed in the downlink:

- The downlink waveform is transmitted by the gNB USRP repeatedly.
- Both on the gNB side (8x8 antenna array) and the UE side (2x8 antenna array) beam steering is executed using the antenna array control.
- For each beam pair (DL and UL) EIRP and EVM are measured on the UE USRP.

In the uplink, the uplink waveform is transmitted by the UE USRP repeatedly and two cases are considered:

1. Uplink beam sweeping: The same procedures as in the downlink beam sweeping are performed, beam steering is executed on both sides and for each beam pair, EIRP and EVM are measured on the gNB USRP.
2. Uplink beam reciprocity: The EIRP and EVM measurements on the gNB side are performed using the UL beam pair that is equivalent with the DL beam pair that led to the best results in the downlink.

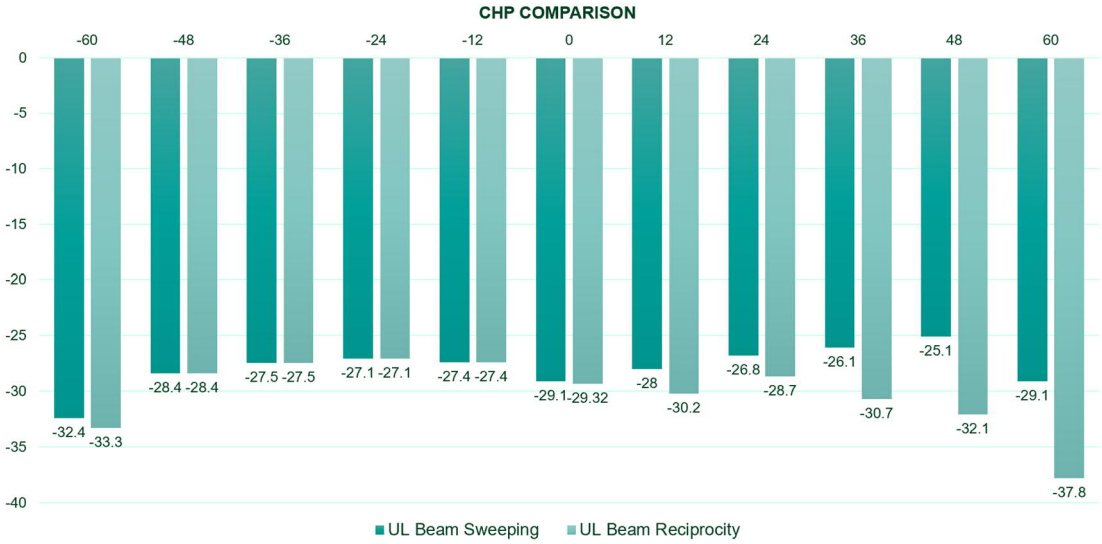

Figure 3-4 Channel Power (CHP) comparison at gNB using UL beam sweeping and UL beam reciprocity

Figure 3-4 shows the difference between the channel power measured on the best uplink beam resulting from uplink beam sweeping and the channel power measured on the uplink beam resulting from beam reciprocity. It can be observed that over a wide range of azimuth angles the results are identical whereas they differ in the boundaries. The overall differences are in range of the beam correspondence condition: $\Delta EIRP = (EIRP_2 - EIRP_1) < 3dB$. The beam indices in the downlink (DL TX and DL RX) that lead to the highest power are the same beam indices in the uplink (UL TX and UL RX) that lead to the highest power, again with the exception of the beams at the boundary.

With the results of the measurements, we can conclude that the setup NI uses for PriMO-5G has beam reciprocity, which means the UL beam management will rely on DL measurements.

3.2.5 mmWave Extensions and Antenna Array Control Integration

The PriMO-5G transceiver design from NI has been enhanced to support FR2. The mmWave extensions are presented in the following sub-sections.

3.2.5.1 Antenna Array Control Integration

The antenna array control is integrated into the MAC-Stub and PHY of gNB and UE as it is shown in Figure 3-5. Both can do beam sweeping and select an active beam for data transmission. In addition, they are responsible for changing the RF mode of the antenna array based on the frame structure and aligning the execution of beam update with the OFDM symbol start by calibrating the baseband and IF latencies.

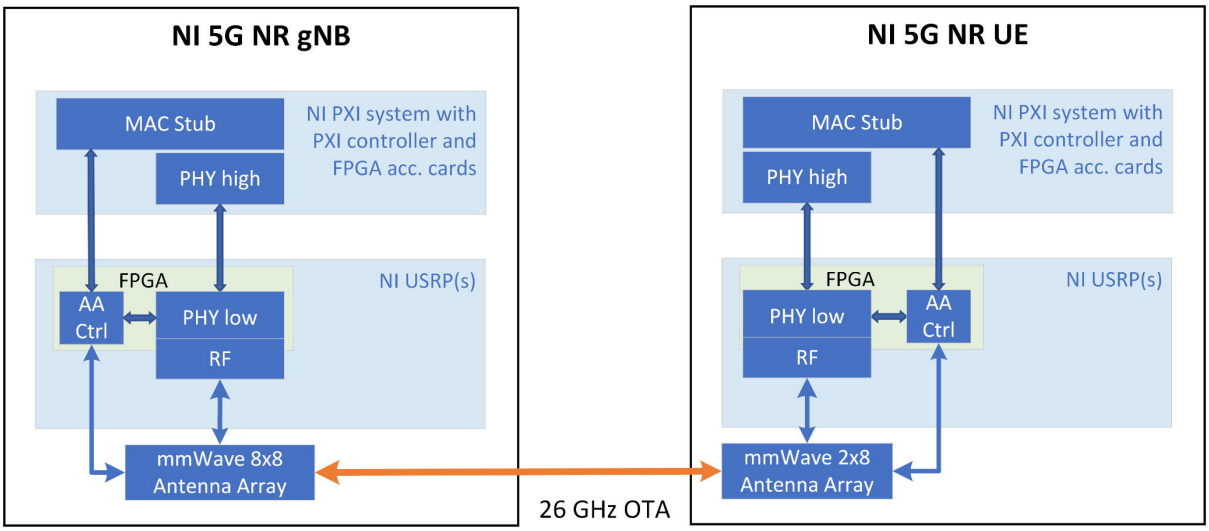

Figure 3-5 mmWave extensions and Antenna Array Control Integration to 5G NR gNB and UE (gNB MAC-Stub to UE MAC-Stub)

3.2.5.2 PHY Extensions

The PHY numerology is extended to have the SCS of 120 KHz for data and synchronization signals. The PHY baseband mmWave extensions are implemented including time and frequency resource allocation, rate matching, … etc. The gNB is transmitting the SSBs with a periodicity of half frames. For initial cell selection, the UE may assume that half frames with SSBs occur with a periodicity of 2 frames as in Section 4.1 of TS 38.213 [3GPP20-38213]. In our case, the Case-D of SCS 120 kHz is used. The first symbols of the candidate SSBs have the following indexes $\{4, 8, 16, 20\} + 28 \cdot n$, where n = 0, 1, 2, 3, 5, 6, 7, 8, 10, 11, 12, 13, 15, 16, 17, 18 for the carrier frequencies within FR2 as in Section 4.1 of TS 38.213 [3GPP20-38213]. The 64 SSBs are transmitted in a burst from the gNB. The UE scans the RX frame and identifies the best SSB to be used for Sync. The PRACH occasion is configured to have a single SSB per each RACH occasion [3GPP20-38213]. Since the gNB and UE are occupied with a MAC-Stub and not the full stack, a simplified Random Access Procedure and random access preamble transmission is implemented. The RSRP of SSS within SSB is measured: the so-called SS-RSRP. The ability of measuring the SS-RSRPs in a burst is implemented on the UE. The measured SS-RSRPs are reported to the UE beam scheduler on UE MAC-Stub for further processing. If the UE is in a connected mode, the best N SS-RSRPs are reported periodically via UCI on PUSCH; the report is created as in Table 6.3.1.1.2-8 of 3GPP TS 38.212 [3GPP20-38212]. The support of AGC and TX power control is implemented.

3.2.5.3 MAC-Stub Beam Management Extensions

The designed MAC-Stubs are able to manage the simplified Random Access Procedure. The beam schedulers on both side of the communication link are created to support the different beam management stages (initial beam establishment, beam refinement, and beam failure recovery). It is worth mentioning that the antenna array LUT can have a large number of beam IDs. For example, the 8x8 antenna array on gNB has 121 Beam IDs, where only 64 Beam IDs should be selected. An optimized algorithm that uses probabilistic arguments was implemented to select the useful number of beam IDs in an efficient way.

3.2.6 mmWave Beam Management Prototyping for 5G NR

In the mmWave beam management demonstrator, we want to show a stationary mmWave base station and a mobile UE on a cart that perform initial beam establishment, then transmit UL Data and possibly some control information or similar in the downlink. When the UE cart is moved, the data link should

remain stable by doing a continuous beam adjustment. Beam adjustment is sometimes not able to cope with rapid-changing environment conditions that degrade the established beam pairs. As a result, there is a need for beam recovery. The beam management can also be classified to two types based on the communication link direction:

- Downlink beam managment: The gNB and UE should identify and maintain the best DL TX and DL RX beam pair shown in Figure 3-6.
- Uplink am managment: The gNB and UE should identify and maintain the best UL TX and UL RX beam pair shown in Figure 3-6. In our setup, the beam reciprocity exists, and the UL beam management can rely on DL measurements.

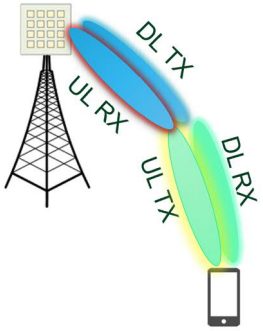

Figure 3-6 gNB and UE beams to be identified

3.2.6.1 Initial Beam Establishment

The procedure of initial beam establishment that has been implemented based on 3GPP specifications is shown in Figure 3-7, which can be summarized in the following steps:

- gNB DL TX Beam Sweeping: The gNB is transmitting the SSBs pattern with a periodicity of the half frames. Each SSB is transmitted via different beam ID.
- UE DL RX Beam Sweeping: Here, we have two levels of scanning to identify the best DL TX beam from the gNB and the best DL RX beam on the UE. To find the best DL TX beam from the gNB, the UE scans the received frame and identifies the best SSB to be used for sync. As soon as the UE is in Sync with the gNB, it measures the RSRPs of all SSBs within the half frame and report them to the UE MAC-Stub Beam Scheduler, which is still in initial beam establishment stage. The UE MAC beam scheduler will store those measurements for a given UE RX beam ID. Every two frames, the UE switches to another RX beam ID, measures the RSRPs of all SSBs and then reports the RSRP measurements of all SSBs to UE Beam Scheduler. If the UE is done with RX beam sweeping, it will set the UE DL RX beam and UE UL TX beam to the beam ID that leads to the maximum SS-RSRP. Then, PRACH preamble is sent during RACH occasion that belongs to the SSB with SS-RSRP larger than a given rsrp-ThresholdSSB.
- gNB DL TX and UL RX Beam Identification: gNB detects PRACH preamble transmission and can conclude from time and frequency resources to which SSB this PRACH preamble transmission belonged to and hence, which DL TX beam was used for this SSB. The same beam ID is going to be used as well for UL RX beam due to the presence of beam reciprocity.

Both gNB and UE beam schedulers will switch from initial beam establishment to beam adjustment stage.

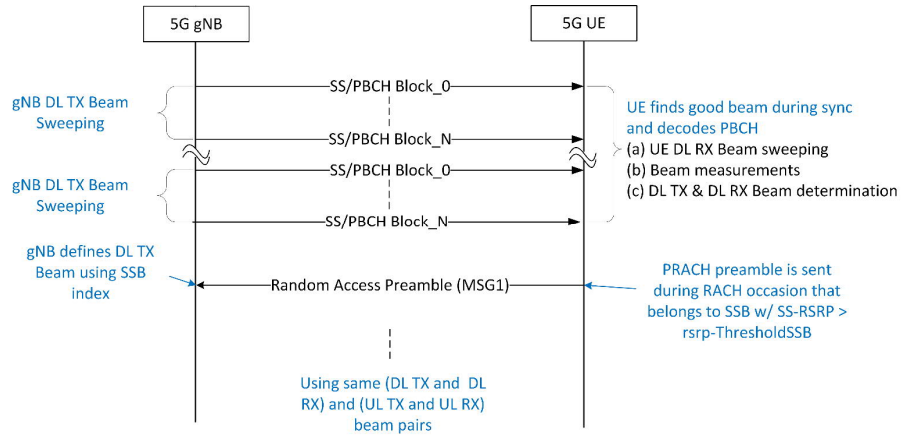

Figure 3-7 Initial Beam Establishment

3.2.6.2 Beam Adjustment

Beam adjustment is used to adjust initial DL and UL beam pairs if needed. The SSB-based beam selection is used also for beam adjustment. The UE reports the SS-RSRP measurements in a periodic manner via UCI on PUSCH to gNB. The UCI of SS-RSRP report is built up like Table 3-1, Table 6.3.1.1.2-8 of TS 38.212 [3GPP20-38212], where SSBRI is the SSB index for which we want to report the RSRP value, the RSRP is an index between 0 and 127 as defined in Table 10.1.6.1-1 of [3GPP20-38133], and differential RSRP is an index for difference from first RSRP as defined in Table 10.1.6.1-2 of [3GPP20-38133] and can cover values between 0 and -30 dB.

Table 3-1 Mapping order of CSI fields of one SS-RSRP reporting [3GPP20-38212]

CSI Report Number	CSI Fields
CSI Report number n	SSBRI Index number 1
	SSBRI Index number 2
	SSBRI Index number 3
	SSBRI Index number 4
	RSRP number 1
	Differential RSRP number 2
	Differential RSRP number 3
	Differential RSRP number 4

On the gNB, the SS-RSRP measurement report is extracted from UCI payload and provided to gNB Beam Scheduler. The gNB Beam Scheduler has a register with a configurable depth, where the measurements history is stored. After receiving a new SS-RSRP measurement report, the history of measurement will be updated with the current measurement, and the Beam Scheduler processes the measurements to find the best SSB index. If the SSB index with the best average RSRP is not equal to the active SSB Index, which points to the Beam ID of data transmission, the gNB beam scheduler will update the beam ID of data transmission.

3.2.6.3 Beam Failure recovery

The beam failure recovery (BFR) is embedded into a simplified radio link monitoring and maintenance. The beam failure is detected if a hypothetical BLER is above a threshold for a number of consecutive events. If this happens, the initial beam establishment is started simply again. The beam failure recovery request is presented by transmission of PRACH preamble considering an UE-specific configuration.

3.2.7 Basic System Performance Measurements

The gNB and UE are running in a lab environment as it is shown in Figure 3-8. The gNB mmWave antenna array has a fixed location while the UE mmWave antenna array is installed on top of a telescope movement unit. The system has been parametrized as follows: IF = 3,34938 GHz, RF = 28,03296 GHz (SSB center ARFCN = 2079163, and DL and UL pointA ARFCN = 2078923) and a component carrier bandwidth = 100 MHz. The 5GNR 3GPP Rel-15 compliant waveform has a subcarrier spacing = 120 kHz, 64QAM as modulation scheme and the usage of PTRS is not enabled. The used modulation and coding scheme is number 28 based on Table 5.1.3.1-1 of TS 38.214 [3GPP20-38214]. The choice for *ssb-PositionsInBurst* is Long (64 SSBs). The PRACH configuration index is 10, and the *ssb-perRACH-Occasion* is 1. The *dmrs-TypeA-Position* is 2 and the number of layers is 1. All physical resource blocks (PRB) of 66 are used and the number of scheduled OFDM symbols is 11. The DL data is transmitted on only a single slot; slot number 40. The throughput is 4.184 Mbit/s. If the TDD slot type [DDDDDDDSUU] is used and all DL slots in the second half of the frame are occupied with Data using MCS number 28, the PHY throughput is 117.15 Mbit/s. Figure 3-9 shows the UE GUI. A measured averaged EVM of approximately -26 dB would allow the usage of 64QAM as modulation scheme while spectrum emission mask is kept.

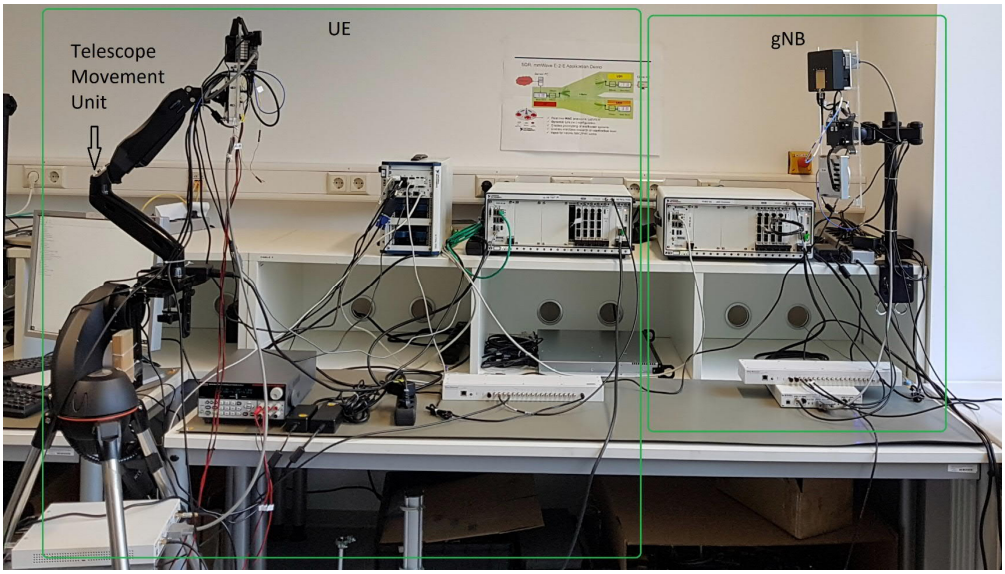

Figure 3-8 gNB and UE Setups

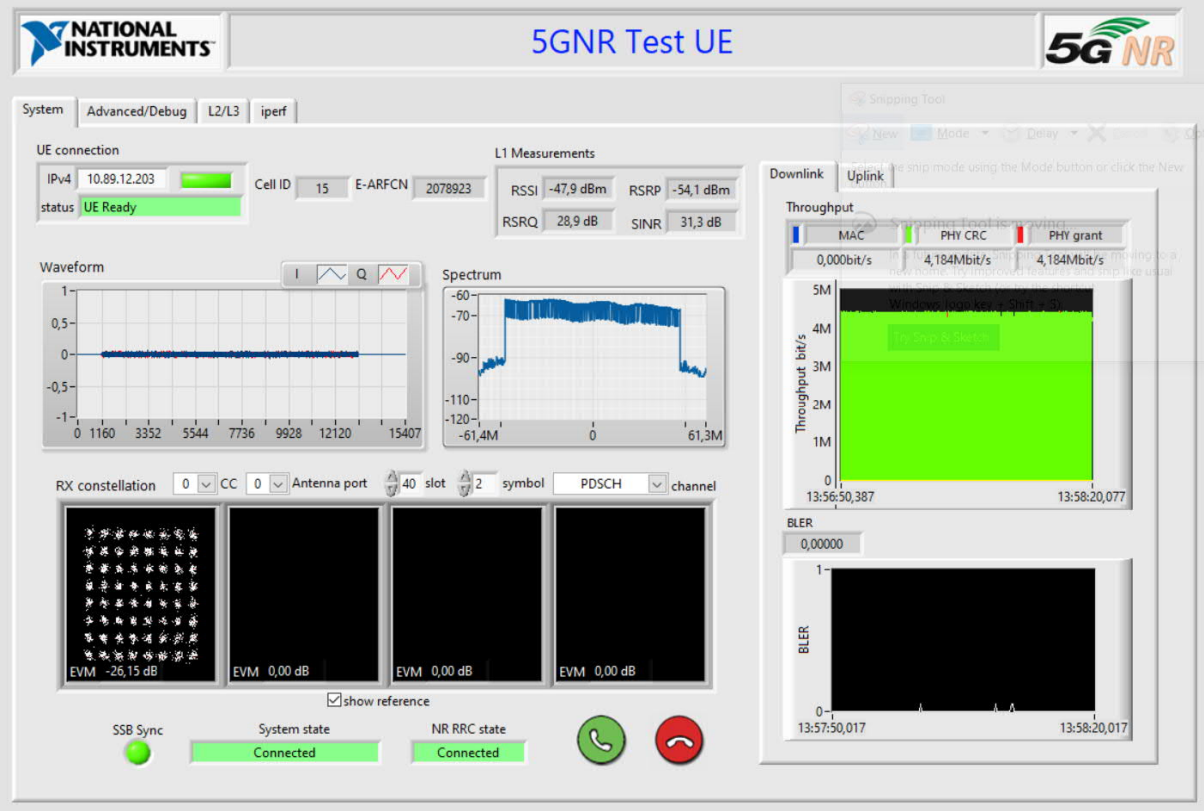

Figure 3-9 UE GUI

3.3 MMSE-Interference Canceling Receiver for QAM-FBMC Systems

When considering the PriMO-5G use case scenarios, an immersive video services utilizing UAVs, getting robustness for the mobility environment is an important technology. This section presents a QAM-FBMC waveforms to address the shortcomings of CP-OFDM, which are sensitive to frequency offset and susceptible to synchronization failure.

In this section, we focus on the MMSE-Interference canceling receiver. Quadrature amplitude modulation-filter-bank multi-carrier (QAM-FBMC) technology, which utilizes a non-orthogonal pulse-shaping filter, has high spectral confinement characteristics and spectral efficiency, and it is considered as a candidate waveform to replace cyclic prefix-orthogonal frequency division multiplexing (CP-OFDM). However, the QAM-FBMC system suffers from performance degradation due to the non-orthogonal filter no matter how well the prototype filter is designed. In this section, we propose the interference-canceling algorithm for QAM-FBMC with an MMSE receive filter. The proposed algorithm effectively mitigates the performance degradation caused by the non-orthogonal filters of QAM-FBMC systems, and it closely achieves the performance of CP-OFDM system in moderate SNR region. Also, the proposed algorithm performs the symbol-wise detection, which allows practical implementation without system delay.

To Avoid the intrinsic interference problem of offset-quadrature amplitude modulation-filter-bank multicarrier (OQAM-FBMC) technology, quadrature amplitude modulation-filter-bank multi-carrier

(QAM-FBMC) systems based on non-orthogonal prototype filters have been studied [YKK+15], [HKK+16], [NSR17], [LCL+18], [ZL14]. The prototype filters of QAM-FBMC systems can be designed using global optimization with the relaxed generalized Nyquist criterion, a fast fall-off rate condition, and time-frequency domain confinement constraints [KHP17], [HP19]. By this filter design, at the cost of acceptable performance loss from the relaxed orthogonality condition, the QAM-FBMC system can dramatically reduce the intrinsic interference problem in a complex channel.

Unlike orthogonal waveforms, such as cyclic prefixorthogonal frequency-division multiplexing (CP-OFDM) and OQAM-FBMC, it is impossible to achieve perfect orthogonality in a QAM-FBMC system no matter how well its prototype filters are designed [BHW98]. Since the non-orthogonality of QAM-FBMC systems causes inter-symbol and inter-subcarrier interference, designing a receiver that can minimize the degradation of the bit error rate (BER) is challenging. Previously, researchers proposed a decision feedback equalizer (DFE)-based interference-mitigating receiver for QAM-FBMC systems [HKK+16]. They formulated the mathematical model of the equivalent system transfer function of a QAM-FBMC system in z-domain, decomposed the transfer function by spectral fac-torization for matrix polynomials, and applied the decomposed components to the DFE structure to mitigate the residual self-interference. Although the algorithm introduced in [HKK+16] was able to improve the BER, the implementation is not practical due to the problems of high decomposition complexity for multi-tap matrix polynomials and large system delays.

In another paper [HKP20], a QAM-FBMC receiver was proposed, which uses a minimum mean squared error (MMSE) filter, replacing the matched filter used in all existing QAM-FBMC receivers. For QAM-FBMC with the non-orthogonal property in which interference exists, the MMSE filter can maximize the self-signal to interference plus noise ratio (self-SINR), which reduces the BER degradation [HKP20]. Also, they designed prototype filters that would provide the best performance considering the use of MMSE filters. The proposed filters showed higher self-SINR values than the conventional filters for given design purposes, and thus showed better BER.

By utilizing the QAM-FBMC system configuration using the MMSE filter as described above, the BER can be improved further by designing an interference-canceling receiver struc-ture. To this end, we propose a nonlinear receiver, which cancels out the residual interference of the received signal after MMSE filtering, without a DFE structure requiring complicated spectral factorization for multi-tap matrix polyno-mials [HKK+16]. Our design is motivated by successive interference cancellation (SIC) and parallel interference cancellation (PIC) concepts in multiple-input and multiple-output (MIMO) com-munication systems with an MMSE receiver [FM00], [ZCW05], [GRS+00], [LZL+08].

For the system model, we use the stacked matrix representation of the QAM-FBMC system model, which is introduced in [HKP20]. Then the relationship between the transmitted data symbols involved by the overlap-and-sum structure and the received data symbol can be expressed as a simple linear model. We denote M as the number of subcarriers, L as the overlap-ping factor for frequency-domain filtering, and N = LM as the number of upsampled frequency points. Figure 3-10 illustrates the QAM-FBMC transceiver structure in stacked matrix representation.

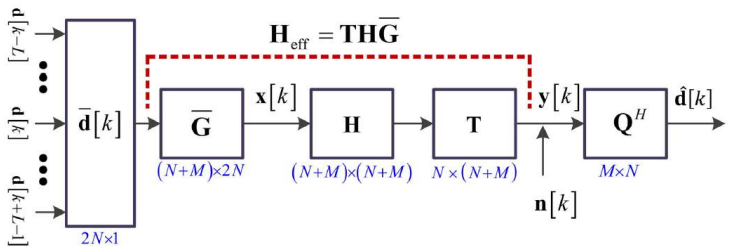

Figure 3-10 The stacked matrix representation on QAM-FBMC system with a linear receiver

First, we express the transmitted data symbols, which are involved in the k-th symbol interval by the overlap-and-sum structure, in the stacked representation as follows,

$$\overline{\mathbf{d}}[k] = [\mathbf{d}[k-L]^T, \cdots, \mathbf{d}[k+L-1]^T]^T \tag{3.1}$$

where $\mathbf{d}[k]$ is the k-th data vector containing QAM data symbols $d_m[k]$ with the subcarrier index m. From (3.1), the k-th transmitted signal $\overline{\mathbf{x}}[k]$ in the stacked representation can be expressed using the stacked pulse-shaping filter $\overline{\mathbf{G}}$ as

$$\overline{\mathbf{x}}[k] = \overline{\mathbf{G}}\overline{\boldsymbol{d}}[k] \tag{3.2}$$

where $\overline{\mathbf{G}}$ is a matrix of size $(M+N) \times 2N$ consisting of time-domain pulse shaping filter coefficients for the corresponding data symbol element of $\overline{\mathbf{d}}[k]$. A formal definition of the pulse shaping filter coefficients can be found in [HKP20].

Second, we define the time-domain channel matrix for the stacked system model with L_c channel taps as follows,

$$[\mathbf{H}]_{(:,m)} = \text{cirshift}\left\{\left[h_0 \dots h_{L_c-1}\mathbf{0}_{N+M-L_c}\right]^T, m-1\right\}, \tag{3.3}$$

where $\text{circshift}(\mathbf{a}, m)$ operation is defined as a circularly shifted vector of $\mathbf{a}$ by m elements. Then the k-th received signal vector $\mathbf{y}[k]$ of size $N \times 1$ can be expressed as

$$\mathbf{y}[k] = \mathbf{T}\mathbf{H}\overline{\mathbf{G}\mathbf{d}}[k] + \mathbf{n}[k] \tag{3.4}$$

where $\mathbf{T} = [\mathbf{0}_{N\times M}\mathbf{I}_N]$ is a time-domain slice matrix to extract the samples in the k-th received window. The additive white Gaussian noise (AWGN) vector $\mathbf{n}[k]$ follows the complex Gaussian distribution as $\mathbf{n}[k] \sim \mathcal{CN}(0, \sigma_n^2\mathbf{I}_N)$. By treating the linear receiver process as a filtering process with the receive filter matrix $\mathbf{Q} \in \mathbb{C}^{M\times N}$, the k-th detected data symbol can be represented as follows,

$$\overline{\mathbf{d}}[k] = \mathbf{Q}^H\mathbf{H}_{\text{eff}}\overline{\mathbf{d}}[k] + \mathbf{Q}^H\mathbf{n}[k] \tag{3.5}$$

Where$\mathbf{H}_{\text{eff}} \triangleq \mathbf{T}\mathbf{H}\overline{\mathbf{G}}$. Note that $\mathbf{Q}$ can be designed as the conventional matched filter or MMSE filter [YKK+15], [HKP20].

3.3.1 MMSE Interference cancellation receiver

To improve the detection performance, a nonlinear receiver can be designed according to the conventional approaches, such as spectral factorization-based DFE [HKK+16] and MMSE-SIC [FM00], [ZCW05], [GRS+00], [LZL+08]. However, the DFE-based receiver in [HKK+16] can-not be directly used in realistic fading channel due to the non-symmetricity of equivalent system transfer function, and the MMSE-SIC receiver cannot exploit the effect of IC due to the characteristic of interference signal in QAM-FBMC system.

To design an effective IC receiver, we propose the MMSE filter-based IC (MMSE-IC) algorithm for QAM-FBMC system using the stacked matrix representation in (3.5), which efficiently removes the interference components of the received signal in a simple nonlinear fashion. Since the k-th desired symbol after linear MMSE filtering is still overlapped with interference components, which have smaller power than the desired one, we combine the MMSE filter update-based SIC technique with an additional process using the concept of PIC technique.

3.3.2 MMSE Filter design for the Adjacent Symbol Components

In order to cancel out the interference at the k-th symbol time, we exploit the adjacent symbol information with the index $(k+l)$ for$l \neq 0$, which can be detected by using MMSE filters designed for each l. The MMSE filter for detecting the $(k+l)$-th transmitted symbol $\mathbf{d}[k+l]$ as $\tilde{\mathbf{d}}$ can be found by solving the following MMSE problem.

$$\begin{aligned}\mathbf{Q}[k+l] &= \underset{\mathbf{Q}}{\operatorname{argmin}} \left[\mathbb{E}\left\|\tilde{\mathbf{d}}[k] - \mathbf{d}[k+l]\right\|_2^2\right] \\ &= \underset{\mathbf{Q}}{\operatorname{argmin}} \left[\mathbb{E}\left\|\left(\mathbf{Q}^H\mathbf{H}_{\text{eff}}\bar{\mathbf{d}}[k] + \mathbf{Q}^H\mathbf{n}\right) - \mathbf{S}^{(l)}\bar{\mathbf{d}}[k]\right\|_2^2\right]\end{aligned} \tag{3.6}$$

for $l = -L, \dots, L-1$, where $\mathbf{d}[k+l] = \mathbf{S}^{(l)}\bar{\mathbf{d}}[k]$. The sampling matrix $\mathbf{S}^{(l)}$ is to extract the $(k+l)$-th symbol from the stacked data vector $\bar{\mathbf{d}}[k]$. Following the procedure in [HKP20], we can derive the MMSE receive filter to detect the l-th relative adjacent data symbol as

$$\mathbf{Q}[l] = \left(\mathbf{H}_{\text{eff}}\mathbf{H}_{\text{eff}}^H + \frac{\sigma_n^2}{\sigma_d^2}\mathbf{I}\right)^{-1}\mathbf{H}_{\text{eff}}\mathbf{S}^{(l)H} \tag{3.7}$$

where the filter is shown to be independent of k, thereby we drop the index k from the expression. If the l'-th adjacent symbol components for $l' = a, \dots, b$ are canceled from the received signal, then $\mathbf{Q}[l]$ in (3.7) should be modified by changing the effective channel matrix $\mathbf{H}_{\text{eff}}$. In this case, the MMSE receive filter can be rewritten in consideration of the removed component as follows,

$$\mathbf{Q}[l] = \mathbf{Q}^{(a:b)}\mathbf{S}^{(l)H} \tag{3.8}$$

with

$$\mathbf{Q}^{(a:b)} \triangleq \left(\mathbf{H}_{\text{eff}}^{(a:b)}\mathbf{H}_{\text{eff}}^{(a:b)H} + \frac{\sigma_n^2}{\sigma_d^2}\mathbf{I}\right)^{-1}\mathbf{H}_{\text{eff}}^{(a:b)} \tag{3.9}$$

Where $\mathbf{H}_{\text{eff}}^{(a:b)}$ is defined as the modified version of Heff by nulling the columns corresponding to the $(l' = a, \dots b)$-th adjacent symbols.

3.3.3 Proposed MMSE-IC Procedures

Although the MMSE filter in (3.7) minimizes the MSE in a linear system, we can improve the performance further by exploiting other adjacent symbol information, which cannot be fully exploited in the linear system. To this end, the unknown adjacent symbols are sequentially detected along with l using (3.8). Then the detected adjacent symbol infor-mation can be canceled out from the received signal in a nonlinear fashion according to the conventional SIC approach. However, the direct use of the SIC technique, which should be performed in decreasing order of signal power, is not applicable to our system because the desired symbol after MMSE filtering has always the highest power than other interference components. To overcome this, we also adopt the PIC technique after the SIC procedure. The proposed MMSE-IC algorithm is summarized in Algorithm 1, where the definitions of the simplified notations are given as follows,

- $\mathbf{y} \triangleq \mathbf{y}[k]$,
- $\tilde{\mathbf{d}}^{(l)}$: The detected symbol corresponding to $\mathbf{d}[k+l]$,
- $Q(\cdot)$: QAM-demodulation and symbol regeneration,
- $[\mathbf{H}_{\text{eff}}]_{(l)}$: the extracted matrix with the columns for the l-th adjacent symbol from the effective channel matrix $\mathbf{H}_{\text{eff}}$, which is the matrix with $(N+lM)(N+(l+1)M-1)$-th columns of the $\mathbf{H}_{\text{eff}}$.

Algorithm 1 MMSE-IC Procedure

Require: $\mathbf{y}$, $\tilde{\mathbf{d}}^{(l)}$ for $l = -L, \ldots, -1$.
Output: $\tilde{\mathbf{d}}^{(0)}$

1: Perform pre-cancellation of the preceding symbols.
$$\mathbf{y}^{(0)} = \mathbf{y} - \sum_{l=-L}^{-1} [\mathbf{H}_{\text{eff}}]_{(l)} \tilde{\mathbf{d}}^{(l)}$$
2: **for** $l \leftarrow 0$ to $(L-1)$ **do**
3: Get l-th adjacent symbol by MMSE receive filter from the received signal after cancelling the previous symbols.
$$\mathbf{u}^{(l)} = \mathbf{S}^{(l)} \mathbf{Q}^{(-L:l)H} \mathbf{y}^{(l)}$$
4: Perform QAM-demodulation and symbol regeneration
$$\hat{\mathbf{u}}^{(l)} = Q\left(\mathbf{u}^{(l)}\right)$$
5: Successively cancel the l-th symbol component from the received signal.
$$\mathbf{y}^{(l+1)} = \mathbf{y}^{(l)} - [\mathbf{H}_{\text{eff}}]_{(l)} \hat{\mathbf{u}}^{(l)}$$
6: **end for**
7: Constitute the desired signal without adjacent symbol components.
$$\tilde{\mathbf{y}}^{(0)} = \mathbf{y}^{(L)} + [\mathbf{H}_{\text{eff}}]_{(0)} \hat{\mathbf{u}}^{(0)}$$
8: Detect $l = 0$-th symbol again
$$\tilde{\mathbf{d}}^{(0)} = \mathbf{S}^{(0)} \mathbf{Q}^{(l \neq 0)H} \tilde{\mathbf{y}}^{(0)}$$

In Algorithm 1, the information of the previously detected symbols are first canceled out in Step 1, which is also presented in Figure 3-11(a). From Step 2 to Step 6, SIC is performed in decreasing order of the power of the overlapped symbols of QAM-FBMC. The SIC procedure is illustrated in Figure 3-11(b). However, when performing only the general SIC process, the desired symbol with l = 0 has the largest power compared to all other interference symbols. As a result, when the SIC process is performed in decreasing order of power, the first desired symbol cannot benefit from the SIC procedure. For this reason, we use the concept of PIC technique in Step 7 such that the desired symbol component is obtained by excluding the adjacent interference symbol components from the received signal. This is illustrated in Figure 3-11(c).

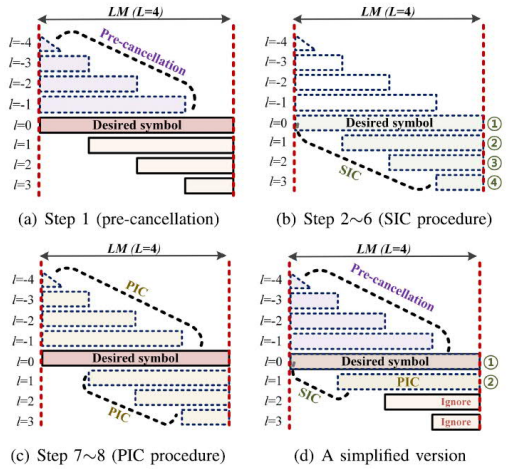

(a) Step 1 (pre-cancellation) (b) Step 2∼6 (SIC procedure)

(c) Step 7∼8 (PIC procedure) (d) A simplified version

Figure 3-11 The detailed processes of the proposed MMSE-IC algorithm for QAM-FBMC system

3.3.4 Complexity of MMSE-IC Algorithm

Simplified Version of Algorithm 1: If necessary, additional gain can be taken into account by using inter-

subcarrier IC. However, this method is typically too complex and ineffec-tive because the number of subcarriers is too large and there is little power difference between each subcarrier component. Therefore, in the proposed algorithm, the block operation is performed without IC in each subcarrier in a single symbol block, thereby greatly reducing the hardware complexity and eliminating system delay. In addition, the interference components of QAM-FBMC system with a well-designed pulse shaping filter do not have large powers except for the adjacent symbols of l = 1, −1. In this case, even if the SIC is performed only for l = 1, −1 , the residual interference are negligible. To be specific, the SIC processes from Step 2 to Step 6 are performed only for l = 0and l = 1-th symbols. The simplified version of Algorithm 1, which is used for simulations, is illustrated in Figure 3-11(d).

Computational Complexity of the Proposed Algorithm: The proposed algorithm basically repeats the linear MMSE filtering and IC procedure in the loop. Then the computational complexity of the Algorithm 1 is approximately L + 1 times higher than that of the linear MMSE receiver. In the case of the simplified version described above, the complexity is only approximately 3 times higher than that of the linear MMSE receiver. It is remarkable that the complexity of the proposed algorithm with a practical value of L, e.g., $L \leq 4$, has the same order of $\mathcal{O}(N^3)$ with the linear MMSE receiver. The specific comparison of complexity is presented in Table 3-2 in terms of the number of complex multiplications, which dominate the addition operations [SMJ+19]. Meanwhile, it is impossible to compare with the complexity of nonlinear baseline scheme because a specific QAM-FBMC receiver structure, which can be used in fading channel, has not been studied yet.

Table 3-2 Comparison of computational complexity

Receiver type	The number of complex multiplications
Linear MMSE	$\frac{13}{3}N^3 + \left(1+\frac{1}{L}\right)N^2 - \frac{1}{3}N$
MMSE-IC (Algorithm 1)	$\frac{13}{3}(L+1)\,N^3 + \left(L+4+\frac{1}{L}\right)N^2 - \frac{L+1}{3}N$
MMSE-IC (Simplified)	$13N^3 + \left(4+\frac{5}{L}\right)N^2 - N$
DFE-based approach	No specific scheme in fading channel

Table 3-3 The prototype filters for simulation

	[YKK+15]	[KHP17]	[HKP20]	
Type	2	C	G30	G50
Target receive filter	Matched		MMSE	
Target SNR [dB]	∞	∞	30	50
K(Number of taps in frequency)	15	15	15	15
$\Upsilon\,(0, \mathbf{q})$ [dB]	19.2	17.4	24.9	25.4
Fall-off rate	$\lvert\omega\rvert^{-4}$	$\lvert\omega\rvert^{-5}$	$\lvert\omega\rvert^{-5}$	$\lvert\omega\rvert^{-5}$
σ_t	0.197	0.083	0.078	0.075
Coefficient	Complex	Real	Real	Real

Table 3-4 Simulation parameters

Parameter	Value
M	64
L	4
Modulation	QPSK, 16-QAM, and 64-QAM
Channel	AWGN, EPA, and EVA [HLD+12]
Receive filter	Matched filter and MMSE filter
IC algorithm	DFE [HKK+16] and MMSE-IC (Algorthm1)

To compare the different QAM-FBMC schemes, we bring the several prototype filter candidates from previous researches in Table 3-3, where the definitions of the notations can be found in [HKP20]. Each prototype filter is designed by assuming a target SNR at the receiver. Type G30 and G50 filters in [HKP20] are designed to achieve the highest self-SINR at SNR = 30 dB and SNR = 50 dB, respectively. The parameters used in our simulations are listed in Table 3-4.

In Figure 3-12, we compare the BER between the existing DFE-based algorithm [HKK+16] and the proposed MMSE-IC algo-rithm in AWGN channel. The BERs of MMSE-IC are plotted using the simplified version of Algorithm 1 because they are almost the same with that of Algorithm 1. We observe that the BER of the proposed MMSE-IC algorithm is comparable to that of the DFE-based algorithm when using Type 2 filter, while approaching to that of the OFDM system which does not suffer from interference.

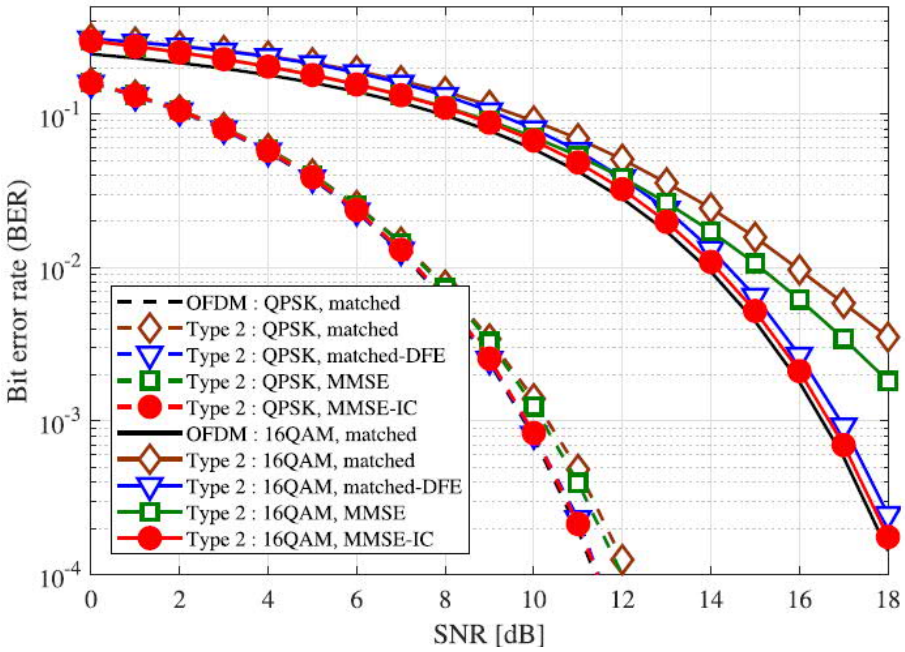

Figure 3-12 The BER comparisons between the existing DFE-based algorithm [HKK+16] and the proposed MMSE-IC algorithm in AWGN channel

Figure 3-13 shows the BER of the proposed MMSE-IC algorithm with various prototype filters in AWGN channel. We observe that the proposed MMSE-IC algorithm significantly improves the BERs of QAM-FBMC system with the existing prototype filters. Particularly for 64-QAM, IC procedure is necessary to

obtain a satisfactory BER, e.g., 10^{-4} , as presented in Figure 3-13(b). In addition, we see that the simplified algorithm performs very similarly with the full procedure of Algorithm 1.

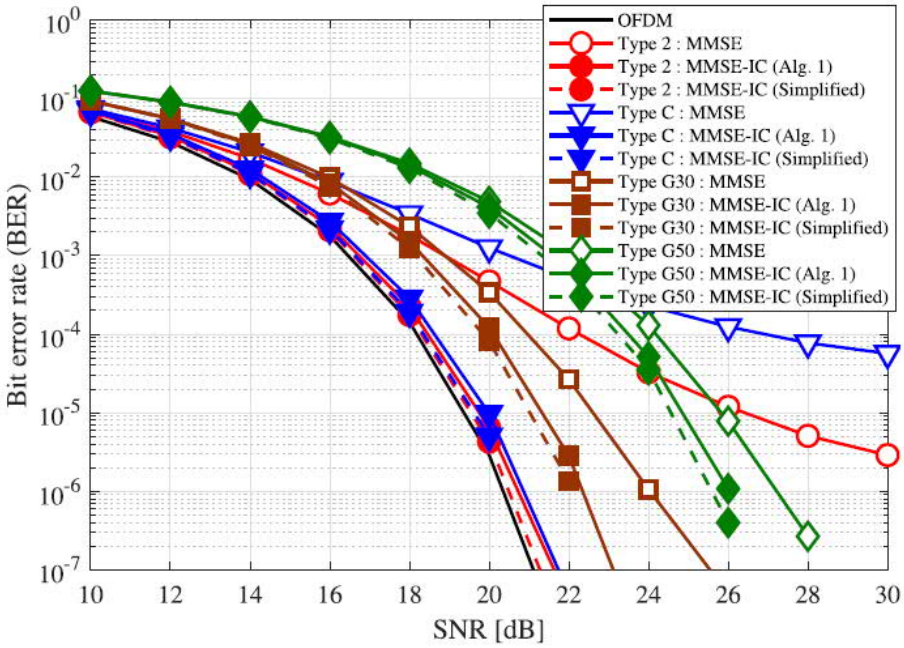

(a) 16-QAM in AWGN channel

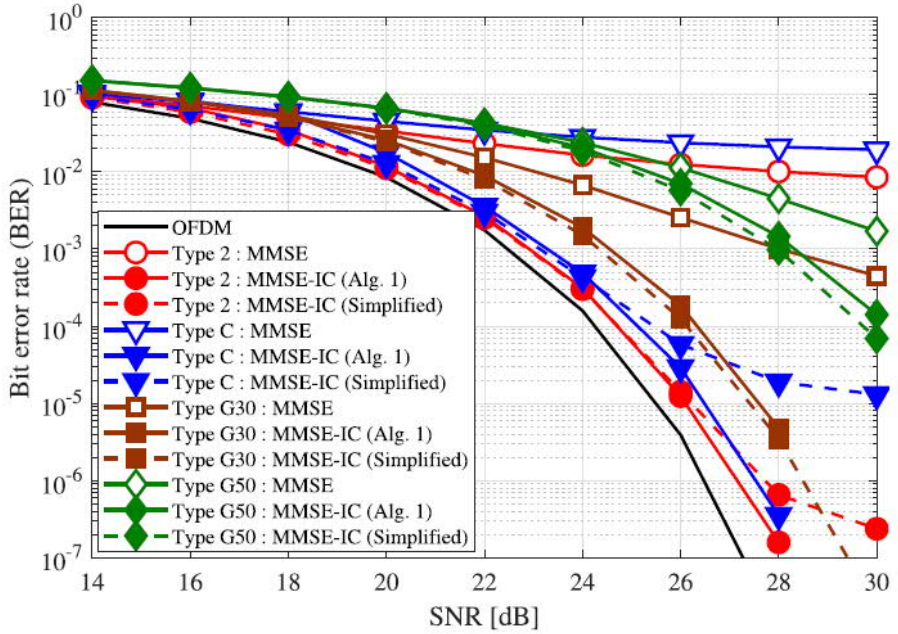

(b) 64-QAM in AWGN channel

Figure 3-13 The BER of the proposed MMSE-IC algorithm with the various prototype filters in AWGN channel: (a) 16-QAM and (b) 64-QAM

Figure 3-14 shows the BER of the proposed MMSE-IC algorithm in EPA and EVA channels, which are more realistic than AWGN channel. Even in the practical channels, it can be seen that the proposed MMSE-IC algorithm greatly improves the BER of QAM-FBMC with prototype filters and closely achieves the BER of OFDM system in moderate SNR region. Note that the DFE-based algorithm in [HKK+16] is

only applicable in AWGN channel.

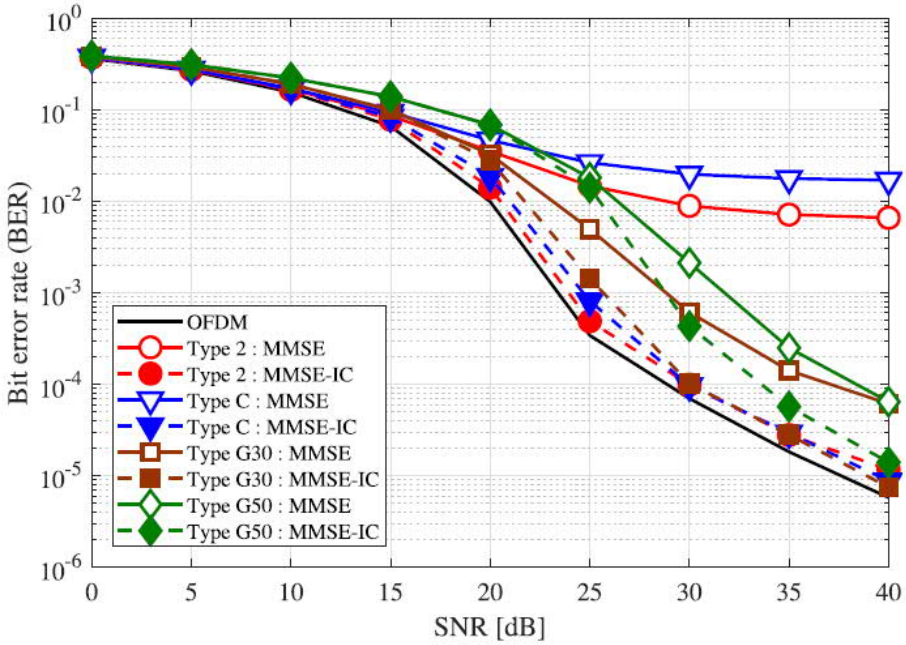

(a) 64-QAM in Extended Pedestrian A model (EPA)

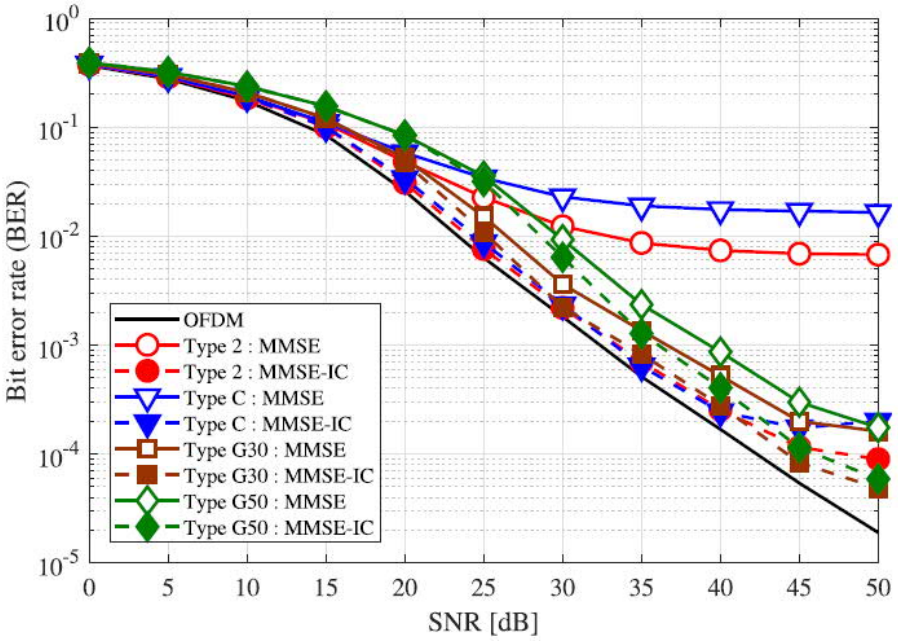

(b) 64-QAM in Extended Vehicular A model (EVA)

Figure 3-14 The BER of the proposed MMSE-IC algorithm with the various prototype filters in realistic wireless channels. The simplified algorithm is used for MMSE-IC scheme

Overall, when the MMSE-IC algorithm is used to perform IC, the effective noise variance during the cancellation proce-dures can be changed from the design target of the prototype filter. For this reason, the conventional prototype filters (such as Type 2 filter) with the proposed MMSE-IC algorithm show

good overall performance in moderate SNR region than the prototype filters designed by assuming the MMSE receiver.

3.4 Time-varying multiple access with spatial-frequency filter for mmWave

3.4.1 Universal Spatio-Frequency Division Multiple Access (USFDMA)

In PriMO-5G scenarios, drones need connectivity with the infrastructure and other drones for collaborative firefighting and immersive videos. Therefore, a large amount of sensing information needs to be exchanged in a very low latency. Similar to teleoperation applications, the required latency depends on the dynamics of neighboring environments such that the allowed air latency can be less than or equal to one millisecond with high reliability.

In order to get high reliability in a wireless fading channel environment, it is requiring a large amount of diversity with a coexistence of different waveforms and multiple access schemes within one carrier, according to various traffic characteristics. We propose new multiple access technology, universal spatio-frequency division multiple access (USFDMA), which can satisfy the requirements of URLLC for 5G service. The proposed waveform technique is available for time-varying multiple access with spatial-frequency filter.

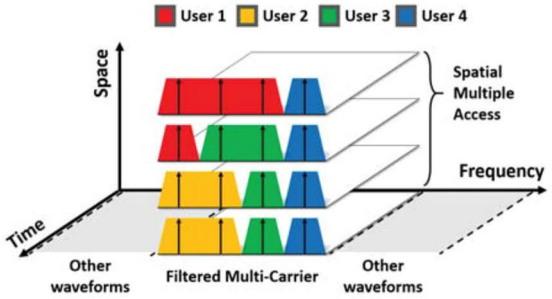

Figure 3-15 USFDMA PHY slicing

Consider the case of waveform multiplexing and a part of time-frequency resource within a carrier is allocated for URLLC services as shown in Figure 3-15. In this case, other waveforms are multiplexed in the outside of the allocated resource so that each waveform needs to provide low out-of-band emission (OOBE). USFDMA is a kind of filtered multicarrier waveform that allows a low OOBE so that it does not interfere other simultaneously multiplexed waveforms. In addition, it uses block-wise filters with block size according to the resource allocation for each user so that it provides orthogonality among different subcarriers allocated to different users. Furthermore, USFDMA allows multiple layers in th spatial domain so that arbitrary resource allocation in the spatio-frequency domain is possible. In order to maximize the spectral efficiency and connectivity while satisfying the challenging latency and reliability requirements in URLLC services, a user-specific spatio-frequency filter is employed by combining a precoding filter in the spatial domain and the pre-equalizer in the frequency domain with the knowledge of the channel state information (CSI), which can be obtained by using the channel reciprocity of the time division duplex (TDD) and the symmetricity in the traffic characteristics.

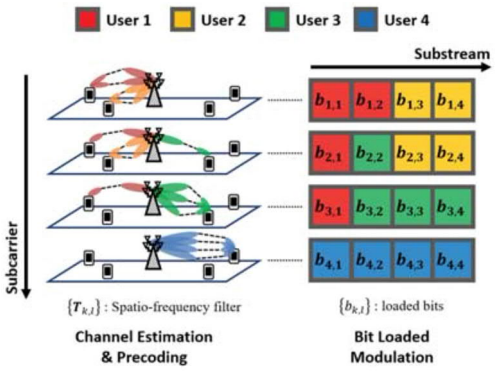

Figure 3-16 User-specific spatio-frequency filter and bit loaded modulation in USFDMA

The user-specific spatio-frequency filter structure is described in Figure 3-16. To further improve the spectral efficiency and connectivity while satisfiying the latency and reliability requirements, the spatio-frequency filter $\{\boldsymbol{T}_{k,l}\}$ and loaded bits $\{b_{k,l}\}$ on subcarrier k and substream l allocated to user i are jointly determined based on the knowledge of the CSI of each user as

$$\min_{\{\boldsymbol{T}_{k,l}\}\{b_{k,l}\}} tr(\boldsymbol{P})\ s.t \begin{cases} \sum_{(k,l)\in R_i} b_{k,l} = b_i \\ SINR_{k,l}(\{\boldsymbol{T}_{k,l}\}) \geq \beta(b_{k,l}), \end{cases} \quad (3.10$$

where b_i is the code block size for user i, $\boldsymbol{P}$ is the diagonal substream-wise transmission power matrix, and $SINR_{k,l}(\{\boldsymbol{T}_{k,l}\})$ denotes the instantaneous SINR which is function of CSIs and $\{\boldsymbol{T}_{k,l}\}$, and $\beta(b_{k,l})$ denotes the targe SINR which is determined from the reliability requirement and loaded bits $b_{k,l}$. A heuristic algorithm is proposed by decomposing the above problem by the two sub-problems of determining $\{b_{k,l}\}$ at a given $\{\boldsymbol{T}_{k,l}\}$ and vice versa, and iteratively solving each sub-problem. Then, within the scheduling period determined by the packet arrival rate and latency requirements, the rate of each user or the number of served users can be increased until $tr(\boldsymbol{P})$ is equal to the power constraint. At the receiver, a spatio-frequency post processing is also applied and we can see the transceiver design of USFDMA in Figure 3-17.

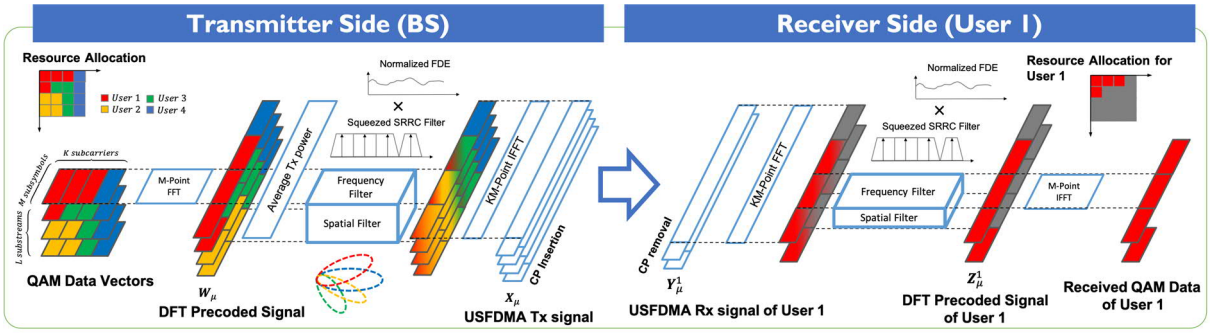

Figure 3-17 Transceiver Design of USFDMA

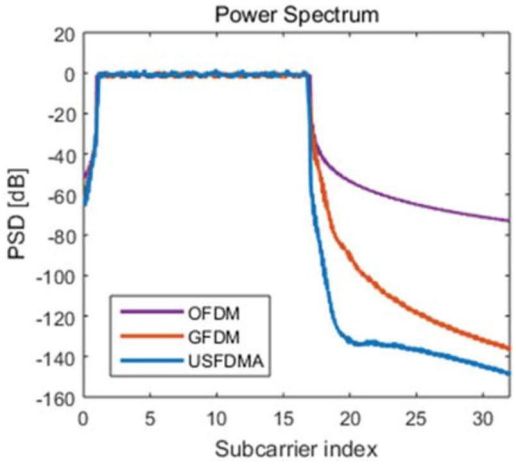

Figure 3-18 OOBE comparison of the waveforms

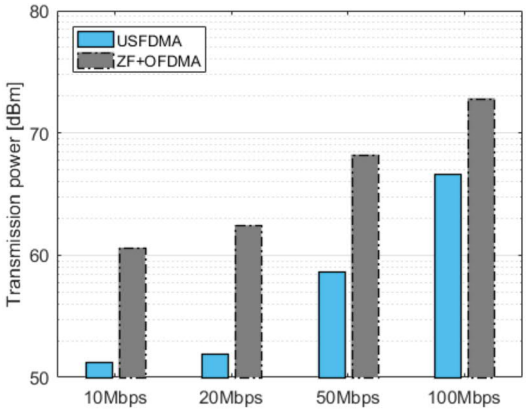

Figure 3-19 The transmission power corresponding to the data rate requirement of 4 users with the given 2048 subcarriers and 4 substreams

In Figure 3-18, the OOBE of the proposed USFDMA is plotted and compared in which the square root raised cosine (SRRC) filter with the roll-off factor of 0.1 is used and is squeezed to fit in the allocated subcarriers for each user. For comparison, orthogonal frequency division multiplexing (OFDM) and generalized frequency division multiplexing (GFDM) using the SRRC filter with the same roll-off factor are also plotted. Note that the use of user-specific spatio-frequency filter can further reduce the OOBE in the proposed USFDMA.

In Figure 3-19, the performance of the proposed USFDMA is compared with the orthogonal frequency division multiple access (OFDMA) with zero-forcing (ZF) precoder and uniform bit-loading. Here, we assume K = 2048 subcarriers in 20MHz as the system bandwidth and L = 4 substreams used in each allocated resource. The reliability requirement is set to 10^{-5}. A typical macro cell scenario with path loss and Rayleigh fading is assumed and the required transmission power is compared at given target rates for users when the path loss is -100dB and the noise spectral density is -174dBm.

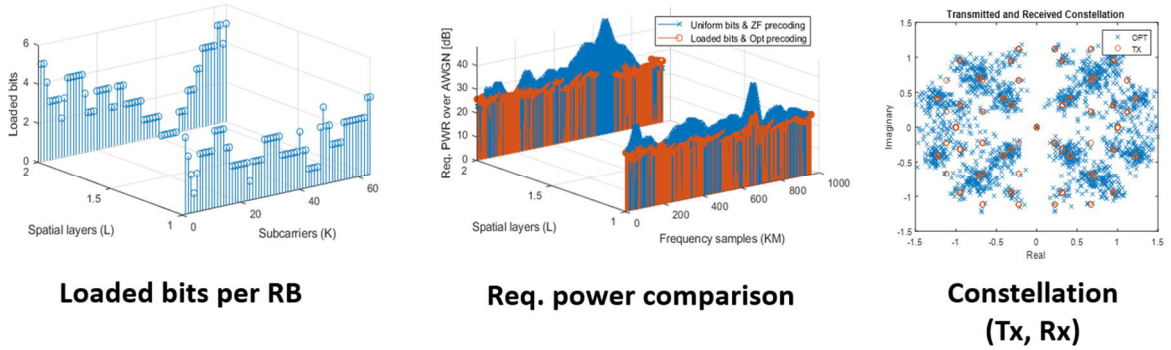

Figure 3-20 Joint optimization under the target SINR and the target data rate

We can also get joint optimization, power/resource optimization under the target SINR by User-specific spatio-frequency filter and power/resource optimization under the target data rate by bit-loaded modulation which is illustrated in Figure 3-20. From the results, it is shown that the proposed scheme can improve the spectral efficiency and/or connectivity while satisfying the requirements of URLLC services.

4 Beamforming technologies for PriMO-5G

4.1 Introduction

Multiuser hybrid precoding in 5G NR mmWave communication system faces significant challenges such as establishing accurate directional radio links and maintaining links for mobile stations (MSs) moving in outdoor environments, especially in the scenario of PriMO-5G, where the drones are moving with high speed. A conventional solution relies on finite codebook-based beam sweeping for initial first-stage beam acquisition and subsequent second-stage beam tracking by sweeping adjacent beam pairs. However, such a conventional solution has inevitable residual AoA/AoD errors even after the best beam pair is established in the first stage and incurs nonnegligible overheads to sound adjacent beam pairs for maintaining the best beam pair.

In this section, to overcome these problems, we propose two advanced beamforming technologies. First, a novel codebook-based two-stage solution that combines a novel beam tracking protocol with a low sounding overhead, a unique receiver structure employing a beam scheduler and a beam tester, and a fine accuracy residual AoA/AoD error estimation algorithm based on the monopulse ratio concept is proposed. Then, a novel AoA and beam tracking algorithm for the lens-incorporated mmWave hybrid architecture is presented.

4.2 Hybrid precoding with limited feedback for mmWave systems

Applications using unmanned aerial vehicles (UAVs), such as drones, are also emerging and among them are drones for public safety, remote explorations, logistics, flying base stations, etc. Owing to the high dynamics in such UAV environments, real-time video, audio, and haptic information should be exchanged within a low latency, i.e., the allowed air latency less than or equal to one millisecond for kinesthetic information and a few milliseconds to tens of milliseconds for high-quality video/audio information and haptic information.

There are significant challenges in multiuser hybrid precoding in 5G NR mmWave communication system such as establishing accurate directional radio links and maintaing links for mobile stations (MSs). A conventional solution relies on codebook-based beam sweeping for initial first-stage beam acquisition and subsequent second-stage beam tracking by sweeping adjacent beam pairs, which has inevitable AoA/AoD errors even after the best beam pair is established in the first stage and incurs nonnegligible overheads to sound adjacent beam pairs for maintaining the best beam pair in the second stage. The proposed solution combines a novel beam tracking protocol with a low sounding overhead, a unique receiver structure employing a beam scheduler and a beam tester, and a fine accuracy residual AoA/AoD error estimation algorithm based on the monopulse ratio concept.

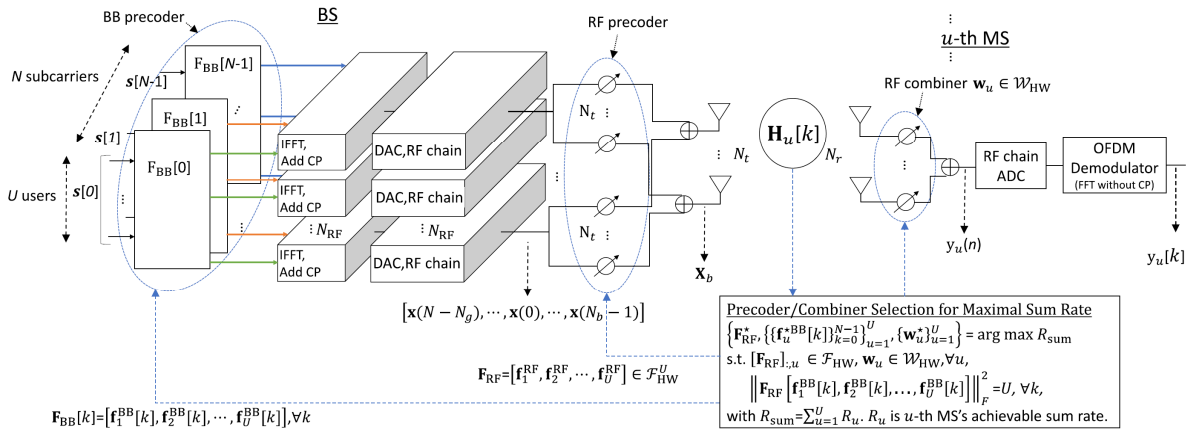

Figure 4-1 A single BS and multiuser mmWave system where the RF precoder has a fully connected

architecture as a representative case

A single BS multiuser mmWave system is shown in Figure 4-1. We assume that there are U selected MSs by an appropriate user selection algorithm, and each MS has N_r antennas and a single RF chain. To perform multiuser hybrid precoding, the BS has N_t antennas and N_{RF} RF chains. We describe the transmitter operation for downlink hybrid precoding in a multiuser MIMO OFDM system with N subcarriers. The transmit random data symbol vector $\mathbf{s}[k] = \left[s_1[k], s_2[k], \dots, s_U[k]\right]^{\mathrm{T}}$ for each subcarrier $k \in \{0, 1, \dots, N-1\}$. The BS applis a $U \times U$ BB digital precoder matrix $\mathbf{F}_{\mathrm{BB}}[k] = \left[\mathrm{f}_1^{\mathrm{BB}}[k], \mathrm{f}_2^{\mathrm{BB}}[k], \dots, \mathrm{f}_U^{\mathrm{BB}}[k]\right]$ to $\mathbf{s}[k]$ for all k. The N-point inverse fast Fourier transform (IFFT) is performed at each U RF chain to obtain the time domain signal $\mathbf{x}(n)$ for $n = 0, 1, \dots, N-1$ as

$$\mathbf{x}(n) = \frac{1}{\sqrt{N}} \sum_{k=0}^{N-1} \mathbf{F}_{BB}[k]\boldsymbol{s}[k] e^{\frac{j2\pi kn}{N}} \qquad (4.1)$$

The CP of length $N_g (\leq N)$ is added to the IFFT outputs to make one OFDM block of length $N_b = N_g + N$. Finally, an $N_t \times U$ frequency flat RF precoder $\mathbf{F}_{\mathrm{RF}} = [\mathrm{f}_1^{\mathrm{RF}}, \mathrm{f}_2^{\mathrm{RF}}, \dots, \mathrm{f}_U^{\mathrm{RF}}]$ is applised so that an OFDM block at the output of BS transmitter antennas becomes $\mathbf{X}_b = \mathbf{F}_{\mathrm{RF}}[\mathbf{x}_b(0), \dots, \mathrm{x}_b(N_b - 1)] = \mathbf{F}_{\mathrm{RF}}[\mathbf{x}(N - N_g, \dots, \mathbf{x}(N-1), \mathbf{x}(0), \dots, \mathbf{x}(N-1))$. Therefore, the effective transmit signal at subcarrier k is $\mathbf{F}_{RF} = \mathbf{F}_{\mathrm{RF}}\mathbf{F}_{\mathrm{BB}}[k]s[k]$, which is confirmed via IFFT/FFT relation.

4.2.1 Frame structure and concept of proposed solution

Figure 4-2 illustrates the concept of the proposed solution in comparison with the conventional solution. The frame comprises the first and second stages. The first stage can be divided into DL Beam Sweep and UL Beam Sweep. The second stage consists of multiple M_{CSI} repeats of a CSI period. The CSI period consists of CSI Acquisition and DL MU-MIMO Data Transmission. This frame structure is well suited for the two-stage multiuser hybrid precoding schemes.

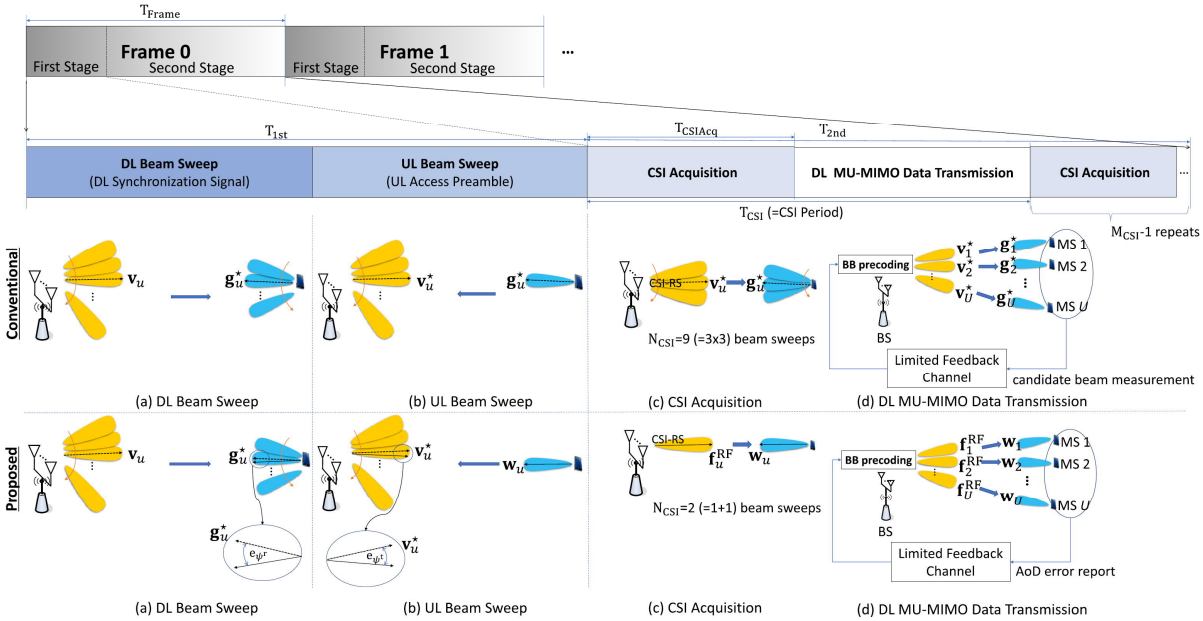

Figure 4-2 The frame structure and concept of the proposed solution in comparison to the conventional solution for a two-stage multiuser hybrid precoding

The conventional solution in Figure 4-2 can be viewed as a codebook-based method for beam acquisition and beam tracking procedures in 5G NR mmWave systems. As shown in Figure 4-2(a), the DL Beam Sweep in the first stage implies joint BS/MS beam sweeping using known reference signals (e.g., 5G NR synchronization signal (SS) blocks in an SS burst for initial directional cell search in the idle mode). Through beam pair tests (e.g., SNR mea- surement), each MS determines the best beam pair and best MS transmit beam for the following uplink beam sweeping. As shown in Figure 4-2(b), the UL Beam Sweep is for the BS to perform beam sweeping and to find out the best BS beam for each MS. As shown in Figure 4-2(c), the CSI Acquisition in the second stage has two functions. The first function is the measurement of candidate beam pairs adjacent to the current best beam pair for the MS under mobility. Based on the measurement, the BS and MS can switch to always-the-best beam pair. The N_{CSI} in the figure denotes the number of CSI reference signal (CSI-RS) symbols per CSI period. For the uniform linear array (ULA) type, N_{CSI} can be 9 (= 3 × 3) for the conventional solution. The second function is the BB CSI estimation using the CSI-RS symbols. Each MS estimates the BB CSI and reports the quantized BB CSI estimates to the BS. As shown in Figure 4-2(d), during the DL MU-MIMO Data Transmission, the BS transmits simultaneous data streams using multiuser BB precoding. The conven- tional solution uses the RF precoder/combiner only in the RF beam search codebook and does not estimate or compensate the residual AoA/AoD errors.

4.2.2 Monopulse ratio

We first explain the monopulse ratio, and then, the unique receiver structure to make the discriminating features feasible using the CP. Finally, we present the monopulse ratio based AoA/AoD error estimators built in the receiver structure. Some subscripts (subscripts μ, 1) in the following equations are omitted for brevity.

We briefly explain the monopulse ratio for the ULA type. For a target AoA $\hat{\psi}^r$, the sum beam, which always belongs to the DFT-based HW codebook, is denoted as $w_{sum} = a_r(\hat{\psi}^r) \in W_{\mathrm{HW}}$, and the difference beam, which is used only for estimating the AoA error, is denoted as $\mathbf{w}_{\mathrm{diff}}$ = DiffBeam($\mathbf{w}_{\mathrm{sum}}$) with

$$\mathrm{DiffBeam}(\mathbf{b}) = \left[-b_0, \ldots, -b_{\frac{M}{2}-1}, b_{\frac{M}{2}}, \ldots, b_{M-1}\right]^{\mathrm{T}} \tag{4.2}$$

for any array steering vector $\mathbf{b} = \left[b_0, \ldots, b_{\frac{M}{2}-1}, b_{\frac{M}{2}}, \ldots, b_{M-1}\right]^{\mathrm{T}}$ with a length M of an even number. For case $\hat{\psi}^r = 0$ and $N_r = 16$, the beam patterns of the difference beam and the sum beam ilustrted in Figure 4-3 are defined as

$$g_d = \mathbf{w}_{\mathrm{diff}}^* a_r(\hat{\psi}^r),\ g_s = \mathbf{w}_{\mathrm{sum}}^* a_r(\hat{\psi}^r). \tag{4.3}$$

The monopulse ratio plotted in Figure 4-4 together with the absolute values of g_d and g_s is debined by

$$r = \frac{\Im\mathcal{M}[g_d g_s^*]}{|g_s|^2} = \tan\left(\frac{N_r}{4} e_{\hat{\psi}^r}\right) \tag{4.4}$$

where the AoA error is $e_{\psi^r} = \psi^r - \hat{\psi}^r$ for a true AoA ψ^r.

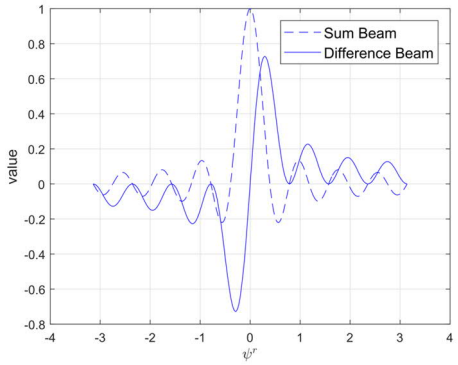

Figure 4-3 Beam pattern of the sum and difference beams

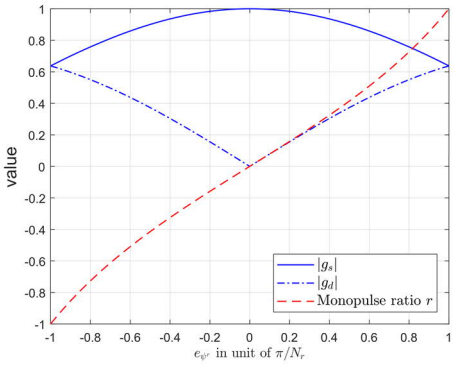

Figure 4-4 Monopulse ratio r of the sum and difference beams

- ***Protocol, receiver structure, and monopulse ratio based AoA Error estimator***

The conventional solution is limited in the array gain maximization and incurs non-negligible sounding overheads in protocols for measuring adjacent candidate beam pairs under mobility. Increasing the codebook size (e.g., using oversampled DFT-based RF beam search codebooks) is not a good remedy, as it worsens beam-sweeping overheads in the protocols. To remove the limitations, we devise a receiver structure that can perform finer resolution AoA/AoD error estimation even though the nonoversampled DFT-based RF beam search codebook is used for beam sweeping.

We notice a monopulse ratio that is a well-established AoA error estimator in radar systems to track moving tar- gets. However, simply adopting the monopulse ratio causes another obstacle that requires two separate RF chains for the respective sum and difference beam (nulling at the boresight) measurements. To avoid the 65bstacle, one can measure the sum and difference beam outputs in a time division multiplexing manner with a single RF chain. However, if an entire OFDM block is allocated to obtain the difference beam output, then the entire OFDM block would be wasted in terms of data rate.

Currently, we are motivated by classic methods in which the CP in OFDM systems is exploited for time/frequency synchronization purposes. In this report, the CP is exploited for angle synchronization. Therefore, we design an algorithm for the unique receiver structure equipped with a monopulse ratio-based AoA/AoD error estimator; this is integrated within one OFDM block. Thus, our solution can be used to detect and track well, even with a single RF chain condition, the direction of change of the current best beam pair. Therefore, our solution does not need to measure adjacent candidate beam pairs, thereby considerably reducing the sounding overhead of beam tracking in protocols.

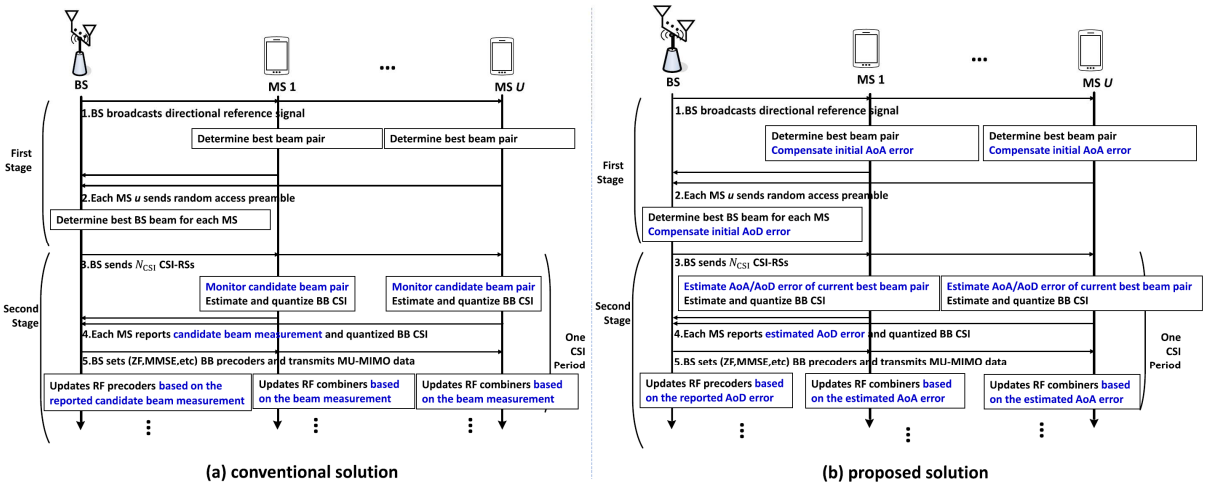

Figure 4-5 Protocol of the proposed solution in comparison with the conventional solution

In Figure 4-5, the protocol of the proposed solution is designed to have more accurate beam acquisition and lower sounding overhead beam tracking than the conventional solution. In the first stage, the proposed solution estimates and compensates the initial AoA/AoD error of the best beam pair found by DL/UL beam sweeping. This feature cannot be provided by the conventional solution. In the second stage, the sounding overhead N_{CSI} for beam tracking has a significantly reduced value than that in the conventional solution because the proposed solution does not need to monitor adjacent candidate beam pairs.

As shown in the left half of Figure 4-5, in the first stage of the conventional solution, the BS broadcasts directional reference signals and each MS finds the best beam pair by using codebook-based beam sweeping. Each MS sets the RF combiner corresponding to the identied best MS beam, and sends random access preambles. Then, the BS finds the best BS beam using codebook-based beam sweeping, sets the RF precoder as the determined best BS beam. Therefore, the BS and MSs establish directional radio links. In the second stage, at each CSI period, the MSs measure adjacent candidate beam pairs using N_{CSI} CSI-RS symbols for beam tracking and BB CSI estimation. Based on the measurement results, each MS reports the quality of the candidate beam pairs and quantized BB CSI estimates. The BS sends the MU-MIMO data streams to MSs using the calculated BB precoders. At the end of the CSI period, the BS and MSs update the RF pre- coders/combiners based on the measurement results of the candidate beam pairs for the next CSI period.

As shown in the right half of Figure 4-5, in the first stage of the proposed solution, the BS broadcasts directional reference signals and each MS finds the best beam pair by codebook- based beam sweeping. As a discriminating feature, each MS estimates/compensates the initial AoA error of the found best beam pair, sets the RF combiner corresponding to the estimated AoA, and sends random access preambles. Then, the BS finds the best BS beam by codebook-based beam sweeping. The BS estimates/compensates the initial AoD error of the found best BS beam, and sets the RF precoder considering the estimated AoD. Therefore, at the end of the first stage, the BS and MSs set up more accurate directional radio links than the conventional solution. In the second stage, at each CSI period, for both AoD/AoA error estimation of the current best beam pair and BB CSI estimation, the MSs requires much smaller numbers of the CSI-RS symbols for sounding (smaller N_{CSI}) than those for the conventional solution. Based on the measurement results, each MS reports the AoD error and quantized BB CSI estimates. The BS sends MU-MIMO data streams to MSs using calculated BB precoders. At the end of a CSI period, the BS and MSs update RF precoders/combiners based on the estimated AoD/AoA error for the next CSI period.

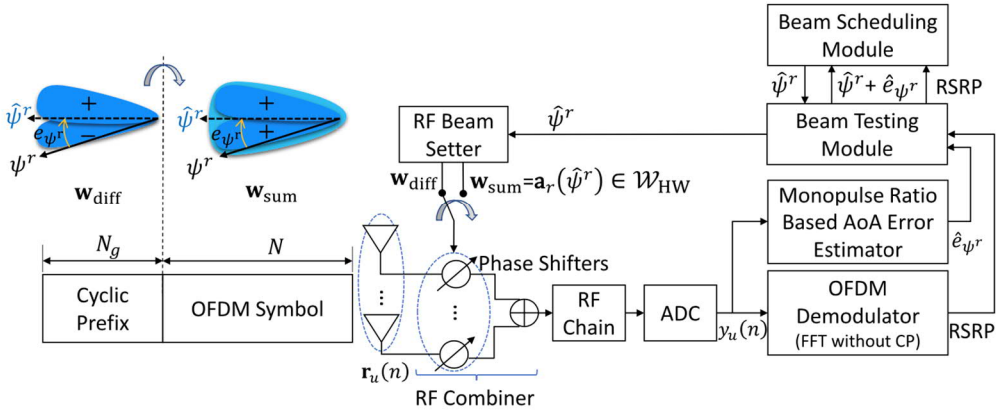

Figure 4-6 Receiver structure of the proposed solution to estimate the AoA error of the target MS beam. This also can be configured for AoD error estimation.

In Figure 4-6, the MS receiver structure is designed to make the protocol of the proposed solution feasible assuming the ULA type. The beam scheduling module schedules the target MS beam to test in an OFDM block, and then, the beam testing module configures the target AoA $\hat{\psi}^r$ to the RF beam setter and gathers an AoA error report $\hat{e}_{\psi^r}$ from the monopulse ratio based AoA error estimator, and the reference signal received power (RSRP) from the OFDM demodulator. The RF beam setter configures the difference beam $\mathbf{w}_{\text{diff}}$ to the phase shifters in the CP duration, and subsequently, it switches to the sum beam $\mathbf{w}_{\text{sum}}$ in the OFDM symbol duration. Using the difference beam and sum beam outputs, the monopulse ratio based AoA error estimator computes the estimate $\hat{e}_{\psi^r}$. The OFDM demodulator demodulates the OFDM symbol and reports the RSRP to the beam testing module. The RSRP can be used for best beam pair selection. When the OFDM block is not used for AoA error estimation, the RF beam setter holds the sum beam in the entire OFDM block.

In Figure 4-6, the received signal at the antennas of the u-th MS is modeled with a sample index n for $n = 0, \dots, N-1$ as $\mathbf{r}(n) = \sum_{d=0}^{D-1} \mathbf{H}_{u,d}\, \mathbf{v}_u x_b(n-d) + \boldsymbol{n}_u(n)$, where it is assumed that BS uses only one RF chain and its RF precode $\mathbf{v}_u \in \mathcal{F}$ for broadcasting the reference signals $x_b(n)$ with the full bandwidth. After analog combining, the input signal $y_u(n)$ of the AoA error estimator in Figure 4-7 is respectively denoted as $y_u^{\text{diff}}(n) = \mathbf{w}_{\text{diff}}^* r_u(n)$ during the CP interval and $y_u^{\text{sum}}(n) = \mathbf{w}_{\text{sum}}^* r_u(n)$ during the last N_g samples in the current OFDM symbol; it can be represented as

$$y_u^{\text{diff}}(n) = \sum_{d=0}^{D-1} \mathbf{w}_{\text{diff}}^* \mathbf{H}_{u,d}\, \mathbf{v}_u x_b(n-d) + \mathbf{w}_{\text{diff}}^* \boldsymbol{n}_u(n) \tag{4.5}$$

$$y_u^{\text{sum}}(n) = \sum_{d=0}^{D-1} \mathbf{w}_{\text{sum}}^* \mathbf{H}_{u,d}\, \mathbf{v}_u x_b(n-d) + \mathbf{w}_{\text{diff}}^* \boldsymbol{n}_u(n) \tag{4.6}$$

where $\mathbf{n}_u^N(n) = \mathbf{n}_u(n+N)$ and $\{x_b(n)\}_{n=-1}^{-D+1}$ are the last $D-1$ samples of the previous OFDM symbol.

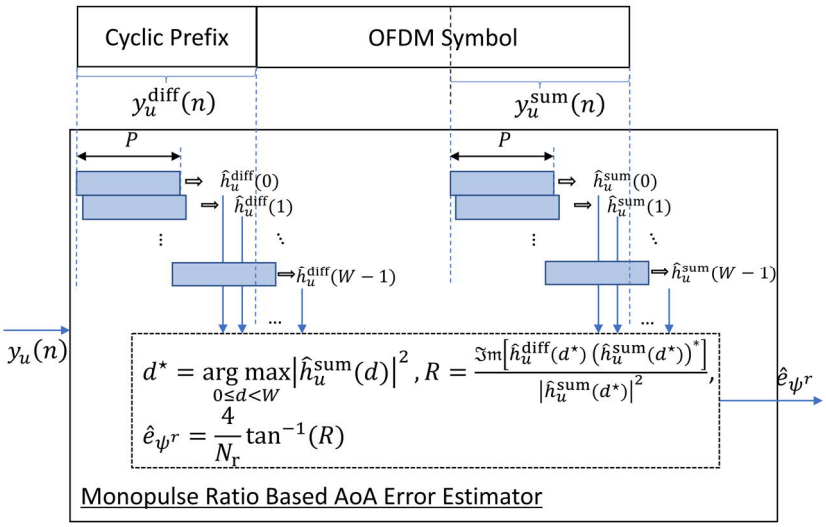

Figure 4-7 Monopulse ratio based AoA error estimator

First, by taking a cross-correlation with the pseudo-random reference signal sequences $\{x_b(n)\}$, the least square estimates on the d-th tap of the time domain BB channel can be obtained as

$$\hat{h}_u^{\mathrm{diff}}(d) = \frac{1}{P}\sum_{p=0}^{P-1} y_u^{\mathrm{diff}}(d+p)x_b^*(p) \tag{4.7}$$

$$\hat{h}_u^{\mathrm{sum}}(d) = \frac{1}{P}\sum_{p=0}^{P-1} y_u^{\mathrm{sum}}(d+p)x_b^*(N+p) \tag{4.8}$$

Here, the cross-correlation window length P can be appro- priately selected to suppress the IBI and the MPI from the previous and its own OFDM symbols as well as the AWGN. Then, the monopulse ratio estimate R is computed as

$$R = \frac{\Im\mathcal{M}\left[\hat{h}_u^{\mathrm{diff}}(d^\star)\left(\hat{h}_u^{\mathrm{sum}}(d^\star)\right)^*\right]}{\left|\hat{h}_u^{\mathrm{sum}}(d^\star)\right|^2} \tag{4.9}$$

where the dominant tap index $d^\star$ is found as

$$d^\star = \arg\max_{0\le d<W} \left|\hat{h}_u^{\mathrm{sum}}(d)\right|^2 \tag{4.10}$$

Finally, based on R or (R^x, R^y), we can estimate the AoA error of the target MS beam for ULA or uniform planar array (UPA) by

$$\hat{e}_{\psi^r} = \frac{4}{N_r}\tan^{-1}(R), or$$

$$\hat{e}_{\psi^{r,x}} = \frac{4}{N_{r,x}}\tan^{-1}(R^x),\ \hat{e}_{\psi^{r,y}} = \frac{4}{N_{r,y}}. \tag{4.11}$$

4.3 Fast AoA & beam tracking with lens antenna

4.3.1 Background and motivation

Previously, authors in [AKB13] devised a unique mmWave hybrid architecture based on the RF lens and the network of switches, which we denote as mmWave lens MIMO. The role of the lens is to focus the incident electromagnetic (EM) wave into certain directions, while the network of switches can actively steer the beam direction by activating certain antenna elements. Under the ideal lens design, the lens MIMO can form an identical analog beam with that of the phase shifter network by only activating a single antenna element, resulting in much lower power consumption and hardware complexity [AKB13]. It has been shown that mmWave lens MIMO can significantly reduce the required hardware cost than the conventional hybrid mmWave systems with negligible degradation in its performance.

Nevertheless, the acquisition of accurate channel information at the base station is imperative to achieve the system capacity. Such task is often challenging for the efficient supporting of UAV scenarios, such as that of PriMO-5G, due the the huge pilot overhead, which typically occurs from the large number of antenna elements, and the fast variation of the moving vehicle's channel. Thus, efficient channel tracking schemes which exploits the temporal correlation of the time-varying channel are of great interest [GAO16]. Thus, we focus on the fast angle of arrival (AoA) tracking problem which requires low latency and pilot overhead by exploiting lens MIMO and the temporal correlation of the channel.

4.3.2 System model

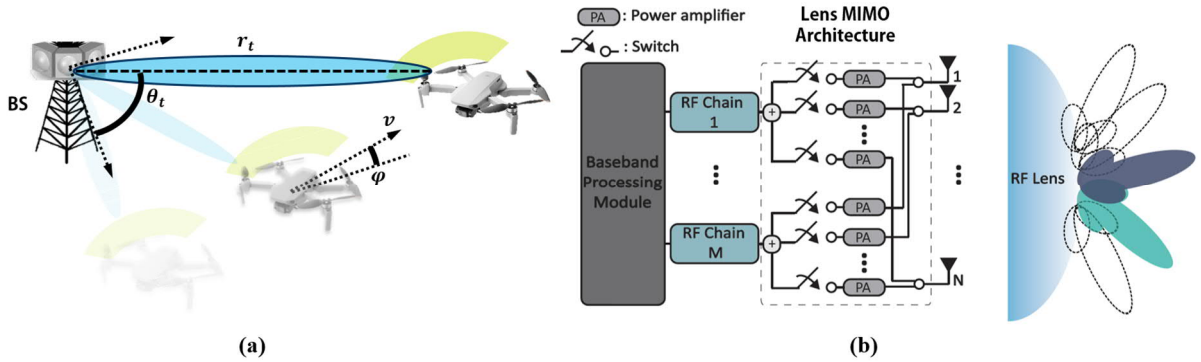

Figure 4-8. (a) UAV supporting BS with lens antenna; (b) RF lens-embedded hybrid aprecoding architecture

Figure 4-8 (a) represents the UAV supporting BS with lens antenna. Then, the AoA and the distance from the BS of the UAV at time instance t can be expressed by θ_t and r_t, respectively. The vehicle is assumed be moving on the road with constant velocity v and direction relative to the straight trajectory φ. Although v and φ are assumed to be constant values through out this study for simplicity, the proposed method can be easily expanded to scenarios with time-varying v and φ, whereas the assumption of liner UAV motion should hold. The architecture of mmWave lens MIMO system is illustrated in Figure 4-8 (b). There locates an RF lens in front of the antenna array, focusing the incident EM wave to certain directions. The antenna array is composed of N antenna elements, which may form a focal array as assumed in many previous studies, or a non-focal array. In this study, we consider a ULA serving K single antenna vehicles with N_{RF} = K RF chains, where the network of switches enables the analog beamforming.

4.3.3 Proposed fast AoA tracking method

Figure 4-9 illustrates the block diagram of the proposed AoA tracking method. Our method incorporates two main phases: antenna subset selection and low complexity AoA estimation with power profile of the

antenna array. We first scan the subset of information from the large antenna array, where the subset is determined at the previous time slot. Then, the AoA estimation algorithm is performed on the subset of information. Our proposed method enables AoA tracking with low pilot overhead and computational complexity.

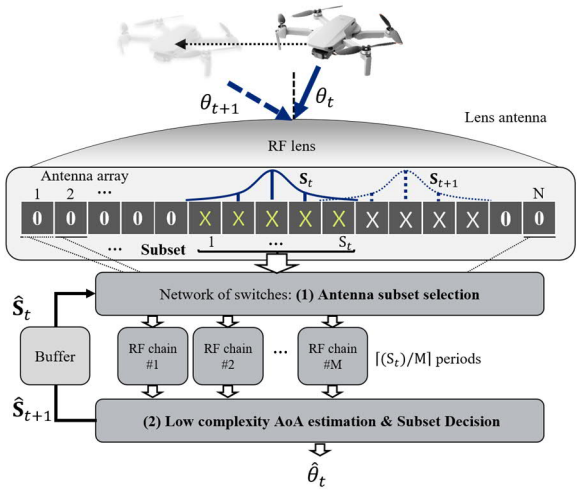

Figure 4-9. A block diagram of the proposed fast AoA tracking method

First, the antenna subset selection refers to accessing the information of only the subdivision of the entire antenna array. This motivates from the fact that the signal energy is mostly concentrated at the subregion of the entire antenna array in lens MIMO, where the subregion is determined by the AoA of the incident signal; and that the amount of information each antenna element conveys are not equal. Thus, instead of accessing the information from all the N antenna elements, we may reduce the overhead by exploiting the effective S_t elements.

The antenna subset at a certain time slot S_t is determined through the combination of the initial AoA estimate at the previous time slot and the motion model of the vehicle. For the motion model of the vehicle, we adopt the linear user motion model introduced in [GAO16]. Define the vehicle's motion state at time slot t as $\mathbf{m}_t \equiv [\theta_t\ \omega_t\ \varphi]^T$, where $\omega_t = \frac{v}{r_t}$ is the angular velocity at time t. By exploiting the laws of trigonometrical functions under the assumption that the vehicle is moving with constant velocity v and direction φ, the following relationship between adjacent time slots is derived,

$$\mathbf{m}_{t+1} = \boldsymbol{\Theta}(\mathbf{m}_t) = \begin{bmatrix} \arctan\left\{\frac{\sin(\theta_t)+T\omega_t\cos(\varphi)}{\cos(\theta_t)+T\omega_t\sin(\varphi)}\right\} \\ \frac{\omega_t}{\sqrt{1+2T\omega_t\sin(\theta_t+\varphi)+T^2\omega_t^2}} \\ \varphi \end{bmatrix}, \tag{4.12}$$

where, $\boldsymbol{\Theta}(\mathbf{m}_t)$ is a function of $\mathbf{m}_t$ and T is the time interval of a single time slot. Also, it can be derived that

$$\omega_{t+2} = \frac{\sin(\theta_{t+2}-\theta_t)}{2T\cos(\theta_t+\varphi)}, \tag{4.13}$$

$$\varphi = \frac{2\sin(\theta_{t+1}-\theta_t)\sin(\theta_{t+2}) - \sin(\theta_{t+2}-\theta_t)\cos(\theta_{t+1})}{2\sin(\theta_{t+1}-\theta_t)\cos(\theta_{t+2}) - \sin(\theta_{t+2}-\theta_t)\sin(\theta_{t+1})}$$

.

Based on the above equations, once we have estimated the motion states in time slots t, t + 1, and t + 2, the next motion state at time slot t + 3 can be derived assuming the linear motion of the UAV. Thus, once the system accumulates the estimates of AoA for the previous 3 time slots, we can utilize the initial estimation of the motion state at the next time slot to choose the subset indices for that slot.

After the first 3 time slots, we can obtain the initial estimate of the next time slot's motion state. Based on the initial estimate of the next motion state the array response of the lens antenna, we determine the subset for the next time slot by choosing the $|S_t| = s_t$ continuous indices of antenna elements with maximum amplitude in the array response.

Once the subset criteria is determined at the baseband, the network of switches will scan the values from the corresponding antenna elements with index $n \in S_t$. Then the truncated signal vector will be passed on to the AoA estimator for high precision AoA estimation. The proposed method only requires the information from s_t antenna elements at the baseband, thus reducing the required pilot overhead and latency. In practice, v and φ may be time-varying. However, because T is typically very short [GAO16], in the order of 1 ms, or less, the variation won't be large. Hence, by enlarging the subset size S_t, the error of initial estimation error can be refined at the second phase. The second phase of the proposed AoA tracking process is estimating the AoA with the selected subset. This is processed by a low computational complexity algorithm which we denote as power profile based estimation (PROBE), proposed in the earlier time frame of the project PriMO-5G. The principle concept of the AoA estimation algorithm is to exploit the power focusing property of an RF lens. Thanks to the sparsity in the received signal of the lens antenna system, the received array response has a unique power distribution according the input AoA. This can be exploited for AoA estimation with much lower computational complexity.

4.3.4 Simulation results

In this section, we present various simulation results to evaluate our proposed AoA tracking method. Throughout the section, we consider a mmWave lens MIMO system, where the lens antenna operates a linear array of N = 256 antenna elements with $d = \frac{\lambda}{2}$ and $N_{RF} = 4$ to serve K = 4 vehicles, and λ is the wavelength of a 28 GHz EM wave.

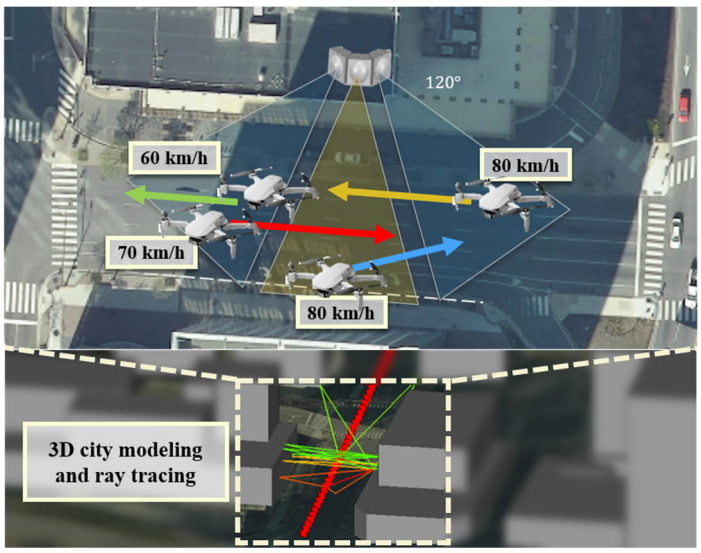

Figure 4-10. Concept view of AoA tracking simulation with realistic 3D urban modelling

For the tracking simulations, we consider a realistic V2I scenario in an urban city as described in Figure 4-10. We simulate our system in the 3D urban model of the downtown in Rossyln city, Virginia, the U.S. The BS is positioned at the edge of the 8 m building adjacent to the road. Total of 4 UAVs are moving in each of its velocity and direction, relative to the BS. We employ ray-tracing algorithm to model the realistic multi-path channels described earlier.

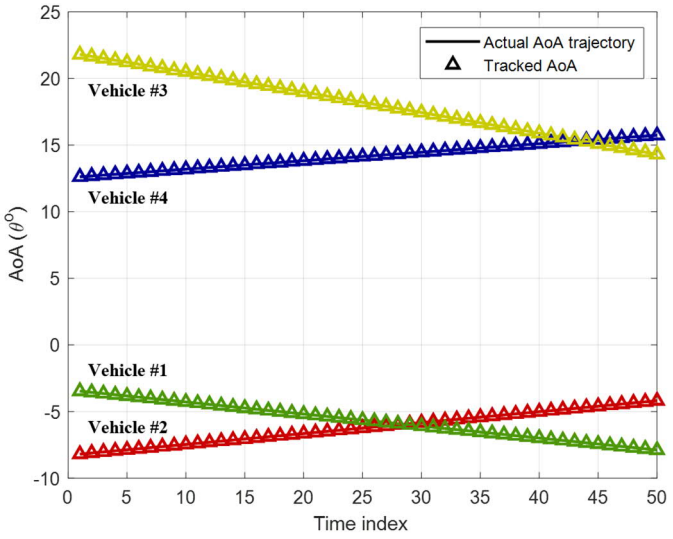

Figure 4-11. AoA tracking result of the UAVs in the urban city scenario

Figure 4-11 shows the AoA tracking accuracy of the proposed AoA tracking method, where the SNR is 10 dB. The simulation is done for 50 time slots with T = 1 ms. For the initial 3 time slots, Q = 128 pilots are used to estimate the initial motion states of the vehicles, and a reduced Q = 16 pilots are used for the remaining time slots. We observe that, for all the 4 vehicles, our proposed AoA tracking method tracks the actual AoA with very small deviation. This shows us that the proposed AoA tracking method shows good tracking performance with low pilot overhead.

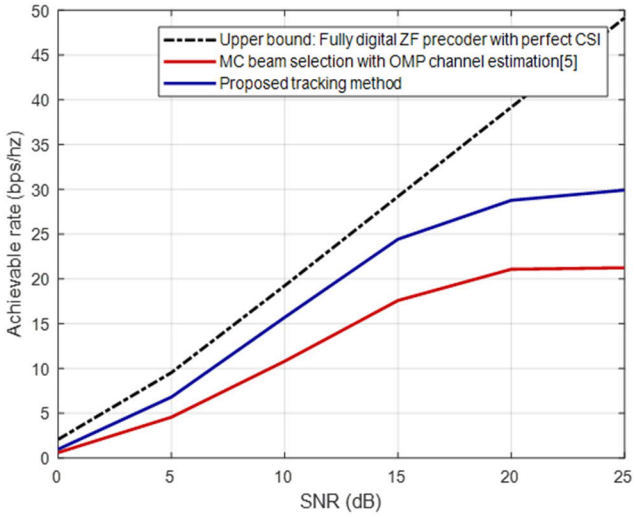

Figure 4-12. Sum-rate performance evaluation

Finally, we evaluate the impact of the proposed AoA tracking method on beam selection and the consequent sum-rate for downlink transmission. As mentioned earlier, our proposed method selects the subset for AoA tracking, and that subset can be used for the reduced-channel estimation. For comparison, we adopt the maximization of capcity (MC) beam selection proposed in [AMD15] and the channel estimation scheme with orthogonal matching pursuit (OMP) [RHJ14] as a benchmarks. For the benchmark, after estimating the channel with OMP, the operating antenna subset which maximizes the capacity information is selected. For fair comparison, we fix the number of pilots as $Q = 16$ and the SNR of the pilot as 10 dB for all the schemes. Once the operating subset is determined, zero-forcing (ZF) precoder is employed for the dimension-reduced precoding. Figure 4-12 shows the sum rate of 4 UAVs in the aforementioned urban scenario. We can observe that the proposed method outperforms the conventional MC beam selection with OMP channel estimation. This is because the proposed method can significantly reduce the pilot overhead for estimating the reduced-channel of the selected subset, while the benchmark system requires to estimate the entire channel first before the selection of the subset. Moreover, the performance gap between the proposed method and the fully digital ZF precoder with perfect channel state information (CSI) case is not large. Considering the fact that the proposed method only utilizes 4 RF chains while the fully digital case employs 256 RF chains, our proposed method shows enhanced cost-efficiency.

5 Conclusions

This deliverable is the final deliverable of WP3 of the PriMO-5G Project. The remainder of the study is provided except as previously submitted in D3.1 and D3.2. The objective of D3.3 is to provide the fundamental technologies to achieve PriMO-5G scenarios. Each section proposed appropriate technologies for those scenarios. Furthermore, this deliverable discusses the SWaP (size, weight, and power) issue.

5.1 Summary of technical contributions

Section 2 showed some of the limitations in conventional radio access technologies and different approaches considered for their enhancements to enable support of the PriMO-5G use cases. In Section 2.2, “Quality-aware trajectory planning of cellular-connected UAVs” is studied. The planning of flight trajectories for connected UAVs may result in suboptimal service at different stages of the flight if connection quality is not considered. This work proposed algorithms for trajectory planning of UAVs connected to terrestrial mmWave BSs, taking into consideration path length and quality of the ground-to-aerial connection. Besides, In section 2.3, we considered “Drone localization based on terrestrial transmitters.” Drone localization is a key feature not just for monitoring valuable drone assets but also ensuring high quality connectivity (e.g. for seamless handover). This work reported on measurement campaigns in both indoor-controlled and outdoor environments for enhanced localization of UAVs using multiple terrestrial BSs. In section 2.4, we showed that mmWave blockage effects on UAV networks could be sorted out by using beamforming gain and multiple antennas (MIMO) and increasing the bandwidth in our simulations. Another aspect that affects the KPIs analyzed (SINR, maximum Euclidean distance coverage, and Capacity coverage) is the interference mitigation. In addition, the performance of the connectivity highly depends on the height of the UAV. For what we call LoS sight (above 100m), the densification of the UAV is inversely proportional to the coverage capacity. On the other hand, for lower attitudes, we observe a maximum in terms of inter-site distance (ISD) for which the coverage is maximum. This is due to the effects of the interference in the ultra-dense scenarios. In section 2.5, we researched “Analysis of propagation characteristics UAV base stations with ray tracing.” The deployment of UAV base stations is a useful complement for terrestrial networks in places where coverage is limited or non-existence (e.g. damaged in fires). This work analyzed (with the help of ray tracing tool) the propagation characteristics of UAV base stations at different operating bands from sub-6 GHz bands up to 180 GHz, in a realistic 3D urban environment. In section 2.6, we improved the performance of sparse channel estimation, which is essential for the utilization of mmWave, by expressing each multipath element as a geometric sequence and applying the novel method of GSD-ST. In section 2.7, we proposed the mmWave Full Duplex-Interference Alignment(FD-IA) scheme to remove new interference came up with FD network. Our proposed scheme remove all interference of uplink users to downlink users and perform twice higher spectral efficiency compared to HD network. We analyze further with practical issues which could affect to our scheme and showed about 1.6 times higher spectral efficiency to HD network. In section 2.8, we proposed a grant-free multiple access (GFMA) that can reduce uplink connection time via grant-free uplink transmission so that GFMA can provide URLLC service with tight latency requirements such as immersive virtual reality (IVR).

In Section 3, a USRP-based mmWave prototyping architecture has been presented, which enables mmWave experimentation, prototyping, and antenna array characterization. An antenna-array-agnostic control was designed, which simplifies the integration with different kinds of antenna arrays. mmWave Beam Management has been developed based on NI’s Test UE / Test gNB. In section 3.3, we proposed the interference cancellation algorithm with MMSE receive filter for QAM-FBMC system, which is based on the concept of the MMSE-SIC and MMSE-PIC techniques. Furthermore, we composed the interference-canceling procedure as three cancellation stages which are the pre-cancellation stage, the SIC with MMSE filtering and the desired data symbol detection through the MMSE-PIC. Simulation results showed that the proposed MMSE-IC algorithm achieves similar BER enhancement to the existing DFE-based algorithm in AWGN, while the proposed MMSE-IC algorithm can also be used in a realistic fading channel with a simple structure and no system delay. In section 3.4, we proposed USFDMA as a new waveform robust to dynamics of neighboring environments establishing a

coexistence of different waveforms within one carrier. By multiplexing other waveforms in outside of the allocated resource, USFDMA can achieve low OOBE and spectral efficiency maximization.

In Section 4, we designed a beam tracking algorithm based on monopulse ratio exploiting the CP in OFDM system for angle synchronization, which can achieve more accurate beam acquisition and lower sounding overheads in protocols than the conventional solution even for a single RF chain MS suitable for establishing accurate directional radio links and maintaining links for fast-moving MSs. Also, we proposed a low latency AoA estimation method in mmWave lens antenna system.

5.2 Consideration of SWaP aspects

The drone operating and physical parameters, particularly Size, Weight, and Power (SWaP), can be a bottleneck for successfully operating PriMO-5G scenarios, smart firefighting using UAVs or drones. In practice, drone designs may either be rotary wing drones or fixed wing drones, with both having a role to play in different firefighting scenarios [P20]. The use of fixed-wing drones for firefighting provides benefits of longer flight time (several hours) and higher payloads carrying capability is outweighed by limitations of larger size, higher cost and inability to hover. By contrast, rotary-wing drones, such as, quadcopters drones are relatively cheaper and have ability to hover over firefighting scene capturing live immersive video or providing cellular coverage to ground devices while acting as aerial base station. However, these rotary wing drones have stringent limitations in terms of flying time (due to limited battery life) and relatively smaller size and lower payload weight support. These SWaP challenges in designing and operating rotary-wing drone base stations is generating a significant body of research particularly from a wireless communications technology perspective (e.g. see [FHM+19], and references quoted therein).

However, in WP3, radio access technologies and beamforming technologies in section 2, 4 is not affected by SWaP parameters because those technologies can be achieved in base-station and networks. In D3.3, the section that should be taken into account for SWaP is a novel radio mmWave Transceiver in Section 3.2. In Section 3.2, the mmWave Radio Transceiver design did not explicitly consider the SWaP aspects. However, the system resulting from these activities is supposed to be a prototyping platform for developing applications that indeed take care of these aspects. A means to support the power saving is beam management which is part of the mmWave Radio Transceiver design. While mainly being focused on compensating for the increased path loss at higher frequencies, it helps saving energy without sacrificing the key objectives high data rate and low latency. With this, small and lightweight drones are possible.

6 Reference

[3GPP19-38521-2] 3GPP TS 38.521-2 “User Equipment (UE) confirmance specification; Radio transmission and reception; Part 2: Range 2 standalone”, R15, V15.2.0, May 2019, Available online: https://www.etsi.org/deliver/etsi_ts/138500_138599/13852102/15.02.00_60/ts_13852102v150200p.pdf

[3GPP20-38101-2] 3GPP, TS 38.101-2, “User Equipment (UE) radio transmission and reception”, R15, Sep. 2020.

[3GPP20-38133] 3GPP TS 38.133, “Requirements for support of radio resource management”, R15, V15.10.0, June 2020.

[3GPP20-38211] 3GPP TS 38.211, “Physical channels and modulation”, R15, V15.8.0, January 2020. Available online: https://www.etsi.org/deliver/etsi_ts/138200_138299/138211/15.08.00_60/ts_138211v150800p.pdf

[3GPP20-38212] 3GPP TS 38.212, “Multiplexing and channel coding”, R15, V15.8.0, June 2020.

[3GPP20-38213] 3GPP TS 38.213, “Physical layer procedures for control”, R15, V15.10.0, June 2020,

[3GPP20-38214] 3GPP TS 38.214, “Physical layer procedures for data”, R15, V15.10.0, June 2020.

[3GPP20-38521] 3GPP, TS 38.521-2, “User Equipment (UE) conformance specification; Radio transmission and reception”, R15, Sep. 2020.

[AKB13] J. Brady, et al., “Beamspace MIMO for Millimeter-Wave Communications: System Architecture, Modeling, Analysis, and Measurementsj,” in *IEEE Trans. Antennas Propag*., vol. 61, pp. 3814—3827, 2013.

[AKL14] A. Al-Hourani, S. Kandeepan, and S. Lardner, “Optimal lap altitude for maximum coverage,” IEEE Wireless Communications Letters, vol. 3, no. 6, pp. 569–572, 2014.

[AMD15] P. V. Amadori, et al., “Low RF-Complexity Millimeter-Wave Beamspace MIMO Systems by Beam Selection,” in *IEEE Trans. Commun.*, vol. 63, pp. 2212–-2223, 2015.

[CEP+02] S. Coleri, M. Ergen, A. Puri and A. Bahai, "Channel estimation techniques based on pilot arrangement in OFDM systems," in *IEEE Transactions on Broadcasting*, vol. 48, no. 3, pp. 223-229, Sept. 2002, doi: 10.1109/TBC.2002.804034.

[DPS18] Erik Dahlman, Stefan Parkvall and Johan Skold, “5G NR: The Next Generation Wireless Access Technology“, 2018

[FHM+19] A. Fotouhi *et al.*, "Survey on UAV Cellular Communications: Practical Aspects, Standardization Advancements, Regulation, and Security Challenges," In *IEEE Communications Surveys & Tutorials*, vol. 21, no. 4, pp. 3417-3442, Fourth quarter 2019.

[GAO16] X. Gao, et al., “Fast Channel Tracking for Terahertz Beamspace Massive MIMO Systems,” in *IEEE Trans. Veh. Technol*., vol. 66, pp. 5689 – 5696, 2017.

[GNN+21] A. Gaber, A. Nahler, W. Nitzold, and M. Anderseck “USRP-based mmWave Prototyping Architecture with Real-Time RF Control”, IMS 2021, Atlanta, GA, June 2021.

[GZP+19] H. Groll *et al.*, "Sparsity in the Delay-Doppler Domain for Measured 60 GHz Vehicle-to-Infrastructure Communication Channels," *2019 IEEE International Conference on Communications Workshops (ICC Workshops)*, Shanghai, China, 2019, pp. 1-6, doi: 10.1109/ICCW.2019.8756930.

[K18] Younsun Kim, “NR Physical Layer Design: NR MIMO”, https://www.3gpp.org/ftp/workshop/2018-10-24_25_WS_on_3GPP_subm_tw_IMT2020/Docs/” RWS-18008, Oct. 2018.

[LLS21] W. -H. Lee, J. -H. Lee and K. W. Sung, "Geometric Sequence Decomposition With k-Simplexes Transform," in *IEEE Transactions on Communications*, vol. 69, no. 1, pp. 94-107, Jan. 2021, doi: 10.1109/TCOMM.2020.3028876.

[NI_RFmx_NR_Lib] https://www.ni.com/de-de/shop/software/products/rfmx-nr.html

[NI_RFmx_Waveform_creator]https://www.ni.com/de-de/support/downloads/software-products/download.rfmx-waveform-creator.html#371864

[P20] A. M. Petrillo, “Wildland Firefighting Aircraft: Fixed Wing, Rotors, Drones,” *Fire Apparatus & Emergency Equipment*, Jan. 2020. https://www.fireapparatusmagazine.com/fire-apparatus/wildland-firefighting-aircraft-fixed-wing-rotors-drones/#gref

[PRIMO-D11] PriMO-5G D1.1, "PRIMO-5G USE CASE SCENARIOS", Feb. 2019. Available online: Deliverables – Primo-5g (primo-5g.eu)

[PRIMO-D31] PriMO-5G D3.1, “INTERMEDIATE REPORT ON ENHANCED 5G RADIO ACCESS TECHNOLOGIES”, April 2019. Available online: Deliverables – Primo-5g (primo-5g.eu)

[PRIMO-D32] PriMO-5G D3.1, “INTERMEDIATE REPORT ON THE 5G TRANSCEIVER DESIGN AND ADAPTIVE BEAMFROMING”, April 2020. Available online: Deliverables – Primo-5g (primo-5g.eu)

[RHJ14] E. Ayach, et al., “Spatially Sparse Precoding in Millimeter Wave MIMO Systems,” in *IEEE Trans. Wireless Commun.,* vol. 13, pp. 1499—1513, 2014.

[SM15] S. K. Sahoo and A. Makur, "Signal Recovery from Random Measurements via Extended Orthogonal Matching Pursuit," in *IEEE Transactions on Signal Processing*, vol. 63, no. 10, pp. 2572-2581, May15, 2015, doi: 10.1109/TSP.2015.2413384.

[WTW+03] Xianbin Wang, T. T. Tjhung, Yiyan Wu and B. Caron, "SER performance evaluation and optimization of OFDM system with residual frequency and timing offsets from imperfect synchronization," in *IEEE Transactions on Broadcasting*, vol. 49, no. 2, pp. 170-177, June 2003, doi: 10.1109/TGRS.2003.810271